UNIVERSITY OF CALIFORNIA, SAN DIEGO

# Three-dimensional forces driving amoeboid cell migration and characterization of the extracellular matrix

A dissertation submitted in partial satisfaction of the
requirements for the degree
Doctor of Philosophy

in

Engineering Sciences (Mechanical Engineering)

by

Begoña Álvarez-González

Committee in charge:

Professor Juan C. Lasheras, Chair
Professor Juan C. del Álamo, Co-Chair
Professor Richard A. Firtel, Co-Chair
Professor Adam J. Engler
Professor Alison L. Marsden
Professor Shyni Varghese

2015

The dissertation of Begoña Álvarez-González is approved, and it is acceptable in quality and form for publication on microfilm and electronically:

_____

_____

_____

_____

Co-Chair

_____

Co-Chair

_____

Chair

University of California, San Diego

2015

DEDICATION

To Manu and to my parents, Javier and Carmen.

EPIGRAPH

*Imagination is more important than knowledge*

—Albert Einstein

TABLE OF CONTENTS

LIST OF FIGURES

LIST OF TABLES

LIST OF SYMBOLS AND ABBREVIATIONS

| | |
|---|---|
| 3DTFM | Three-dimensional Traction Force Microscopy |
| *abp120*$^-$ | Filamin null cells |
| AFM | Atomic force microscopy |
| APS | Ammonium persulfate |
| AR | Aspect ratio of the cells |
| cAMP | Cyclic adenosine monophosphate used as chemoattractant |
| *ctxA*$^-$ | Cortexillin I null cells |
| *ctxA*$^-$*/B*$^-$ | Cortexillin I and cortexillin II double null cells |
| *ctxB*$^-$ | Cortexillin II null cells |
| DIC | Differential interference contrast |
| DMSO | Dimethyl sulfoxide |
| E | Young's modulus |
| ECM | Extracellular matrix |
| FWHM | Full width half maximum |
| $\gamma$ | Cortical tension |
| GFP | Green fluorescent protein |
| $h$ | Substratum's thickness |
| $h_0$ | Distance from the bottom of the substratum at which the deformation is measured |
| $\eta$ | Vertical coordinate in the cell-based reference system |
| H2B | Histone 2B |
| LM | Lagrange multipliers |
| *mhcA*$^-$ | Myosin II null cells |
| MyoA | Myosin IA |
| *myoA*$^-$ | Myosin IA null cells |
| *myoA*$^-$*/B*$^-$ | Myosin IA and myosin IB double null cells |
| MyoB | Myosin IB |
| *myoB*$^-$ | Myosin IB null cells |
| MyoII | Myosin II |
| $\vec{n}$ | Unit vector normal to the surface of the substrate |
| PIV | Particle Image Velocimetry |
| PSF | Point spread function |
| $\sigma$ | Poisson ratio |
| SDS | Sodium dodecyl sulfate |
| $T$ | Period of cells' motility cycle |
| $\tau$ | Stress vector field $(\tau_{zx}, \tau_{zy}, \tau_{zz})$ |
| $\bar{T}$ | Three-dimensional stress tensor |
| $T_0$ | Main period of the strain energy autocorrelation function |
| TEMED | Tetramethylethylenediamine |
| TFM | Traction Force Microscopy |

| | |
|---|---|
| $\tau_n$ | Normal stresses |
| $\tau_t$ | Tangential stresses |
| $T_x$ | Axial tension |
| $T_z$ | Normal tension |
| $\mathbf{u}$ | Displacement vector field |
| $u$ | Displacement in the tangential direction to the substrate in the x-direction |
| $U_s$ | Strain energy |
| $U_{sn}$ | Strain energy generated by the normal forces |
| $U_{st}$ | Strain energy generated by the tangential forces |
| $v$ | Displacement in the tangential direction to the substrate in the y-direction |
| $w$ | Displacement in the normal direction to the substrate |
| $\xi$ | Horizontal coordinate in the cell-based reference system |

ACKNOWLEDGEMENTS

I would like to acknowledge Professor Juan C. Lasheras, who offered me this once-in-a-lifetime opportunity and allowed me to join his research group. I am deeply grateful to him for his constant professional guidance and also for his personal support. I also want to thank Professor Juan Carlos del Álamo, whose support was determinant to reach this opportunity. He has provided me a with a constant guidance and exceptional ideas, that have been essential during my PhD thesis. I am also grateful to Professor Richard A. Firtel, who gave me the opportunity to work in his laboratory in the Division of Cell and Developmental biology. He opened me the doors of a completely new field under his guidance. I want to acknowledge him for the useful discussions and supervision through all these years.

I also want to gratefully acknowledge Ruedi Meili, for teaching me most of the biological techniques that I have learnt. His ideas and help have been really indispensable and valuable for my PhD. thesis. I also want to thank Effie Bastounis, who has been close to me during all these years. The innumerable discussions with her have been very helpful for my work and her personal support has been really important. I am also grateful to Shun Zhang, who has teach me some experimental techniques and has been always willing to help me in the laboratory. I also want to acknowledge Baldomero Alonso-Latorre for his priceless guidance during my first year as a graduate student in UCSD. I am thankful, as well, to Susan Lee for her assistance in the laboratory and with some experiments. I also want to thank Alexis Lasheras for her help in editing my scientific papers and her personal support during all these years.

From the personal side, many people has my gratitude. During these years in San Diego I have develop friendships that I really want to maintain, I am very grateful to all of them for all the good moments. I also want to thank my friends from Spain, specially the ones from Soria, who have been always there and have made my day many times.

I also want to acknowledge my parents, Javier and Maria del Carmen. The have always been an unconditional support for me. They have done their best to give me an education, not only in the academic aspect. I truly appreciate what they have done for me in all the aspects of

my life, supporting me to achieve my goals.

Finally, I want to thank Manuel Gómez-Gonzlález, who has been my truly and constant support during all these years. I am grateful for his scientific support and his continuous encouragement. I certainly owe him a lot.

Chapter 2 has been in part published in *Applied Mechanics Reviews*, "Cytoskeletal mechanics regulating amoeboid cell locomotion" by B. Álvarez-González, E. Bastounis, R. Meili, R. A. Firtel, J. C. del Álamo and J. C. Lasheras (2014), 66 (5), 050804. It has also been published in part in *Biophysical Journal*, by B. Álvarez-González, R. Meili, E. Bastounis, R. A. Firtel, J. C. Lasheras and J. C. del Álamo (2015), 108 (4), 821-832. The thesis author is the primary investigator in these publications.

Chapter 3 has been in part published in *Biophysical Journal*, "Three-dimensional Balance of Cortical Tension and Axial Contractility Enables Fast Amoeboid Migration" by B. Álvarez-González, R. Meili, E. Bastounis, R. A. Firtel, J. C. Lasheras and J. C. del Álamo (2015), 108 (4), 821-832. The thesis author is the primary investigator in this publication.

Chapter 4 is currently being prepared for publication, "Cellular Traction Forces Quantification Improved by Lagrange Multipliers Optimization" by B. Álvarez-Gonzálezand, R. A. Firtel, J. C. Lasheras and J. C. del Álamo. The thesis author is the primary investigator in this publication.

Chapter 5 is currently being prepared for publication, "Novel Elastometric Microscopy to Characterize the Extracellular Matrix Properties" by B. Álvarez-González, R. A. Firtel, J. C. Lasheras and J. C. del Álamo. The thesis author is the primary investigator in this publication.

This investigation was partially funded by the U.S. National Institutes of Health.

I also acknowledge the support of the Ibercaja Foundation Fellowship, the Rita L. Atkinson Graduate Fellowship and the Siebel Scholars Foundation.

VITA

| | |
|---|---|
| 2008 | Ingeniero superior Aeronáutico.<br>Escuela Técnica Superior de Ingenieros Aeronáuticos.<br>Polytechnic University of Madrid, Spain. |
| 2008-2009 | Project Engineer.<br>Industria de Turbopropulsores S. A., Madrid, Spain. |
| 2009-2010 | Awarded Ibercaja Foundation Fellowship. |
| 2009-2015 | Research Assistant.<br>Departments of Mechanical and Aerospace Engineering and Division of Cell and Developmental Biology.<br>University of California San Diego, USA. |
| 2010-2011 | Teaching Assistant.<br>Departments of Mechanical and Aerospace Engineering and Bioengineering.<br>University of California San Diego, USA. |
| 2009-2010 | M. S. in Mechanical Engineering.<br>University of California, San Diego, USA. |
| 2011-2012 | Awarded Rita L. Atkinson Graduate Fellowship.<br>Departments of Mechanical and Aerospace Engineering and Division of Cell and Developmental Biology.<br>University of California San Diego, USA. |
| 2014 | Siebel Scholar, Class 2015. |
| 2015 | Ph. D. in Engineering Sciences (Mechanical Engineering).<br>University of California, San Diego, USA. |

PUBLICATIONS

J. C. del Álamo, R. Meili, **B. Álvarez-González**, B. Alonso-Latorre, E. Bastounis, R. A. Firtel, J. C. Lasheras. "Three-Dimensional Quantification of Cellular Traction Forces and Mechanosensing of Thin Substrata by Fourier Traction Force Microscopy.", *PLOS ONE*, 8 (9), p:1, 2013.

E. Bastounis, R. Meili, **B. Álvarez-González**, J. Francois, J. C. del Álamo, R. A. Firtel, J. C. Lasheras. "Both contractile axial and lateral traction force dynamics drive amoeboid cell motility", *Journal of Cell Biology;*, 204 (6), p:1045-1061, 2014.

**B. Álvarez-González**, E. Bastounis, R. Meili, J. C. del Álamo, R. A. Firtel, J. C. Lasheras. "Closure to "Discussion of Cytoskeletal Mechanics Regulating Amoeboid Cell Locomotion".", *Applied Mechanics Reviews*, 66 (5), p:056002, 2014.

**B. Álvarez-González**, E. Bastounis, R. Meili, J. C. del Álamo, R. A. Firtel, J. C. Lasheras. "Cytoskeletal Mechanics Regulating Amoeboid Cell Locomotion.", *Applied Mechanics Reviews*, 66 (5), p:050804, 2014.

**B. Álvarez-González**, R. Meili, E. Bastounis, R. A. Firtel, J. C. Lasheras, J. C. del Álamo., "Three-dimensional Balance of Cortical Tension and Axial Contractility Enables Fast Amoeboid Migration", *Biophysical journal*, 108 (4), p:821-832, 2015.

E. Bastounis, **B. Álvarez-González**, J. C. del Álamo, J. C. Lasheras, R. A. Firtel. "Cooperative Cell Motility during Tandem Locomotion of Amoeboid Cells." (Submitted).

**B. Álvarez-González**, R. A. Firtel, J. C. Lasheras and J. C. del Álamo. "Cellular Traction Forces Quantification Improved by Lagrange Multipliers Optimization." (In Preparation).

**B. Álvarez-González**, R. A. Firtel, J. C. Lasheras and J. C. del Álamo. "Novel Elastometric Microscopy to Characterize the Extracellular Matrix Properties." (In Preparation).

FIELDS OF STUDY

Major Field: **Engineering Science**

**Studies in Biomechanics**
Professors Juan C. del Álamo and Juan C. Lasheras.

**Studies in Tissue Engineering**
Professor Karen L. Christman.

**Studies in Fluid Mechanics**
Professors Daniel M. Tartakovsky and James W. Rottman.

**Studies in Computational Methods**
Professors Alison L. Marsden and Juan C. del Álamo.

**Studies in Applied Mathematics**
Professors Eric Lauga, Stefan G. Llewellyn Smith and William R. Young.

**Studies in Cardiovascular Fluid Mechanics**
Professor Alison L. Marsden.

ABSTRACT OF THE DISSERTATION

**Three-dimensional forces driving amoeboid cell migration and characterization of the extracellular matrix**

by

Begoña Álvarez-González

Doctor of Philosophy in Engineering Sciences (Mechanical Engineering)

University of California, San Diego, 2015

Professor Juan C. Lasheras, Chair

Professor Juan C. del Álamo, Co-Chair

Professor Richard A. Firtel, Co-Chair

Fast amoeboid migration requires cells to apply mechanical forces on their surroundings via transient adhesions. However, the role these forces play in controlling cell migration speed remains largely unknown. We use three-dimensional force microscopy to examine the mechanics underlying the chemotactic migration of wild-type *Dictyostelium cells*, as well as mutant strains with defects in contractility, internal F-actin cross-linking and cortical integrity. We show that cells pull on their substrate adhesions using two distinct, yet interconnected mechanisms: axial actomyosin contractility and cortical tension. The three-dimensional pulling forces generated by both mechanisms are internally balanced by an increase in cytoplasmic pressure that allows cells to push on their substrate downward without adhering to it. These compressive pressure-induced forces are not associated to adhesion sites, and may allow amoeboid cells to push off surrounding

structures when migrating in complex three-dimensional environments. We find a relationship between the strength of these three-dimensional forces and the migration speed and we show that the cell migration speed increases with the ratio of the tangential to normal forces. This finding indicates that the migration speed increases when axial contractility balances cortical tension, allowing the cells to modulate their three-dimensional shape and move faster.

Additionally, we develop a new methodology for the calculation of the three-dimensional forces exerted by migrating cells improved by a Lagrange multipliers optimization that provides a stress field in equilibrium and equal to zero outside the region in which the cell is localized.

Furthermore, we design a novel elastometry technique based on the exact solution of the elastic equation of equilibrium, the measurement of the deformation exerted by cells when moving and the application of an optimization algorithm for solving a non-linear least-squares problem. This novel method enables the characterization of the Poisson ratio of polymer-based substrates on real time, which is essential for a precise calculation of the traction forces. The value of the Poisson ratio that we obtain for the polyacrylamide gels used in our experiments is 0.45. A similar methodology could be applied to calculate the mechanical properties and constitutive equations for other extracellular environments, which are not perfectly elastic.

# Chapter 1

# Introduction

## 1.1 Background

Cell migration is important in many physiological processes such as embryonic development, wound healing, the response of the immune system or the regeneration and repair of tissues [1][2]. Furthermore, the failure or misregulation of the process of the cell migration results in pathological processes, such as the metastatic spreading of some cancer cells [3]. Some cardiovascular diseases are caused by the disordered movement of cells, for example atheriosclerosis is caused by interactions between circulating blood monocytes and T lymphocytes with the lining endothelium that trigger the migration and proliferation of smooth muscle cells in the artery [4][5]. Besides, some autoimmune diseases such as rheumatoid arthritis or multiple sclerosis are caused by dysregulation of the inflammatory response [6][7].

Cell migration encompasses the coordination of actin polymerization dynamics, motor protein-mediated contractility, and the formation and detachment of adhesion complexes necessary to transmit the internal forces to the extracellular environment [8][9]. Furthermore, it requires the combination of numerous biochemical and mechanical signals [10]. The cytoskeleton of the cells is fundamental in this process having mechanical and biochemical functions [11]. From a mechanical point of view, the cytoskeleton provides the structure for the cell and serves as support of its shape. Furthermore, the cytoskeleton generates the forces required for cell

migration through the polymerization of actin filaments and the contractility of motor proteins [12]. The cytoskeletal filaments are connected through distributed adhesions to the surrounding environment and transfer extracellular biochemical and mechanical stimuli to the intracellular signaling network [13][14][15].

Cells move either individually or collectively. In the case of single cell migration, there are two distinct types of locomotion: amoeboid and mesenchymal. Mesenchymal migration is characterized by high adhesion to the substrate. Usually the adhesions formed by mesenchymal migrating cells are integrin mediated and focal adhesions are clearly defined. This stronger adhesion leads to higher contractile traction forces [16]. The characteristic shape of the mesenchymal migrating cells is elongated [17]. In 3D matrices the movement of these cells is proteases-dependent and cells secrete metalo-proteases that degrade the extracellular matrix. Mesenchymal migration is a slow migration mode in which the traction forces are generated under the lamellipodium [18]. Examples of mesenchymal migrating cells are fibroblasts, smooth muscle cells, epithelial cells, endothelial cells and stem cells.

In contrast, amoeboid migration is characterized by low adhesion to the substrate and lack of mature focal adhesions. Consequently, the traction forces exerted by these cells are also low [16]. The adhesions in amoeboid migration are non-integrin or weak-integrin mediated [19][20]. The characteristic shape of the amoeboid migrating cells is rounded or ellipsoidal [21] [17]. These cells are highly motile and protease-independent in 3D matrices. Typically cells performing amoeboid migration have the ability to change cell shape (blebbing, elongation or bending). Amoeboid migration can be sub-classified in two types depending on the mechanism of forward extension of the plasma membrane: Blebbing (cells move by extending membrane blebs) and protrusion of actin-rich pseudopods (3D finger-like protrusions) [17]. Amoeboid cells are highly motile, and the contractile traction forces are exerted at the sides, front and back of the cell body [22] [23] [24]. The group of amoeboid migrating cells is very large and heterogeneous including unicellular eukaryotic cells such as *Dictyostelium discoideum* as well as individually migrating metazoan cells such as neutrophils and dendritic T cells.

Chemotactic migration is the directed movement of the cells in response to chemical

stimuli. An example of amoeboid migrating cells performing chemotaxing are neutrophils, which in response to chemicals produced by bacteria move to the infection sites as a key component of the immune response. The chemotactic process is controlled by a complex network of signaling events that trigger the remodeling of the cellular cytoskeleton and the formation and release of the adhesions to the extracellular matrix [25]. In the case of amoeboid cells, this process is tightly spatio-temporarily regulated and coordinated, resulting in a cyclic process [26][27][28]. The cycle is defined by protrusion of the leading edge through actin polymerization, formation of a new pseudopod and adhesion of this new pseudopod to the substrate, contraction of the cell body by interaction of F-actin and myosin, release of the rear adhesions and retraction of the cell body [24].

In this dissertation we study the chemotactic movement of amoeboid migrating cells. We perform chemotaxis experiments using *Dictyostelium discoideum* as a model experimental system to examine the mechanics of cell movement and to explore in detail the role of each cellular component involved in this process. *Dictyostelium* is an excellent model due to the high conservation of pathways and molecular components with some mammalian cells, such as mammalian neutrophils [29]. Other characteristic that make *Dictyostelium* a good model to explore the function of different components and signaling networks is the accessible manipulation of its genetics. *Dictyostelium* is haploid, its genes have only few and small introns which simplifies the genetic manipulation and facilitates the availability of a wide range of mutant strains with contractility, adhesion and actin polymerization defects. In addition, this makes easier the possibility of fluorescently label specific proteins inside the cell and therefore performing real time imaging of motility and of reporters of signaling pathways. Moreover, *Dictyostelium* is highly responsive to chemoattractants, consequently it facilitates the experimental study, and the key signaling pathways implicated in the directional cell movement are conserved from the amoeba to higher eukaryotes [29]. Furthermore, the spatio-temporal evolution and organization of the forces exerted by some mammalian cells migrating in an amoeboid manner and by *Dictyostelium* cells are very similar [30].

Unlike mesenchymally migrating cells, *Dictyostelium* cells do not form localized focal

adhesions. They attach to the substrate through diffuse areas and the molecular basis of the adhesions is not well characterized yet [31][32]. These cells move with a high velocity and therefore perform a fast assembly and disassembly of the adhesions, which entails a difficulty in understanding the molecular processes that control the formation and release of the adhesion sites.

## 1.2 Three-dimensional Traction Force Microscopy to study the mechanics involved in cell migration

In the last 20-25 years it has been recognized the importance of the study of cell migration form a mechanical approach. Several methods have been developed for the measurement and calculation of the forces generated by cells during migration [33][34]. These forces can be characterized using microscopy-based techniques that rely on the measurement of the deformation of thin membranes, the measurement of the deflection of micro-fabricated structures, or the measurement of the deformation of elastic hydrogels [35]. Scientist have realized the importance of coupling the biochemistry, signaling events and the mechanics involved in the locomotion process. Unraveling the interplay between the mechanics and biochemistry during migration will allow to construct better models to predict cellular motion and therefore to get a better control of the process.

During the past few years, there have been an increasing number of studies using Traction Force Microscopy (TFM) to study the mechanics of cells crawling on flat surfaces [36][20][37][38]. The majority of these TFM methods assumed that, while migrating, the cells only apply in-plane traction forces (tangential to the plane of the substrate) and do not exert out-of-plane forces (normal to the substrate's plane) [39][40]. The recent development of Three-dimensional Traction Force Microscopy (3DTFM) has produced mounting evidence showing that the normal component of the forces exerted by the cells can be as large as the in-plane (tangential) component [41][42][43].

The realization that cells generate out-of-plane stresses even when they adhere to plane

surfaces, indicates that the conclusions reached through the analysis performed using two-dimensional TFM methods may be not accurate. Consequently, it is necessary the study of the forces generated by cells through 3DTFM methods and the characterization of the error that the widely used two-dimensional TFM methods may have incurred by neglecting these stresses.

Additionally, there is a wide variability in the results obtained from a population of cells, and therefore it is crucial to be able to perform statistical analysis and consider a big number of cells to obtain definite answers to biological questions. In this dissertation, we use the 3DTFM method developed by del Álamo et al. [43] to study the structural origin of the three-dimensional forces exerted by amoeboid migrating cells and their function in migration. This method allows us to perform averages over many cells and over many instants of time through the normalization of the cell length, which guarantee statistically relevant conclusions and avoid biased results due to the specific cells selected for the measurements.

## 1.3 Aims of this dissertation

The actin polymerization at the leading edge of the cells generates the protrusion of new pseudopods, with the addition of actin monomers at the barbed end of the filaments and the loss of these subunits at the pointed end. The ability of the cells to generate forces requires that the cytoskeletal actin filaments are cross-linked and forming a continuos network. The actin cross-linking contributes to the stabilization of the cytoskeleton by linking the actin meshwork and therefore plays a structural role. Myosin II (MyoII) is a motor protein that is a very important F-actin cross-linker. *Dictyostelium* contains a single myosin II complex that is composed of two myosin heavy chains, two essential light chains and two regulatory light chains [44]. Each heavy chain contains a motor domain that allows the protein to slide over the actin filaments [45]. The C-terminal tail region forms a coiled coil with the second heavy chain molecule. MyoII accumulates mostly in the posterior edge of the cell and it is important for the retraction of the cells' rear part [46][47].

Another important actin cross-linker is the protein filamin. Filamin cross-links the actin

network in an orthogonal manner, and is needed to stabilize newly formed pseudopods in the anterior part of the cells [48]. Filamin is located mostly at the leading edge of the cells and is involved in the protrusion stage [49].

The cellular cortex is a major contributor to cellular rigidity [50]. It is composed of a thin shell of cross-linked actin filaments and myosin motors attached to the membrane and to the remainder of the cytoskeleton by binding proteins [51]. The cortex is critical to many biological processes, including cell division and motility [52][53]. The cell cortex coordinates cell shape changes and locomotion [54], i.e., the cortical tension regulates the internal pressure balance that promotes bleb formation [55][56]. Additionally, the cortical tension has been shown to be essential to breaking the symmetry necessary for cell polarization by regulating the forces transmitted to the extracellular environment [57][58][59].

The leading edge and posterior cross-linking of the cytoskeleton, the cortex, the nucleus, and its connectivity to the cytoskeleton are the major structural components involved in the generation of cellular traction forces [60][61][62]. However, the role that each of these cellular components plays in the generation of the traction forces, as well as in the mechanosensing of the external environment, is not well understood.

Cells with F-actin cross-linking defects generate lower traction forces that are distributed more laterally, and move slower than wild-type cells [24][63][64]. Nonetheless, these cells still generate significant traction forces and are able to migrate using mechanisms that are not fully understood yet.

Additionally, there is a need to better understand the properties of the cells' cortex and how it contributes to the generation of three-dimensional stresses in both stationary and motile cells. Among the many molecules that play a structural role in the cell cortex, we will focus on the role that cortexillin and myosin I play in the generation of cellular forces. Cortexillin I and cortexillin II are members of the α-actinin/spectrin family that are located in the cortex and are involved in the regulation of cell morphology and cell division [65][66]. On the other hand, myosin IA and myosin IB are single-headed motors involved in linking cortical and intracellular F-actin to the plasma membrane [67][68].

Furthermore, the nucleus is the largest and stiffest compartment of the cell and it is linked to the cytoskeleton, therefore it is also connected to the cells' adhesion sites [69]. Consequently, the nucleus might play a function in the generation of the stresses exerted through the adhesion sites [70]. Particularly, it has been hypothesized that it may be involved in the generation of the compressive normal forces [71].

The recent development of 3DTFM has showed that the normal component of the forces exerted by the cells can be as large as the tangential component [72][43]. This finding poses relevant questions, such as how does the cell generate forces in the direction perpendicular to the substrate, and how do the various structural components (anterior and posterior cytoskeletal cross-linking, cortical cytoskeleton and nucleus) contribute to the generation of these forces.

While it is well-known that migrating cells modulate the strength and spatial distribution of their traction forces to produce the necessary shape changes [73][74], until now, the association between the forces exerted by cells and migration was not established. The connection between forces and the efficiency of movement was still unclear and had never been stated. Therefore, the understanding of the traction forces' biological function remained widely uncovered. Hence, a critical question that remained unanswered was what roles do the normal and tangential components of the stresses play in establishing the efficiency of cell motility, including the migration speed of the cells. In this dissertation we present the relationship between forces and velocity of migration for amoeboid migrating cells, which provides the first connection between forces and migration speed to our knowledge.

This dissertation provides answers to many biological questions from a mechanical approach. We unravel the structural mechanisms for the generation of the forces and we establish the relationship between the tangential and normal forces and the velocity of migration. Additionally, it has been known during many years that the forces that a cell exert during migration are much larger than the needed to overcome the resistance of the surrounding environment [75]. In this dissertation we present a mechanistic explanation for the generation of such large forces, as well.

The understanding of the structural origin of the forces in *Dictyostelium* and their relationship with the efficiency of migration is key to elucidate the mechanisms of force generation

and their function in the amoeboid type of migrating mammalian cells, such as neutrophils. We have previously shown that the distribution and dynamics of the tangential traction forces exerted by differentiated HL60 cells, human promyelocytic leukemia cells that when differentiated behave similarly to neutrophils [76][77], are very similar to those exerted by *Dictyostelium* [30]. This suggests that there may be a common mode of amoeboid migration and possibly conserved mechanisms between all amoeboid migrating cells.

In addition, we have developed a novel approach in which Fourier Microscopy can be used to characterize the properties of the extracellular matrix in which cells move and to measure the forces that cells exert simultaneously on real time. We present a novel elastometry method based on the exact solution of the elastic equation of equilibrium, the measurement of the deformation exerted by cells when moving over an elastic substrate and the application of an optimization algorithm for solving a non-linear least-squares problem. This method is based on an extended procedure from the one used in Fourier Traction Force Microscopy, with a novel application as Elastometric Microscopy.

Elastic polymer-based hydrogels are broadly used for the calculation of the traction forces that cells apply when moving [36][78]. The accurate characterization of their elastic properties is crucial for a precise calculation of these traction forces. It was assumed that the value of the forces exerted by the cells didn't depend much on the value of the Poisson ratio of the substrate over which they move, but on the contrary the value of the forces is very sensitive to the value of the Poisson ratio, especially for values close to 0.5, which is the case of hydrogels [43]. We present a novel method for characterizing the Poisson ratio of polymer-based substrates on real time. A similar methodology could be applied to calculate the mechanical properties and constitutive equations for other extracellular environments, which are not perfectly elastic. This methodology has the potential to be used in the quantification of the interactions between different cells and the environment in which they move in real time.

## 1.4 Outline of the dissertation

In chapter 2, we present the experimental techniques that we have used to study the mechanics underlying the chemotactic amoeboid type of migration. In this chapter we also explain the analytical methods that we have used for the quantification of the forces and tensions exerted by amoeboid migrating cells. The method to calculate the forces is based on the solution of the elastic equation of equilibrium, and requires the measurement of the deformation applied by the cells when moving in the three spatial directions. In this chapter we present a thorough analysis of the accuracy that we achieve in the measurement of the deformation field and a study of the necessary configuration for the acquisition of the images with the microscope in order to achieve precise measurements of the forces. We also present a comparison between the tangential traction forces exerted in the plane of the substrate when using a 2D and a 3D Fourier force methodology.

In chapter 3, we unravel the structural origin of the three-dimensional forces exerted by amoeboid cells and the connection between the migration speed and the tangential and normal forces. Additionally, we characterize the location of actin foci, which are actin rich structures localized in the ventral side of *Dictyostelium* cells that have been previously reported to be located in the adhesion sites, and we find the relationship between adhesion sites, pulling and pushing forces. We study ten different *Dictyostelium* cell lines, with leading edge and posterior cross-linking defects, impaired cortical integrity and deficient of connection between the plasma membrane and the cortical and intracellular F-actin. We also study the function of the nucleus in the generation of the compressive forces through a cell line that has the nucleus fluorescently labeled by tagging the protein Histone2B to GFP.

In chapter 4, we present a new method for the calculation of the forces exerted by migrating cells that accounts for the limitations of Fourier Traction Force Microscopy. These limitations are that the forces obtained by TFM may not be balanced and we can find some forces applied outside the region where the cell is located. We perform a Lagrange multipliers optimization and imposed two constraints for the calculation of the forces. The first one is that

the forces exerted by the cell need to be in equilibrium, since the cell does not generate a net force. The second constraint is that the forces must be applied only in the region where the cell is located, therefore the forces outside the contour of the cell must be equal to zero. Imposing these two constraints, we obtain results that agree with the physics behind this subject, in contrast to the ones obtained with unconstrained TFM methods.

In chapter 5, we present a novel methodology for the calculation of the properties of the extracellular matrix. This technique is based on the solution of the elastic equation of equilibrium, similarly to the 3DTFM method that we use for the calculation of the cell-substrate forces. This new Elastometric Microscopy technique allows the measurement of the Poisson ratio of elastic hydrogels, extensively used in TFM. There is a wide range of values for the Poisson ratio of polymer-based elastic hydrogels in the literature, and the error made in the measurement of this value results in large errors in the computation of the forces. Additionally, our technique allows the simultaneous quantification of the cell-substrate forces applied in real time.

Finally, in chapter 6 we present a summary of the aims and contents of the dissertation. This chapter provides the general conclusions and final remarks of this study.

# Chapter 2

# Experimental and analytical methodology to study the mechanics of chemotactic amoeboid migration

## 2.1 Introduction

Several methods have been developed to characterize the dynamics of cells when migrating over flat substrates [79]. Most of these methods are based on measurements of the deformation of a flat elastic substrate on which the cells crawl, and the subsequent calculation of the traction forces from the measured deformation. Dembo et al. used the classical solution of the elastostatic equation for a homogeneous, semi-infinite medium found by Boussinesq for the elastic solid in the half-space [34] [80]. Butler et al. calculated the traction forces by performing the Fourier transform of the displacement field and applying the solution to the Boussinesq equation in Fourier space to obtain the forces through the inverse Fourier transform [33]. These methods do not take into account the effect of the finite thickness of the substrate and consider it semi-infinite. A third method was developed by Yang et al., which consists of using a 3D finite element method and the effect of a finite substrate is incorporated [81].

Until recently, traction force microscopy methods were focused on measuring the traction forces exerted by the cells only in the tangential direction to the plane where the cells were attached, while the perpendicular component was neglected. The role of the z-component was supposed to be negligible assuming that the predominant orientation of the contractile fibers of the cytoskeleton is mainly horizontal. But since cells and their environment are three-dimensional, it is important to measure the traction forces in the perpendicular direction to the substrate as well.

There are some methods that have been developed recently in order to measure the three-dimensional traction forces; they reveal that the perpendicular forces to the substrate are not negligible. Hur et al. [41] developed a method to measure this perpendicular component as well as the in-plane components by using a finite element method and applying the constitutive equations (elastic stress-strain law). Franck et al. [72] calculated the traction forces exerted by 3T3 fibroblasts from the deformation applied on the substrate directly from the constitutive equations for a linearly elastic and incompressible medium. To study the mechanics underlying chemotactic amoeboid migration we used the 3D Fourier Force Microscopy method developed by del Álamo et al. [43], which consists of an exact, computationally efficient solution of the elastic equation of equilibrium based on Fourier expansions that obtains the traction forces explicitly as functions of the substrate deformations. This method takes into account the substrate thickness, which increases the accuracy of the Boussinesq solution and allows for non-zero net forces. It also considers the distance between the measurement plane and the surface of the substrate.

We have used diverse experimental and analytical techniques to study the mechanics of cell migration. This chapter includes a summary of the techniques used for examining the functioning of the internal cytoskeleton, the cortical region and the nucleus of cells in the mechanics of chemotatic migration. Furthermore, we performed a thorough analysis for the accurate calculation of the displacement field applied by these cells to the substratum over which they move, which is crucial for the accurate calculation of the traction forces that they exert. Additionally, we present a comparison of the tangential forces and the strain energy calculated for a cell when using a two-dimensional and a three-dimensional methodology.

## 2.2 Cell culture and microscopy

*Dictyostelium discoideum* cells were grown under axenic conditions in HL5 growth medium on tissue culture plates. We used ten different cell lines, wild-type Ax3 and Ax2, myosin II null cells (*mhcA*$^-$), (generated from Ax3), filamin null cells (*abp120*$^-$), (generated from Ax2), cortexillin I null cells (*ctxA*$^-$), (generated from Ax2), cortexillin II null cells (*ctxB*$^-$), (generated from Ax2), cortexillin I and cortexillin II double null cells (*ctxA*$^-$*/B*$^-$), (generated from Ax2), myosin IA null cells (*myoA*$^-$), (generated from Ax2), myosin IB null cells (*myoB*$^-$), (generated from Ax3) and myosin IA and myosin IB double null cells (*myoA*$^-$*/B*$^-$), (generated from Ax3). All the cell lines were obtained from the Dicty Stock Center except the *myoA*$^-$, *myoB*$^-$ and *myoA*$^-$*/B*$^-$, which were generously provided by Dr. Margaret Titus, and in which myosin I genes were disrupted by recombination, following the procedures found in Peterson et al. [82] and Novak et al. [67].

*MhcA*$^-$ cells lack the protein myosin II, which localizes at the back of the cell and acts both as an F-actin crosslinker and as a motor [83]. *Abp120*$^-$ cells lack the protein filamin, which localizes at the front of the cells and is required for the stabilization of the newly formed pseudopods [48]. *CtxA*$^-$, *ctxB*$^-$ and *ctxA*$^-$*/B*$^-$ cells lack the protein cortexillin I, cortexillin II and both proteins, respectively. Cortexillin I and cortexillin II are F-actin-binding proteins, members of the $\alpha$-actinin/spectrin family that are located in the cortex of *Dictyostelium* cells [84]. *MyoA*$^-$, *myoB*$^-$ and *myoA*$^-$*/B*$^-$ cells lack the protein myosin IA, myosin IB and both proteins, respectively. Myosin IA and myosin IB are single-headed actin molecular motors involved in the connection between the plasma membrane and the cortical and intracellular F-actin [67].

For all chemotaxis applications, cells were taken from axenic exponentially growing or "log-phase" cultures, by shaking cells in nutrient medium, in an autoclaved Erlenmeyer flask at 150 rpm, 22$^o$C, overnight. The next morning cells were counted using a hematocytometer to determine the cell density. The aggregation competent cells were prepared by pulsing a $5 \cdot 10^6$ cells/ml suspension in Na/K phosphate starvation buffer (9.6mM $KH_2PO_4$, 2.4mM $Na_2HPO_4$, pH 6.3) with cAMP to a concentration of 30 nM every 6 minutes during 6 hours. Then, the cells

were diluted in Na/K phosphate buffer to a concentration of $2 \cdot 10^4$ cells/ml and 200 $\mu$l of cells with this concentration were seeded onto the functionalized flat elastic polyacrylamide substrate and allowed to adhere.

A drawn glass capillary mounted on a micro-manipulator served as the source of chemoattractant (150mM cAMP in an Eppendorf femtotip, Eppendorf, Germany). We acquired images using a spinning disk confocal microscope (Zeiss) and a cooled charge-coupled device camera (HQ CoolSNAP; Roper Scientific). The microscope was equipped with a piezo-Z actuator (ASI). A PC running Slidebook software (3I) controlled the entire setup.

## 2.3 Blebbistatin treatment of the cells

We dissolved (-)- blebbistatin ( Sigma-Aldrich) into Dimethyl sulfoxide (DMSO) to make a 100mM stock solution. Then, cells were treated with 50$\mu$M blebbistatin by diluting the stock solution in Na/K phosphate starvation buffer (9.6mM $KH_2PO_4$, 2.4mM $Na_2HPO_4$, pH 6.3).

When blebbistatin is present, the illumination with a light of wavelength lower than 490 nm causes the generation of free radicals that result in cell damage [85][86]. We observed that in experiments with blebbistatin, wild-type cells couldn't move and did not generate forces when the wavelength of the light was 488nm, even when the concentration of blebbistatin was very low. Whereas when illuminating the cells with a wavelength of 531nm, wild-type cells moved and generated forces. Therefore, in the experiments involving blebbistatin we always used 531nm light. In the rest of the experiments, we always used 531nm light as well, except for the calculation of the actin distribution in which we used 488nm light, and image GFP-labeled actin for the experiments without blebbistatin.

## 2.4 Polyacrylamide substrates fabrication

To fabricate the polyacrylamide gels, first we treated the glass coverslips, in order to allow the attachment of the gels. Initially we placed 22mm #1 square glass coverslips on a hot plate and added 500$\mu$l of 0.1M NaOH. We waited until the liquid was evaporated and a

uniform layer of NaOH was formed. After this, we covered the coverslips with 100$\mu$l of 3-Aminopropyltriethoxysilane during 5 minutes. Once we rinsed the coverslips with MQ water and dried them completely, we covered them with 100$\mu$l of 0.5% Glutaraldehyde during 30 minutes. Then we rinsed the coverlids with MQ water and dried them. After this step, the gel can be attached to the treated glass coverslip.

We fabricated the gels as two adjacent layers in order to improve the signal-to-noise ratio of the image z-stacks and the displacement field calculation. The bottom layer was made with 4% acrylamide and 0.056% bisacrylamide [87][88] , 0.2% tetramethylethylenediamine (TEMED) and 0.05% ammonium persulfate (APS). We put 3.4$\mu$l of this mixture in the center of a 12mm diameter rounded coverslip, and then placed it on top of the treated square coverslip. The top layer was fabricated in the same manner, but this one contained 0.03% carboxylate modified red latex beads of 0.1$\mu$m diameter (Fluospheres, Invitrogen, Carlsbad CA). We put 2.5$\mu$l of this mixture on top of a 12mm diameter rounded coverslip, and we placed it on top of the bottom layer, in this way all the beads are located in a very thin layer on the surface of the gel. The gels fabricated in this way have a stiffness around 900 Pa [89]. The two layers were verified to adhere well to each other under experimental conditions by confirming continuous registration of the two layers using gels with beads of a second color in the bottom layer. We mounted the coverslips with the gels in Petri dishes with a circular opening in the bottom using silicon grease (Dow Corning, Midland, Michigan).

Finally, we made the gels physiologically compatible by cross-linking collagen I to the surface of the polyacrylamide. We used 1mM Sulfo-SANPAH (Thermo Sci, Rockford, Il) after UV activation to cross-link 0.25mg/ml collagen I. The gels were incubated overnight at room temperature. After washing, the gels were stored in Na/K phosphate buffer (9.6mM KH2PO4, 2.4mM Na2HPO4, pH 6.3, same composition as used in the experiments) and antibiotic (40$\mu$M Ampicillin) for up to a week.

We measured substrate thickness by locating the top and bottom planes of the gel and subtracting their z positions. We located the top plane by maximizing the number of in-focus pixels of cell outlines [90] and the bottom plane by focusing on streaky patterns left on the surface

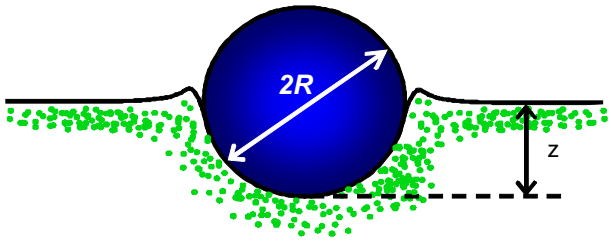


**Figure 2.1**: Sketch of the method that we used to measure the Young's modulus of the substrate with the calculation of the indentation produced by a tungsten carbide ball.

of the glass coverslip during treatment for gel attachment. The thickness of these gels is around 40$\mu$m. The Young modulus ($\sim$ 900Pa) was verified by measurements of the indentation of a tungsten carbide sphere [91] and independently through atomic force microscopy (AFM).

## 2.5 Measurement of the Young's modulus of the substrate

To verify that the published values of the gels' elasticity corresponded to the ones in our substrates, we performed sphere indentation experiments and also used AFM measurements. The Young's modulus of the substrate is determined by measuring the static indentation depth, $\Delta z$, of a tungsten carbide sphere (R=150$\mu m$, W=1.898$\mu N$, Hoover Precision, East Gramby, CT, USA) slowly deposited on the substrate [91]. Figure 2.1 shows a sketch of the experimental procedure used to measure the indentation created by the ball. We applied the equation found by Keer [91] that calculates the Young's Modulus, $E$, as a function of the thickness, $h$, the indentation depth, $z$, the radius, $R$, the apparent weight of the sphere, $W$ and the Poisson ratio, $\sigma$:

$$E = \frac{3(1-\sigma^2)WR}{4{a_0}^3} \tag{2.1}$$

where $a_0$ is solved from:

$$z = \frac{{a_0}^2}{R}[1 - 0.504\frac{a_0}{h} - 0.225\left(\frac{a_0}{h}\right)^3 - 0.098\left(\frac{a_0}{h}\right)^5] \tag{2.2}$$

We determined $z$ as the depth where the beads displaced by the carbide sphere came

into focus in a z-stack of images with a distance between planes of 0.4$\mu$m. The in-focus beads were detected using the SOBEL function in MATLAB. The Young's modulus obtained in our experiments has an average of 910Pa and a standard deviation of 360Pa.

## 2.6 Computational analysis of the accuracy obtained in the measurements of the displacement field

The point spread function (PSF) is the image of a point that is created by an optical system and it describes the distribution in three dimensions of light originating from a dimension-less spot. The core of the diffraction pattern has an ellipsoid shape, and that controls the optical resolution. For confocal sectioning, the goal is to transmit only the inner core of the PSF, which defines the optical section. The distance in z that connects the 50% intensities on both sides of an intensity profile is called the full width half maximum (FWHM), and by convention this is used as a measure of the thickness of optical sections. The FWHM for the microscope that we used in our experiments is shown in Figure 2.2 and its value is 1.4$\mu$m. Therefore, the images that we acquire with the microscope are a convolution of the actual images and the PSF of the microscope, which poses a limitation for the accurate measurement of the displacements in the vertical direction.

In order to quantify the accuracy of our method in the calculation of the displacement field exerted by the cells, we studied systematically the error that was made. We imposed a simulated displacement field of magnitude similar to the displacement field applied by *Dictyostelium* cells to the substrate. In this way, we knew the exact value of the displacement field in each point of the substrate, then we calculated the displacement field obtained with our method based on correlation techniques, and the error made in the result obtained with respect to the exact displacement field imposed. We defined this error as the imposed displacement field minus the displacement field obtained divided by the displacement field imposed.

$$error = \frac{< |u_{exact} - u_{calculated}| >}{< |u_{exact}| >} \cdot 100 \tag{2.3}$$

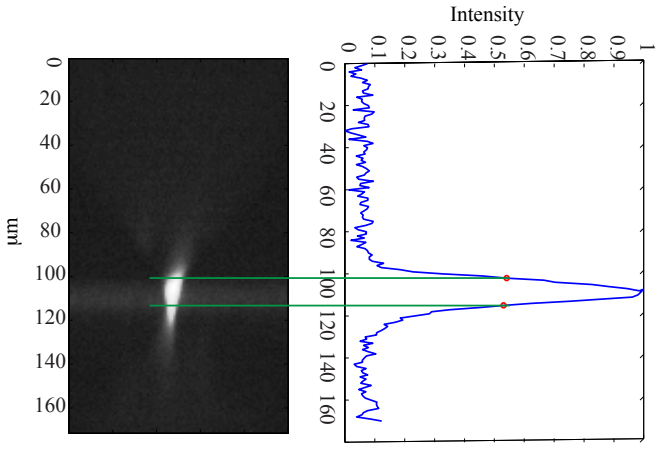


**Figure 2.2**: Point spread function of the specific microscope that we used in the experiments. The two red dots indicate the full width half maximum of the microscope.

We tried some treatments of the images, as well, to investigate if the processing of the images gave a better result for the displacement calculation using our method. The techniques that we used for the processing of the images were:

- Mean normalization: We normalized the images acquired with their mean intensity.
- Contrast enhancement: We normalized the image contrast using a min-max filter that determined the upper and lower envelopes of the image intensity, subtracted the lower envelope and then normalized the image intensity with respect to the difference between the upper and lower values. We imposed a minimum contrast value to avoid too small normalization values.
- Interpolation: We interpolated the images in order to have more planes in between the actual planes.

For a z-stack of images acquired with our microscope of a substrate with beads embedded in all the volume in which the intensity distribution is the one shown in Figure 2.3, we imposed the displacement fields shown in Figure 2.4 , and calculated the error that was made with our method, using eq. 2.3.

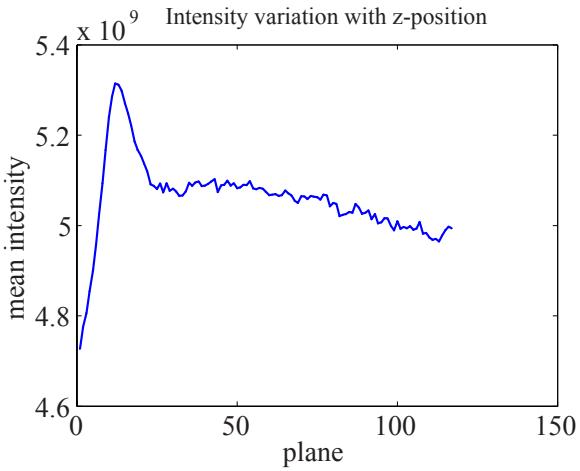


**Figure 2.3**: Intensity variation with z of the images in the z-stack analyzed. The peak intensity is located in the surface of the gel, and the intensity decays towards the interior of the gel.

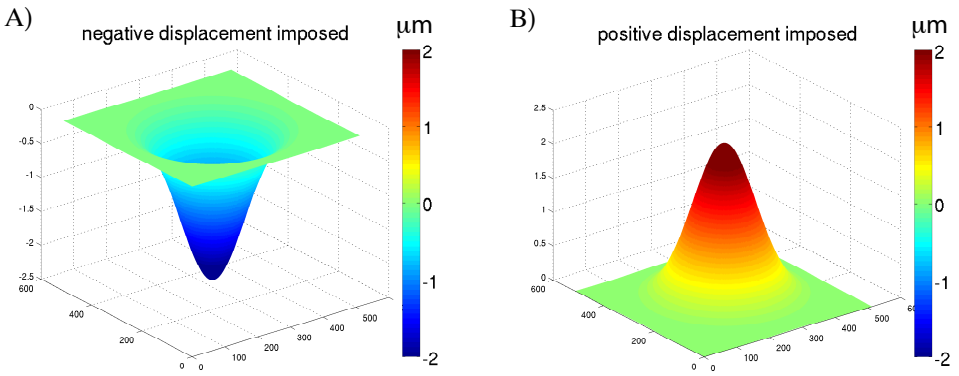


**Figure 2.4**: Simulated displacement fields imposed for the posterior calculation with our method. A) Negative displacement field imposed. B) Positive displacement field imposed.

Figure 2.5A shows the error made when the total z-distance acquired to be used for the displacement field calculation is 30$\mu$m, and the planes have a different separation between them, which results also in a different number of planes acquired. We observed that there is a maximum value in the distance between planes that is equal to 1$\mu$m to obtain accurate displacement fields (Figure 2.5A). When the distance between planes in higher than 1$\mu$m, the error made in the calculation of the displacement field is large. This limitation of the z-distance between planes is due to the section thickness of the microscope.

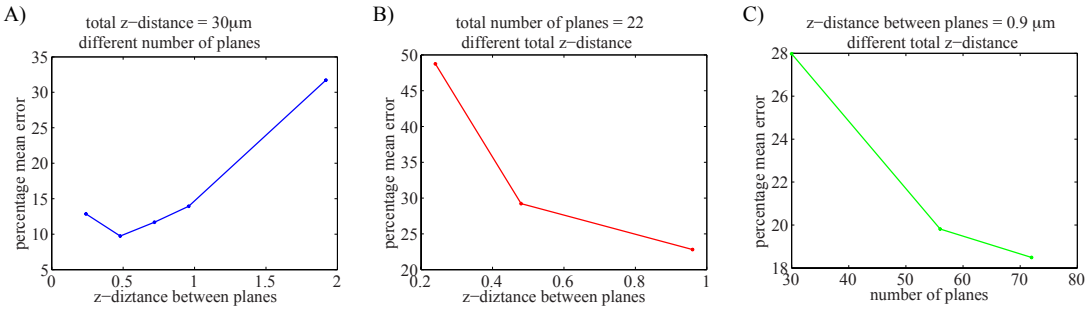


**Figure 2.5**: Percentage mean error calculated using eq. 2.3 for the simulated displacement fields imposed to the substratum. A) Percentage mean error as a function of the z-distance between planes, when the total range of images has a depth of 30$\mu$m in z and therefore the number of planes changes for each z-distance between planes. B) Percentage mean error as a function of the z-distance between planes, when the total number of planes used in the calculation is equal to 22 and therefore the total range of distance in z varies for each z-distance between planes. C) Percentage mean error as a function of the number of planes, when the z-distance between planes is equal to 0.9$\mu$m and therefore the total range of distance in z varies for each number of planes used in the calculation.

Figure Figure 2.5B shows the error made in the calculation of the displacement field when we acquired a total of 22 planes, and we varied the z-distance between planes, which results on a variation of the total z-distance acquired. We observed that the error decreased when the separation between planes increased and therefore when the total z-distance acquired increased, until we reached the limit of 1$\mu$m (Figure 2.5B).

Figure 2.5C shows the error made in the calculation of the displacement field when used a fix z-distance between planes equal to 0.9$\mu$m and we varied the number of planes used, which resulted in a variation of the total z-distance used in the calculation, as well. In this case, we observed that the error decreased when the number of planes used increased, and therefore we were capturing a bigger range of the substrate's thickness since the total z-distance used for the calculation increased (Figure 2.5C).

Therefore, the conclusion after this systematic study of the error was that in order to calculate the displacement field exerted by the cells in an accurate manner, we needed to use all the planes in which there is bead information.

Consequently, there are three requirements for the image acquisition in our experiments to obtain accurate displacement fields. The first one is that we need to acquire the whole thickness

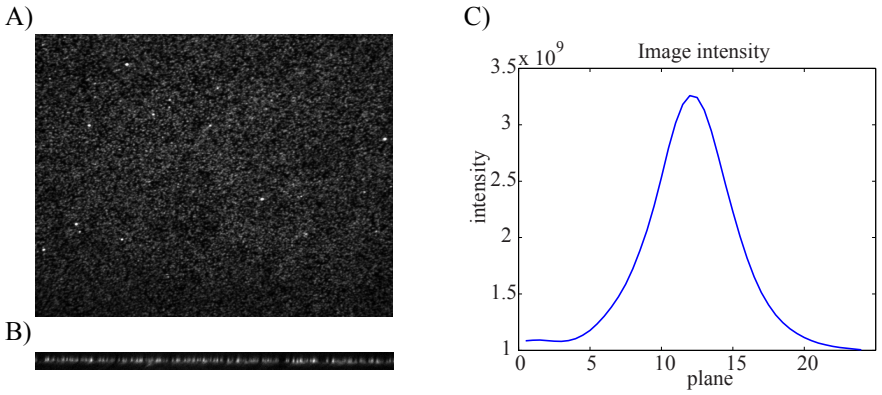


**Figure 2.6**: Representative substrate used in our experiments. A) In-plane view of the beads' distribution in the surface of the substrate. B) Side view of the substrate. The beads are located in a thin layer in the center of the z-stack. C) Intensity profile of the z-stack. The beads are located in the center of the z-stack and we acquire all the range in which there are beads.

of the substrate in which there are beads. The second is that we can not acquire too many planes, in order to be able to image the whole z-stack fast and to avoid phototoxic effects. And the third is that we need to use a small distance between planes to get an accurate result of the displacement field (Figure 2.6A-B). The solution to achieve all these requirements was to put beads only in a thin layer on the surface of the substrate, so that in less than 9$\mu$m we acquired all the beads' information.

For the images in which the beads were located in the surface of the substratum, we acquired a z-stack of images and the section containing the beads was located in the center of the z-stack, as shown in Figure 2.6A-B and in the intensity profile of the image z-stack shown in Figure 2.6C. The maximum intensity of the z-stack was located in the center and we acquired all the information of the beads in the whole stack (Figure 2.6C). Figure 2.7A-B shows the error made when using these images in the displacement fields in the normal and tangential direction to the substrate, when using different image treatments and z-distance between planes. When we acquired the total thickness in which there were beads, the error made was low in the horizontal and vertical directions until a distance between planes of 0.7$\mu$m. When we took only 8 planes the error was big in the vertical direction when the distance between planes was small because

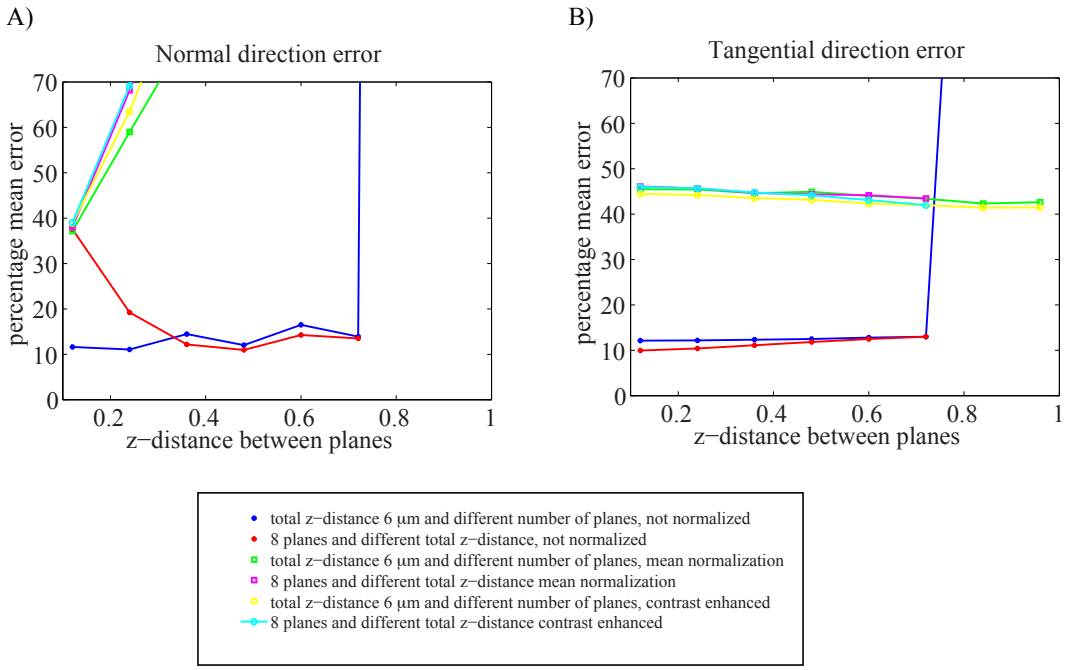


**Figure 2.7**: Percentage mean error for the substrate shown in Figure 2.6. A) Percentage mean error calculated using eq. 2.3 for the displacement field in the normal direction to the substrate for different image treatments and z-distance between planes. B) Percentage mean error calculated using eq. 2.3 for the displacement field in the tangential direction to the substrate for different image treatments and z-distance between planes.

we were getting only a small range of the bead distribution, whereas the error in the horizontal direction was not affected. The treatment of the images didn't provide improved results.

## 2.7 Calculation of the deformation field

The three-dimensional deformation applied by the cells to the substrate was measured from the displacements experienced by the 0.1$\mu$m fluorescent beads embedded in the elastic substrate. We measured the 3D deformation of the substrate by imaging a thin layer of the substrate surface where the fluorescent beads were located by using a confocal microscope. We imaged a z-stack consisting of 24 planes separated 0.4$\mu$m from each other and acquired images every 5 seconds. This deformation was measured in the three dimensions through a method similar to Particle Image Velocimetry (PIV) [92][93] based on correlation techniques. We calculated the

substrate deformation through the cross-correlation of each instantaneous image z-stack in which the substrate was deformed by the moving cells and a non-deformed z-stack used as reference. In each experiment, the reference z-stack was obtained after the cell moved out of the field of view, which was easy to achieve, as *Dictyostelium* cells are highly motile. For the experiments with *ctxA*$^{-}$*/B*$^{-}$ cells treated with 50$\mu$M blebbistatin, which do not move, we needed to detach the cells to acquire the reference image. In order to detach the cells we added 2% Sodium dodecyl sulfate (SDS), and waited for the cells to detach to acquire the reference image.

The instantaneous and reference z-stacks were divided into 3D interrogation boxes of size 16x16x24 pixels in the x, y and z directions, to balance resolution and signal-to-noise while minimizing phototoxic effects. We defined the signal to noise ratio as the ratio between the maximum and the mean values of the cross-correlation. We chose the horizontal size of the interrogation boxes in order to balance resolution, which decreases with box size, and signal to noise ratio, which increases with box size. We chose the smallest box which gave a signal to noise ratio bigger than 4.5. The size, $\Delta$x and $\Delta$y, of the interrogation window was 16 pixels, which was the smallest value that gave a signal to noise ratio bigger than 2.5, with a 50% overlap. These settings provided a Nyquist spatial resolution of 2$\mu$m. The distance between planes and number of planes was chosen in order to obtain accurate values of the vertical displacement field and also to avoid phototoxic effects, for this we used 24 planes and $\Delta_{\text{Z-stack}}$= 0.4$\mu$m, which satisfies the requirements explained in 2.6. The subpixel resolution was obtained through 3D gaussian interpolation of the correlation function by minimizing the norm of the parabolic fit to the logarithmic values of the correlation function.

## 2.8 Identification of the cell contour

Cell contours were determined from differential interference contrast (DIC) images. The image processing was performed with MATLAB (Mathworks Inc, Natick, MA). First we removed the static imperfections and bright non-uniformity by using the average image of the time-lapse series. We applied a threshold to the resulting image in order to obtain the most intense structures

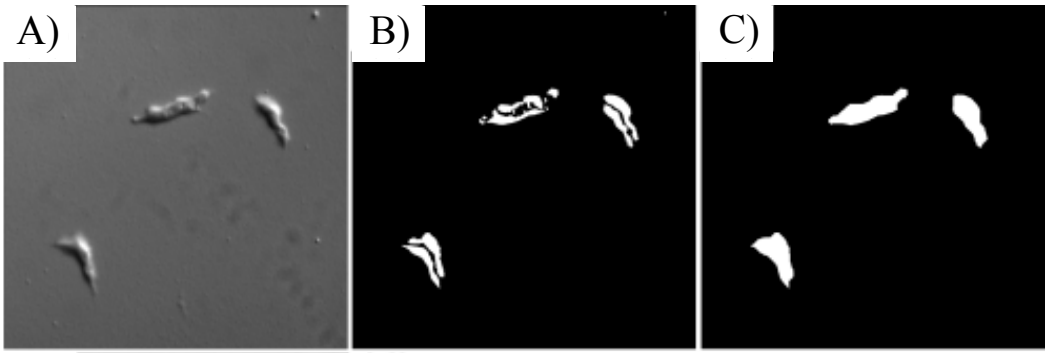


**Figure 2.8**: Contour identification process. A) Differential Interference Contrast (DIC) image acquired with the microscope. B) Contour detection after the application of one dilation and erosion. C) Contour detection after the application of two dilations and erosions.

of the image and subsequently applied two dilations and erosions to obtain the contour of the cell. Figure 2.8A-C shows the process for the identification of the cell contour. Figure 2.8A shows the DIC image acquired with the microscope, while Figure 2.8B-C shows the contour detection after the application of one and two dilations and erosions, respectively. The coordinates of the centroid and the principal axes of each cell were calculated using standard MATLAB functions.

## 2.9 Calculation of the traction forces exerted by the cells in two dimensions

The traction forces were calculated by solving analytically the elasticity equation of equilibrium for a linear, homogeneous, isotropic element of thickness $h$ in a Cartesian coordinate system with the $x$ and $y$ axes parallel to the base of the substrate, which was located at $z = 0$. When a cell migrates over the flat substrate, it generates a displacement field, $\vec{u} = (u, v, w)$. The measurement plane was located at a distance from the surface $h_0$. The equations governing the displacement field are:

$$\frac{\nabla(\nabla \cdot \vec{u})}{(1-2\sigma)} + \Delta\vec{u} = 0 \tag{2.4}$$

The boundary conditions are no slip at the bottom of the substrate, $\vec{u} = 0$ at $z = 0$, since

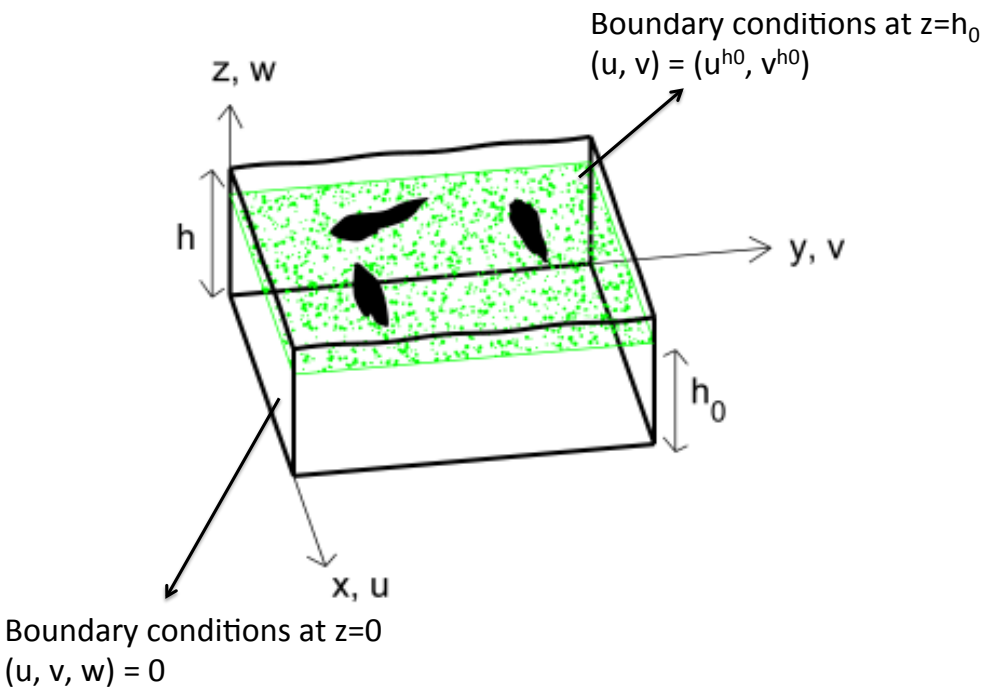


**Figure 2.9**: Experimental configuration of the experiments and boundary conditions used for the calculation of the traction forces exerted by the cells in the substrate in two dimensions.

the substrate is attached to a glass coverslip, and the measured displacements at the surface, $(u^{h_0}, v^{h_0})$ at $z = h_0$ (Figure 2.9). The other boundary condition is the assumption that the traction forces exerted by the cells in the perpendicular direction to the substrate surface are negligible, this is $\tau_{zz} = 0$ at $z = h$. We assume periodicity in the horizontal directions and solve the elastostatic equation analytically by using Fourier series [90]:

$$(u, v, w) = \sum_{\alpha=-\infty}^{\infty} \sum_{\beta=-\infty}^{\infty} [\hat{u}_{\alpha,\beta}(z), \hat{v}_{\alpha,\beta}(z), \hat{w}_{\alpha,\beta}(z)] exp(i\alpha x) exp(i\beta y) \tag{2.5}$$

where $\alpha$ and $\beta$ are the wave numbers in the $x$ and $y$ directions, and $\hat{u}_{\alpha,\beta}(z)$, $\hat{v}_{\alpha,\beta}(z)$, $\hat{w}_{\alpha,\beta}(z)$ are the complex Fourier coefficients of $u$, $v$, $w$.

We obtain a first-order ordinary differential equation for the z-functional form of these Fourier coefficients:

$$\frac{d\hat{u}_{\alpha,\beta}}{dz} = A_{\alpha,\beta}\hat{u}_{\alpha,\beta} \tag{2.6}$$

where:

$$\hat{u}_{\alpha,\beta} = \begin{bmatrix} \hat{u}_{\alpha,\beta} \\ \hat{v}_{\alpha,\beta} \\ \hat{w}_{\alpha,\beta} \\ \frac{\hat{du}_{\alpha,\beta}}{dz} \\ \frac{\hat{dv}_{\alpha,\beta}}{dz} \\ \frac{\hat{dw}_{\alpha,\beta}}{dz} \end{bmatrix} \tag{2.7}$$

and $A_{\alpha,\beta}$ is a matrix, whose coefficients only depend on $\alpha$, $\beta$ and $\sigma$ and was found by del Álamo et al. [90].

We obtained the Fourier coefficients of the tangential stress field on the surface of the substrate through the constitutive equations by using the Fourier coefficients of the displacement field and its z-derivatives, obtained from the solution of eq. 2.6 with the aforementioned boundary conditions:

$$\hat{\tau}_{zx\alpha,\beta}(h) = \frac{E}{2(1+\sigma)}[\frac{d\hat{u}_{\alpha,\beta}}{dz}(h) + i\alpha\hat{w}_{\alpha,\beta}(h)] \tag{2.8}$$

$$\hat{\tau}_{zy\alpha,\beta}(h) = \frac{E}{2(1+\sigma)}[\frac{d\hat{v}_{\alpha,\beta}}{dz}(h) + i\beta\hat{w}_{\alpha,\beta}(h)] \tag{2.9}$$

The inverse Fourier transform of the traction forces coefficients on eq. 2.8 and eq. 2.9, gave the two dimensional stress field exerted by the cell on the substrate surface .

We developed a method to calculate the traction forces exerted in the perpendicular direction to the substrate in addition to the in-plane traction forces. To do this, we measured the three-dimensional deformation of the substrate on a thin layer near its surface, and input this information into an exact analytical solution of the elastostatic equation.

## 2.10 Three-dimensional force microscopy: calculation of the forces exerted by the cells in the three dimensions

The three-dimensional forces exerted by the cells on the substrate were measured using the three-dimensional Fourier Force Microscopy method described by del Álamo et al. [43]. We measured the three-dimensional deformation of the substrate by imaging a thin layer of the substrate surface where the fluorescent beads were located by using a confocal microscope, as explained in section 2.7. We computed the three-dimensional stresses (force per unit area) generated by the cells on the substrate using the 3D Green's function of the elastic equation of equilibrium for a linear, homogeneous, isotropic three-dimensional body, in a similar way as it was done for the calculation of the two-dimensional traction forces (section 2.9). However, in this case we used as boundary conditions the three-dimensional displacement field measured at the surface of the substrate for all three directions, $(u^{h_0}, v^{h_0}, w^{h_0})$ at $z = h_0$, and zero displacement at the bottom of the substrate, $\vec{u} = 0$ at $z = 0$, for all three directions, as shown in Figure 2.10, without need of any assumptions.

The 3D Green's function used to calculate the three dimensional forces was given in closed analytical form in the Fourier domain by del Álamo et al. [43]. We obtained the Fourier coefficients of all the stress tensor components by using the constitutive equations for linear elasticity, and then we performed the inverse Fourier transform to obtain the stress field in the real space. Given that our Fourier method does not enforce zero stress values outside the cell boundaries, the finite spatio-temporal resolution of the deformation measurements may lead to small non-zero values outside of the cell for relatively small, fast moving cells such as *Dictyostelium*.

With our 3D method we calculated all the components of the stress tensor, and the stresses exerted on the surface of the substratum through the Cauchy law:

$$\tau = \bar{T} \cdot \vec{n} \tag{2.10}$$

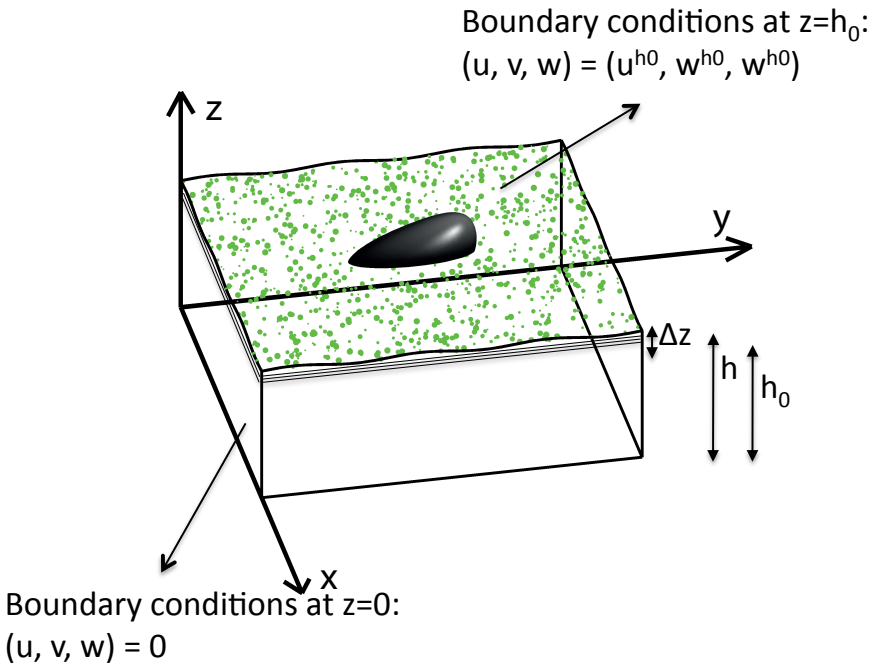


**Figure 2.10**: Experimental configuration of the experiments and boundary conditions used for the calculation of the traction forces exerted by the cells in the substrate in the three dimensions.

where $\bar{T}$ is the three-dimensional stress tensor and $\vec{n}$ is the unit vector normal to the surface of the substrate.

The surface of the substrate when it is deformed by a cell, $z$, can be defined as a constant thickness $h$, plus the displacements exerted by the cell over the substrate in the z-direction.

$$z = h + w(x, y, h) \tag{2.11}$$

Therefore, the expression that defines the the normal vector to the deformed substrate is given by:

$$\vec{n} = \frac{(\partial_x w, \partial_y w, 1)}{\sqrt{(\partial_x w)^2 + (\partial_y w)^2 + 1}} \tag{2.12}$$

The stresses in the perpendicular, $\tau_n$, and tangential, $\tau_t$, directions to the deformed substrate are obtained following Cauchy's law:

$$\vec{\tau}_n = (\vec{n}^T \cdot \bar{T} \cdot \vec{n})\vec{n} \tag{2.13}$$

$$\vec{\tau}_t = (\bar{T} \cdot \vec{n}) - \vec{\tau}_n \tag{2.14}$$

In our experiments the values of $\partial_x w$ and $\partial_y w$ are small, ranging between 0.05 and 0.1. Thus, $\vec{n} \simeq (0,0,1)$, and the normal and tangential stresses can be approximated by $\tau_n = (0,0,\tau_{zz})$ and $\tau_t = (\tau_{zx}, \tau_{zy}, 0)$.

The Fourier coefficients of the tangential stresses, $\tau_{zx}$ and $\tau_{zy}$ are given by eqs. 2.8 and 2.9 respectively. And the Fourier coefficients of the normal stresses exerted by the cells on the surface of the substratum, $\tau_{zz}$, are calculated as follows:

$$\hat{\tau}_{zz\alpha,\beta}(h) = \frac{E}{(1+\sigma)(1-2\sigma)}(\sigma i\alpha\hat{u}_{\alpha,\beta} + \sigma i\beta\hat{v}_{\alpha,\beta} + (1-\sigma)\frac{d\hat{w}_{\alpha,\beta}}{dz}) \tag{2.15}$$

where $E$ is the substrate Young modulus and it was computed as shown in section 2.5 and $\sigma$ is the Poison ratio of the substrate and was set equal to 0.45. There is a wide range of measurements in the literature for the Poisson ration, $\sigma$, ranging from 0.3 to 0.49 [94] [95] [96]. We choose this value, which is a typical value chosen for TFM studies [97] [98].

## 2.11 Comparison of the traction forces obtained by using the 2D and 3D Force Microscopy methods

The measurement of the perpendicular forces to the substrate reveals that this out-of-plane component of the forces is as large as the in-plane component or even larger, and therefore it cannot be neglected. The 2D method is not accurate when calculating the tangential traction forces due to the incorrect assumption that $\tau_{zz} = 0$. The error made when applying the 2D method to the measurement of the tangential traction forces is generally high. We can now characterize the validity of the results obtained with the 2D method described in section 2.9, that calculates the traction forces in the substrate plane, but neglects the out-of-plane component of the traction stresses, through the comparison with the results obtained by using our 3D method described in section 2.10.

We found that the error made in the calculation of the tangential traction forces with the

2D method depends on the value of several elements involved in the experiment, such as cell size, substrate thickness and Poisson ratio. The main parameters that determine the differences between the tangential forces measured with the 2D and 3D methods are the ratio between the cell length and substrate thickness, $\Delta/h$, the Poisson ratio of the substrate, $\sigma$, and the ratio between the magnitudes of the in-plane and the out-of-plane displacements generated by the cells in the substrate, $W_0/U_0$.

In most of the cases, the error of the horizontal traction forces calculated with 2D methods is large. Only by using some specific combinations of these parameters we found that the error of the horizontal traction forces measured with the 2D method is small, and the measurements are not highly affected by neglecting the out-of-plane component of the forces [43]. The two experimental configurations in which the error made with the 2D method is not large are given for specific values of the ratio between the cell length and substrate thickness and the Poisson ratio. This is the case when the Poison ratio, $\sigma$, is close to 0.5, and the ratio between cell length and substrate thickness, $\Delta/h$, is less than 1. Another configuration that gives small differences is given when $\Delta/h$ is large, 100 or larger, and $\sigma$ is lower than 0.3. Regarding the ratio between the magnitude of out-of-plane displacements and in-plane displacements, there are specific cases in which the error of the measurements calculated with the 2D method is small. This condition occurs when the ratio between the magnitude of the out-of-plane and in-plane displacement fields, $W_0/U_0$, is very low. One case is when $W_0/U_0 < 0.2$ and $\Delta/h < 10$ and another case is when $\sigma$ is close to 0.5 [43]. In our experiments $\sigma$ is close to 0.5 and $\Delta/h$ is lower than 1. In this manner these conditions are included into one of the cases in which the error is not large.

To obtain an estimation of the error made with our 2D method for the tangential traction forces exerted by *Dictyostelium* cells moving over the polyacrylamide substrates of approximately 40$\mu$m thickness, we calculated the tangential forces with our 3D method and compare them to the 2D method. The tangential stresses are calculated in both the 2D and 3D method as:

$$\tau_t = \sqrt{\tau_{zx}^2 + \tau_{zy}^2} \tag{2.16}$$

The error in the tangential stresses calculated with the 2D method can be defined as follows:

$$error_t = \left[ \frac{\int\int [\tau_t^{2D}(x,y,h) - \tau_t^{3D}(x,y,h)]^2 dxdy}{\int\int [\tau_t^{3D}(x,y,h)]^2 dxdy} \right]^{1/2} \cdot 100 \tag{2.17}$$

Where $\tau_t^{2D}$ are the tangential stresses calculated with our 2D method and $\tau_t^{3D}$ are the tangential stresses calculated with our 3D method. This definition of the error is normalized in a way that $error_t$ would be 100% if $\tau_t^{2D}$ is 0 and $\tau_t^{3D}$ is different than 0.

We calculated the traction forces in the tangential direction to the substrate, $\tau_t$, exerted by a representative wild-type *Dictyostelium* cell, using our 3D method and compared to the tangential traction forces calculated for the same cell by using our 2D method. Figure 2.11A-B shows the average traction forces in the horizontal plane for a wild-type cell that are obtained with our 3D and 2D methods. Figure 2.11C shows the error that is made by using the 2D method for this cell at each point. The 2D method underestimates the axial forces, parallel to the cell's major axis, and overestimates the lateral forces, perpendicular to the cell's major axis. The error estimated through eq. 2.17, that is made in the calculation of the tangential traction forces by using the 2D method for this cell is 21.2%.

The strain energy deposited by the cell in the substratum is equal to the mechanical work exerted by the cell and it can be determined using the principle of virtual work. The strain energy exerted by the cell, when calculating the stresses in the three directions, is defined as:

$$U_{s\,total} = \frac{1}{2} \int_0^L \int_0^W [\tau_{zx}(z=h) \cdot u(z=h) + \tau_{zy}(z=h) \cdot v(z=h) + \tau_{zz}(z=h) \cdot w(z=h)] dxdy \tag{2.18}$$

where $L$ is the length of the cell and $W$ is the width of the cell.

This total strain energy can be decomposed in its normal, $U_{sn}$, and tangential components, $U_{st}$, in order to compare the results for the tangential strain energy obtained with our 3D method and the results for the total strain energy calculated with our 2D method. The tangential component

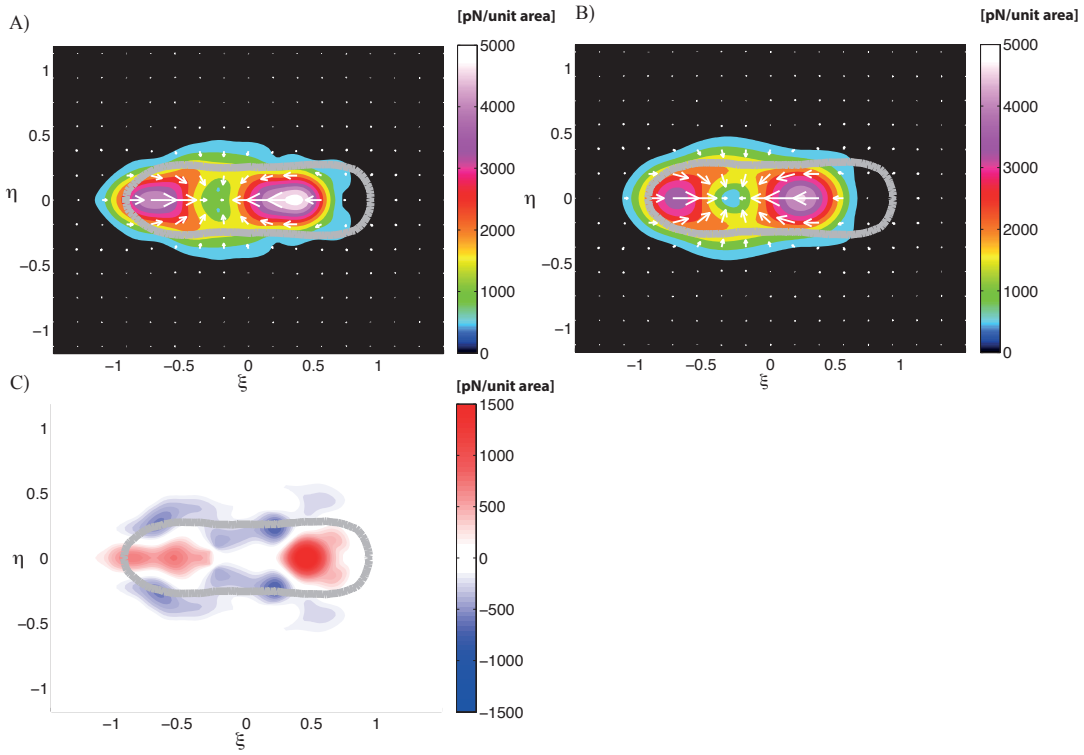


**Figure 2.11**: Comparison of the forces applied by a representative cell in the tangential direction to the substrate when using 2D and 3D methods. A) Tangential traction forces obtained by using the 3D method for a representative *Dictyostelium* cell. B) Tangential traction forces obtained by using the 2D method for the same cell shown in panel A. C) Difference between the horizontal traction forces calculated by using the 3D and 2D methods for this representative *Dictyostelium* cell. The red color indicates that the traction forces calculated with the 3D method are bigger than the ones calculated with the 2D method, and the blue color indicates the opposite, that the traction forces calculated with the 3D method are lower than the ones calculated with the 2D method.

of the strain energy is defined as:

$$U_{st} = \frac{1}{2}\int_0^L \int_0^W [\tau_{zx}(z=h)\cdot u(z=h) + \tau_{zy}(z=h)\cdot v(z=h)]dxdy \tag{2.19}$$

And the normal component of the strain energy is defined as:

$$U_{sn} = \frac{1}{2}\int_0^L \int_0^W [\tau_{zz}(z=h)\cdot w(z=h)]dxdy \tag{2.20}$$

The definition of the tangential strain energy in this way, eq. 2.19, is equivalent to the

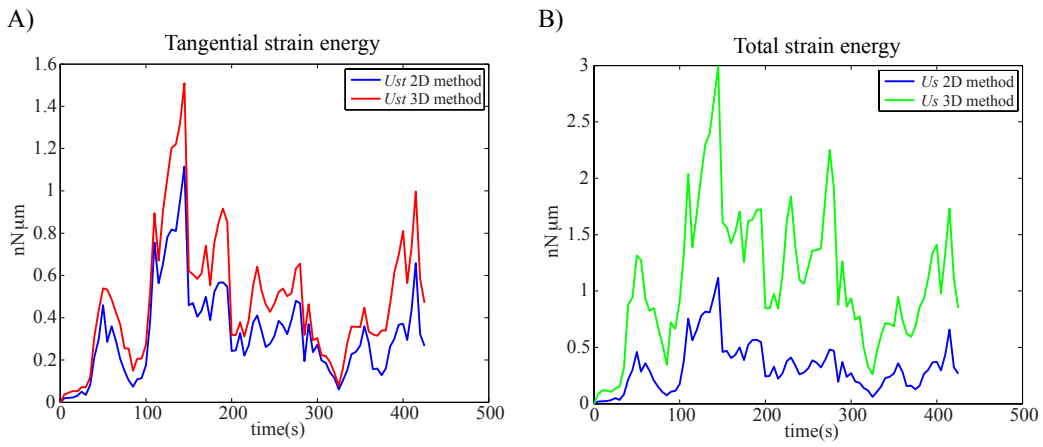


**Figure 2.12**: Comparison of the strain energy calculated using our 2D and 3D methods. A) Tangential strain energy evolution over time, calculated with our 2D and 3D methods for a representative *Dictyostelium* cell. B) Total strain energy evolution over time, calculated with our 2D and 3D methods, applied by the same *Dictyostelium* cell as in panel A.

definition of the total strain energy exerted by the cell when using our 2D method. Figure 2.12A shows the evolution of the total elastic energy calculated by using the 2D method and the tangential strain energy calculated with the 3D method over time for this specific wild-type cell. In the specific case of our experimental conditions, the measurement for the total strain energy calculated with our 2D method is not very different from the tangential strain energy calculated with our 3D method, mainly because the cell length is smaller than the substrate thickness. This may not be the case for a different type of cell and a different substrate. However, the total strain energy measured through our 3D method is the sum of both contributions $U_{st}$ and $U_{sn}$. Therefore, the total strain energy is largely underestimated with our 2D method (Figure 2.12B), and the error made in the magnitude is around 80% when using this method.

## 2.12 Calculation of the elastic energy exerted by the cells on the substrate

The strain energy exerted by the cell on the substrate, $U_s$, is equal to the mechanical work that the cell is performing in the substrate when moving. Assuming that the substrate is a hookean

solid, the elastic energy is given by:

$$U_s = \frac{1}{2}\int_S \vec{\tau}(z=h)\cdot\vec{u}(z=h)dS \tag{2.21}$$

where $\vec{\tau} = (\tau_{zx}, \tau_{zy}, \tau_{zz})$, are the stresses exerted by the cell on the substrate and $\vec{u} = (u, v, w)$, are the displacements applied on the free surface of the substrate. When the stresses applied by the cell to the substrate are calculated in three dimensions, we can calculate the strain energy generated by the tangential stresses ($U_{st}$) and the strain energy generated by the normal forces ($U_{sn}$), as follows:

$$U_{st} = \frac{1}{2}\int_0^L \int_0^W [\tau_{zx}(z=h)\cdot u(z=h) + \tau_{zy}(z=h)\cdot v(z=h)]dxdy \tag{2.22}$$

$$U_{sn} = \frac{1}{2}\int_0^L \int_0^W [\tau_{zz}(z=h)\cdot w(z=h)]dxdy \tag{2.23}$$

## 2.13 Calculation of the motility cycle's period

Amoeboid migrating cells perform a repeated cycle during motion. In order to obtain the period of this motility cycle, first we obtained the main period of the temporal evolution of the strain energy as the time between the first and second peaks of the autocorrelation function, $T_0$. Finally, we obtained the period of the motility cycle by fitting the time records to a sinusoidal function, as follows:

$$f(t) = a\cdot sin(\frac{2\pi}{T}t + c) \tag{2.24}$$

using non-linear least squares. The calculation of the period was constraint using the initial estimate of the period, to have a value between $T_0/2$ and $2T_0$. We observed consistently that the best fit resulted from a sine function of a period similar to the determined with the autocorrelation function.

## 2.14 Cell based reference system

The shape and orientation of the cells are continuously changing in the laboratory coordinate system where the images are obtained. Thus to perform statistical analysis over long periods of time and for many different cells, we calculated the instantaneous stresses in a cell-based reference system which is dimensionless and can be used commonly for all the cells. This procedure has been thoroughly described previously and allowed us to compile robust statistics from many cells at different instants of time [90] [24]. We identified the contour of the cell from the DIC images taken with the microscope in the laboratory reference frame and we computed the principal geometrical axes of the cell contour and their orientation in the laboratory coordinate system. The center of the cell-based coordinate system was located in the centroid of each cell at each instant of time. The coordinates of the center of the cell-based coordinate system in the laboratory coordinate system were: $(x_c(t), y_c(t))$. In the cell-based coordinate system ($\xi$, $\eta$), the axes were parallel to the directions of the principal axes of each cell at each instant of time. The direction of the horizontal $\xi$-axis followed the direction of the major axis of each cell with the cell front pointing in the positive direction, and all spatial coordinates were rescaled with the half length of the cell $L(t)/2$, making the cell-based reference system dimensionless, as shown in Figure 2.13. The ($\xi$, $\eta$) coordinates can be expressed mathematically as:

$$\xi = \frac{(x - x_c(t))cos(\theta(t)) + (y - y_c(t))sin(\theta(t))}{L(t)/2} \tag{2.25}$$

$$\eta = \frac{(y - y_c(t))cos(\theta(t)) - (x - x_c(t))sin(\theta(t))}{L(t)/2} \tag{2.26}$$

where $x$ and $y$ were the coordinates in the laboratory coordinate system, and $\theta(t)$ was the angle between the major principal axis of the cell and the x-axis of the laboratory coordinate system, as shown in Figure 2.13A, E.

To obtain the average stresses, we converted the instantaneous stresses into the cell-based coordinate system $(\xi, \eta)$. Since the distance was scaled with $L(t)/2$ in the cell-based coordinate

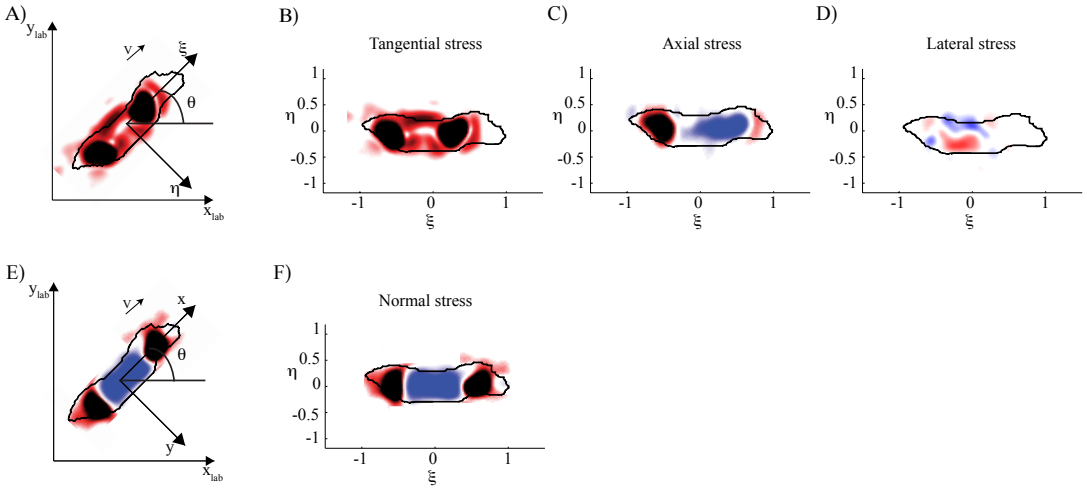


**Figure 2.13**: Calculation of the three components of the stresses in the cell based reference system. A) Tangential stresses calculated in the laboratory-based reference system. B) Tangential stresses calculated in the cell-based reference system. C) Axial stresses, x-component of the tangential stresses (tangential stresses in the direction of the major axis of the cell), calculated in the cell-based reference system. D) Lateral stresses, y-component of the tangential stresses (tangential stresses in the perpendicular direction to the major axis of the cell), calculated in the cell-based reference system. E) Normal stresses calculated in the laboratory-based reference system. F) Normal stresses calculated in the cell-based reference system.

system, the longitudinal axis of the cell spanned from ξ=-1 to ξ=1. The dimensions of the stresses in this coordinate system needed to be consistent with the fact that their surface integral is a force. Therefore the forces were scaled with $[L(t)/2]^2$ and have dimensions of force.

## 2.15 Calculation of correlation coefficients

In order to determine the relationship between the tangential and normal forces we determined the correlation coefficient between the location of the tangential and the positive normal forces over time and between the temporal evolution of the magnitudes of the tangential and normal forces. Additionally, to study the relationship between the nucleus and the negative compressive normal forces, we determined the correlation coefficient between the location of the nucleus and the location of the negative compressive normal forces. We calculated the correlation coefficients in the cell-based coordinate system in order to avoid any influence of the distance that

the cell has moved in space. In this way, the cell contour was determined in the laboratory-based reference system and we determined the principal geometrical axes of the cell. The cell-substrate stresses were calculated in Cartesian coordinates $(\tau_{zx}, \tau_{zy}, \tau_{zz})$ and rotated such that the cell major axis was parallel to the vertical direction. Then, we calculated the axial tension, $T_\xi(\xi,t)$, in the cell-based coordinate system by integrating the x-component of the traction stresses in the cell based reference system across the cell width (y-direction) at each instant of time, and the normal tension, $T_z(\xi,t)$, by integrating the z-component of the stresses in a similar manner, i.e.

$$T_\xi(\xi,t) = \int_{\eta_1}^{\eta_2} \tau_{z\xi}(\xi,\eta,t)d\eta \tag{2.27}$$

$$T_z(\xi,t) = \int_{\eta_1}^{\eta_2} \tau_{zz}(\xi,\eta,t)d\eta \tag{2.28}$$

The axial and normal tensions, $T_\xi(\xi,t)$ and $Tz(\xi,t)$, defined this way have dimensions of force per unit length and typically are of the order of nN/$\mu$m. Using these data, we determined the position of the maximum axial tension in the front and back halves of the cells, the position of the maximum normal tension in the front and rear halves of the cell and the position of the minimum normal tension in between the regions of positive normal tension. To calculate the correlation between the spatio-temporal evolution of the tangential and normal stresses, we calculated the Spearman correlation coefficient for these two signals. To calculate the correlation coefficient between the location of the negative normal stresses and the location of the cell nucleus, we calculated the Spearman correlation coefficient between the minimum normal tension and the location of the cell's nucleus center. To calculate the correlation coefficient for the temporal evolution of the tangential and normal forces, we calculated the magnitudes of these two signals at each instant of time and determined their Spearman correlation coefficient.

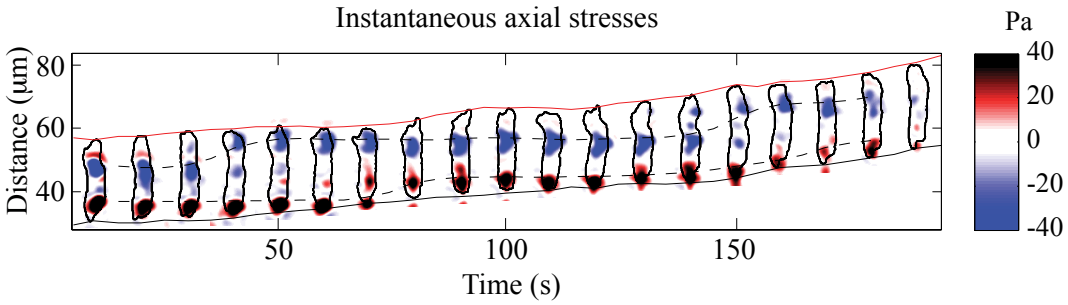


**Figure 2.14**: Kymographic representation of the instantaneous axial stresses exerted by a representative wild-type cell. The solid red line indicates the location of the front of the cell. The solid black line indicates the location of the back of the cell. The dashed black lines indicates the location of the maximum axial tension in the frontal and rear parts of the cell. The instantaneous contour of the cell and axial stresses exerted are plotted every 10 seconds.

## 2.16 Space-time kymographic representation of the stresses

First we obtained the contour of the cell from the DIC images, as explained in section 2.8, and we calculated the major and minor second moments of inertia and the orientation of its axes. We computed the cell-substrate stresses and we rotated them into the cell-based reference system as described in section 2.14. Then, we kept the major axis of the cell aligned to the vertical axis of the kymograph which represents the position of the cell. We constructed the axial stress kymograph by stacking the instantaneous axial stresses coming from consecutive temporal measurements with the time variable in the horizontal axis and the position in the vertical axis, as shown in Figure 2.14. The cell contour was determined and plotted together with the tangential stresses. The locations of the cell front and back were also calculated and plotted. The instantaneous tangential stress kymograph was constructed in the same way but using the measured instantaneous tangential stresses instead of the axial ones and the instantaneous normal stress kymograph was constructed using the measured instantaneous normal stresses.

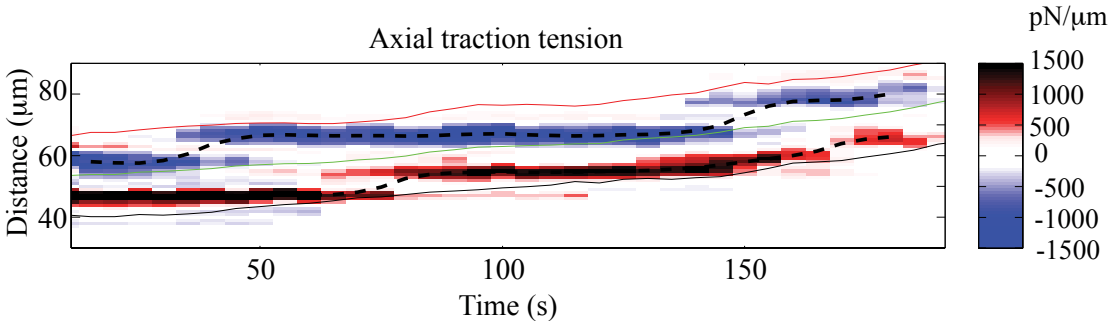


**Figure 2.15**: Kymographic representation of the axial traction tension calculated from the axial stresses exerted by the cell represented in Figure 2.14. The solid red line indicates the location of the front of the cell. The solid black line indicates the location of the back of the cell. The dashed black lines indicates the location of the maximum axial tension in the frontal and rear parts of the cell. The green line indicates the position of the cell's centroid.

## 2.17 Tension kymographic representation

We calculated the contour of the cell from the DIC images, as explained in section 2.8. We calculated the major and minor second moments of inertia and the orientation of its axes. We calculated the cell-substrate stresses and we rotated them into the cell-based reference system as described in section 2.14. We then located the major axis of the cell in a direction parallel to the vertical axis of the kymograph. In this coordinate system we integrated the axial component of the traction stresses across the width of the cell. Therefore the axial traction tension is calculated as follows:

$$T_x(x,t) = \int_{y_1}^{y_2} \tau_{zx}(x,y,t)dy \tag{2.29}$$

And we also integrated the normal component of the stresses across the width of the cell to calculate the normal tension:

$$T_z(x,t) = \int_{y_1}^{y_2} \tau_{zz}(x,y,t)dy \tag{2.30}$$

The axial traction tension kymograph was then constructed by stacking different temporal measurements of $T_x(x,t)$ and plotting them in two dimensions with the time in the horizontal axis and the position in the vertical axis (Figure 2.15). The positions of the maximum axial traction

tension in the front and rear halves of the cells were determined and plotted. The normal tension kymograph was constructed in the same way, but in this case by stacking different temporal measurements of $T_z(x,t)$.

## 2.18 Calculation of the nucleus' volume

We placed cells on a coverslip and waited 20 minutes in order for the cells to adhere to it. Then, we fixed the cells with 3.7% formaldehyde in Na/K phosphate buffer for 5 minutes. Subsequently, the cells were washed 3 times for 5 minutes with PBS and 0.0005% Hoestch in PBS was added during 15 minutes. We then acquired z-stack fluorescent images of the cells' nucleus using a spinning disk confocal microscope (Zeiss) and a cooled charge-coupled device camera (HQ CoolSNAP; Roper Scientific). Using the z-stack images, we performed a 3D reconstruction of the nuclei and calculated their volume using IMARIS software (Bitplane, Zrich, Switzerland).

## 2.19 Calculation of the average F-actin distribution

In order to calculate the actin distribution, we transformed the cells with a vector encoding Lifeact (Abp140 (1-17)-GFP), a 17-amino acid peptide that binds F-actin fused to GFP [99]. In the case of the experiments involving blebbistatin we transformed the cells with a vector encoding this 17-amino acid peptide that binds F-actin fused to RFP. We acquired z-stack of fluorescent images with a confocal microscope (Zeiss) and a cooled charge-coupled device camera (HQ CoolSNAP; Roper Scientific), to obtain the distribution of the F-actin inside the entire cell. Then, we calculated the maximum two-dimensional intensity projection in the cell-based reference system. Once we have the maximum two-dimensional projection for the actin distribution of each cell we calculated the average F-actin distribution for a large number of cells normalizing the intensity distribution with the maximum value for each cell, in order to avoid a larger weight in the average for cells in which the GFP intensity was higher. Therefore the actin intensity in our average measurements ranged from 0 to 1.

## 2.20 Determination of the actin foci localization

Wild-type cells were transformed with a vector encoding Lifeact (Abp140 (1-17)-GFP), a 17-amino acid peptide that binds F-actin fused to GFP [99]. Lifeact-expressing wild-type cells were used for fluorescence imaging of the actin at the ventral surface of the cells. We acquired z-stacks of green and red fluorescence images to visualize the actin localization of the cells and the beads' distribution respectively. The Lifeact fluorescence plane corresponding to maximum bead fluorescence was used to detect actin puncta or foci. It is straightforward to see that, if the bead distribution is uniform in z, the Lifeact signal recorded in this plane comes from a very narrow slice at the surface of the gel, thus allowing to visualize the actin foci on the ventral surface of the cells without interference from actin structures in the cell interior. These actin foci have been previously used as indicators of the areas where *Dictyostelium* cells adhere to the substrate [100].

## 2.21 Construction of cells with fluorescently labeled nucleus: H2B-GFP expressing cells

The sequence of H2Bv2 [101], a histone H2B domain-containing protein, was amplified from gDNA using the forward primer AAAAAGATCTAAAAAATGGTATTCGTTAAAGGTCAAAAG and the reverse primer TTTTTACTAGTGTTTTTGCTTTCAGTTGGATTG. The H2Bv2 domain was fused to GFP, by cloning into the extrachromosomal vector pDM323 digested with BglII and SpeI. The H2Bv2 domain was sequenced to ensure mutation-free DNA. Wild-type cells were transfected with this plasmid to generate H2B-GFP expressing cells for fluorescence imaging.

Chapter 2 has been in part published in *Applied Mechanics Reviews*, "Cytoskeletal mechanics regulating amoeboid cell locomotion" by B. Álvarez-González, E. Bastounis, R. Meili,

R. A. Firtel, J. C. del Álamo and J. C. Lasheras (2014), 66 (5), 050804. It has also been published in part in *Biophysical Journal*, by B. Álvarez-González, R. Meili, E. Bastounis, R. A. Firtel, J. C. Lasheras and J. C. del Álamo (2015), 108 (4), 821-832. The thesis author is the primary investigator in these publications.

# Chapter 3

# Cortical tension and axial contractility balance drives amoeboid migration

## 3.1 Introduction

To move on surfaces, amoeboid cells implement a motility cycle [102] [31] [103], enabled by the coordination of adhesion turnover, F-actin polymerization and cross-linking, and motor protein contractility [8]. Unlike slower moving cells that form stable integrin-mediated focal adhesions, amoeboid cells such as neutrophils and *Dictyostelium* cells rely on transient, diffuse adhesions [102]. The motor protein myosin II (MyoII) binds actin filaments to form a network that can generate the traction forces and is required for efficient cell motility [104]. F-actin cross-linkers such as filamin reinforce F-actin filaments at the leading edge, stabilizing newly formed pseudopodia by enabling a space-filling network that can communicate traction forces between the front and the back of the cell [48].

By definition, traction forces are the forces that a body applies to its tangential surface in order to propel itself. However, there is a puzzling lack of correlation between the migration speed of amoeboid cells and the strength of the traction forces, and this strength is much larger than needed to overcome friction from the overlying fluid [90]. The molecular and structural origins

of the traction forces are also unclear, as migrating cells lacking MyoII or F-actin cross-linkers are still able to exert significant traction forces [40] [24] [30]. Our biomechanical understanding of cell movement is complicated further because migrating cells exert significant normal forces (perpendicular to the substrate) in addition to the tangential ones [41] [105] [42] [106]. The mechanism whereby the cells are able to generate these strong normal forces is not known nor is the role of these normal forces in regulating the efficiency of motility.

The three-dimensional organization of cytoskeletal filaments [107] [108] should account, in part, for the normal forces exerted by the cells, since filaments pulling on the substrate at an elevation angle create both a normal and a tangential projection. However, the cell's cortex, which is composed of a shell of dense cross-linked actin filaments and myosin motors attached to the membrane and to the remainder of the cytoskeleton [109], may be a greater contributor to the generation of these normal forces and has been shown to regulate cell shape changes, cell polarization, and bleb formation during cell movement [54] [110] [59] [55].

By means of a recently developed 3D Force Microscopy technique [43], this study uncovered distinct molecular origins for the tangential and normal forces in migrating amoeboid cells. We analyzed wild-type chemotaxing *Dictyostelium* cells, as well as mutant strains with actin cross-linking and cortical integrity defects, and demonstrated that once the cells initiate their migration and polarize, they generate axial traction forces by MyoII contractility, which requires an internal cross-linked F-actin network. Simultaneously, cortical cross-linking and contractility (cortical tension) provides an additional mechanism for force generation and cytoplasmic pressurization that does not require MyoII. Our findings are consistent with a model in which the two force-generating cellular domains are mechanically connected by myosin I cross-linking that enables the communication of forces between the domains.

We found that the balance between axial MyoII contractility and cortical tension is important to produce the cell shape changes needed for locomotion, as cell migration speed correlates with the ratio of the magnitudes of the tangential traction forces to the normal ones. These results reveal a novel role for the three-dimensional cellular forces in establishing the efficiency of amoeboid cell movement and provide the first mechanistic explanation for the high

values of cell-substrate forces measured in migrating amoeboid cells.

## 3.2 Adhesion foci are needed to pull upward and inward but not to push downward

We measured the 3D forces exerted by *Dictyostelium* cells when migrating up a chemoattractant gradient over flat elastic substrates through the methodology explained in chapter 2 section 2.10, using the three-dimensional force microscopy method presented in del Álamo et al. [43]. Figure 3.1A shows the magnitude and spatial distribution of the tangential traction stresses exerted by a migrating wild-type cell in the plane of the substrate. The magnitude of these tangential forces is calculated as follows:

$$\tau_t = \sqrt{\tau_{zx}^2 + \tau_{zy}^2}, \tag{3.1}$$

with $\tau_{zx}$ being the axial stresses in the direction of the major axis of the cell, and $\tau_{zy}$ being the lateral stresses in the direction of the minor axis of the cell.

Figure 3.1B shows the magnitude and direction of the normal stresses, $\tau_{zz}$, exerted in the direction perpendicular to the substrate simultaneously to the tangential stresses shown in Figure 3.1A. We find that cells exert stresses on the substrate in two diffuse regions located at their front and rear halves. In these regions, the cells apply inward contractile tangential stresses (Figure 3.1A) as well as normal stresses pulling the substrate upward (red regions in Figure 3.1B). Concurrently, the cells also exert downward normal stresses (compressing the substrate) on a central area located between the frontal and rear regions where the cells pull up (Figure 3.1B). These patterns are consistently observed in all 3D cell-substrate forces measured over time in wild-type cells (Figure 3.2A and 3.3A). Figures 3.2A and 3.3A indicate that the locations where the cell applies tangential traction stresses directly coincide with the locations where the cell exerts upward pulling normal stresses.

The coordination of actin polymerization and motor protein contractility drives the gener-

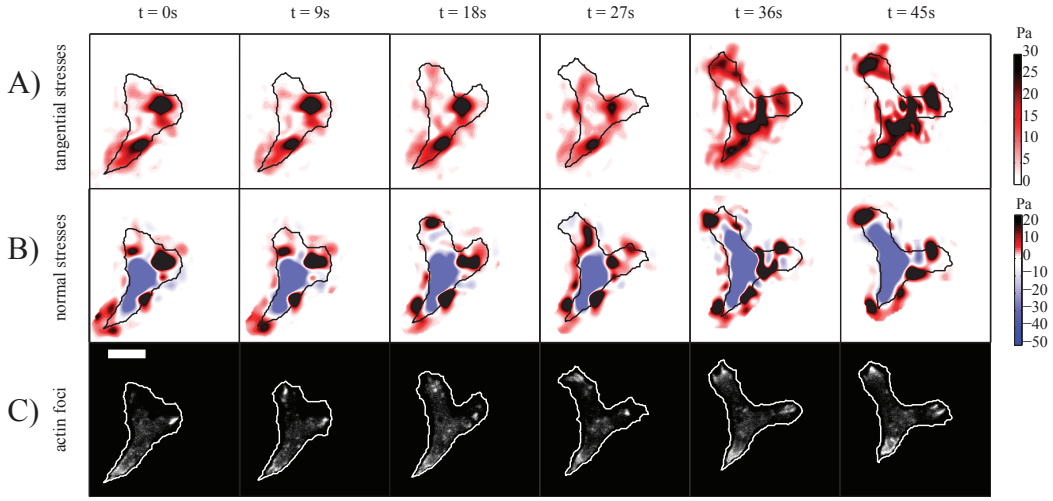


**Figure 3.1**: Tangential and normal stresses exerted by a wild-type cell on the substrate and actin foci localization at the cell's ventral surface in contact with the substrate, plotted every 9 seconds. A) Instantaneous tangential stresses. The colorbar on the right represents the magnitude of the tangential stresses. The contour of the cell is plotted in black. The cell moves from bottom to top. B) Instantaneous normal stresses. The colorbar on the right indicates normal stress magnitude in the upward (pulling, red) or downward (compressive, blue) direction. C) Localization of the actin structures at the ventral side of the cell at the same instants of time shown in panels A-B. The scale bar represents 10 $\mu$m.

ation of the traction stresses that regulates the cell motility [111] [8] [112]. These traction forces are transmitted to the substrate at the adhesion sites. The nature of the adhesions in *Dictyostelium* cells is still not clearly understood [113] [31], and the molecular receptors controlling adhesion have not been fully identified [32]. However, actin-rich structures (known as actin foci) have been previously reported to be localized at the ventral surface of the cell in the adhesion regions of migrating *Dictyostelium* cells [100] [46].

To clarify the interplay between adhesions, pulling forces, and pushing forces in migrating amoeboid cells, we measured three-dimensional cell-substrate forces and the localization of actin foci in wild-type cells simultaneously by imaging the F-actin fluorescent reporter Lifeact at the substrate's surface (Figure 3.1C). Our results indicate that the locations where the cell pulls upward and inward on the substrate, identified by the red spots in Figure 3.1A-B, coincide with the location of the actin foci (white spots in Figure 3.1C). No actin foci were found in regions where the cells are pushing down on the substrate (blue regions in Figure 3.1B). This suggests

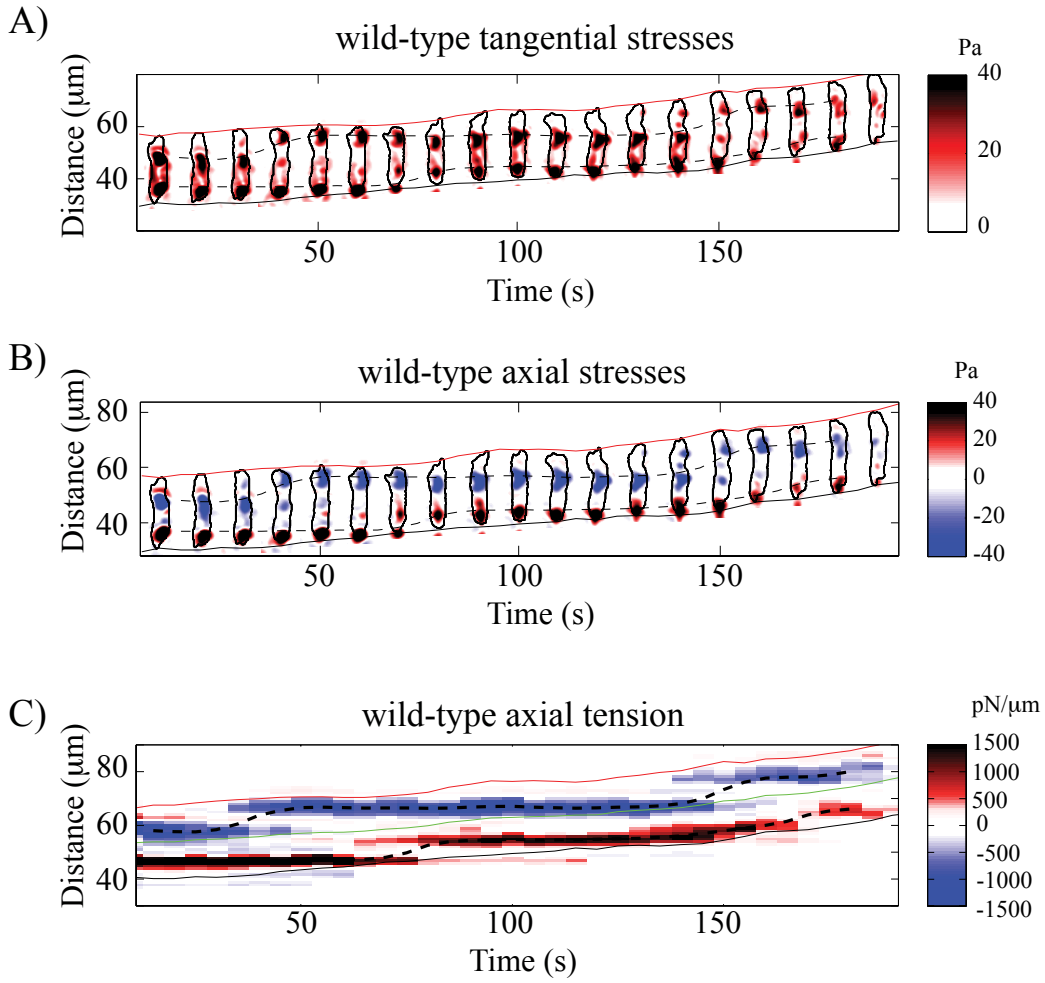


**Figure 3.2**: Kymographic representation of the tangential and axial stresses and axial tension applied by a representative wild-type cell. A) Spatiotemporal representation of the instantaneous magnitude of the tangential stresses as a function of the position along the cell trajectory and time for a representative wild-type cell. The cell contour is represented in black. The colormap on the right indicates the magnitude of the tangential stresses. The red and black lines indicate the instantaneous front and back edges of the cell respectively. Dotted-black lines denote the location of the maximum front and back absolute value of the axial traction tension, $T_x(x,t)$ (eq. 2.29) B) Spatiotemporal representation of the instantaneous magnitude of the axial stresses as a function of the position along the cell trajectory and time for the same wild-type cell as in panel A. C) Spatiotemporal representation of the axial tension, $T_x(x,t)$, as a function of the position along the cell trajectory and time for the same wild-type cell as in panels A and B. The green line indicates the location of the cell's centroid.

that cells need adhesion to pull over the substrate, but can compress it without. The cells pull upward on locations where they are *"mechanically actively"* adhering to the substrate, while they

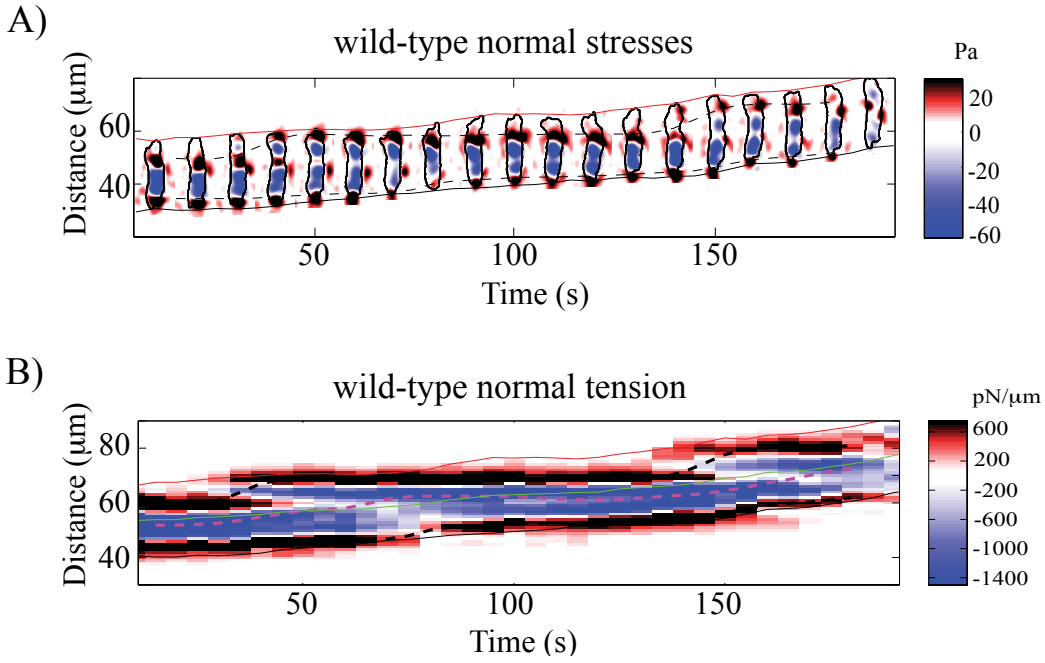


**Figure 3.3**: Kymographic representation of the normal stresses and tension applied by a representative wild-type cell. A) Spatiotemporal representation of the instantaneous magnitude of the normal stresses as a function of the position along the cell trajectory and time for a representative wild-type cell. The cell contour is represented in black. The colormap on the right indicates the magnitude and direction of the normal stresses. The red and black lines indicate the instantaneous front and back edges of the cell respectively. Dotted-black lines denote the location of the maximum normal tension $T_z(x,t)$ (eq. 2.30) at the frontal and rear halves of the cell. B) Spatiotemporal representation of the instantaneous magnitude of the normal tension, $T_z(x,t)$, as a function of the position along the cell trajectory and time for the same wild-type cell as in panel A. The green line indicates the location of the cell's centroid.

do not create *"active adhesions"* on the regions where they are pushing down on the substrate.

Figure 3.2A shows the tangential stresses exerted by a representative wild-type cell in a kymographic manner (chapter 2 section 2.16). Wild-type cells exert higher axial stresses than lateral ones, and Figure 3.2B shows the axial component of the tangential stresses exerted by this cell. Wild-type cells contract axially continuously and most of the time they adhere in two regions in the frontal and real halves. The axial tensions applied by this cell are presented in Figure 3.2C, the blue patches indicate front-to-back direction and the red ones indicate back-to-front direction.

The blue and red patches are located always in a horizontal position with respect to the kymograph axes (Figure 3.2C). This indicates that the adhesion sites where the cell applies the forces are stationary. This can also be seen through the instantaneous forces shown in Figure 3.2B.

The adhesion sites remain stationary while the cell protrudes a new pseudopod. During the protrusion process, the traction adhesions in the front remain stationary and they become a traction adhesion in the back when a new adhesion is formed in the front, in agreement with [30]. The adhesion in the back stays stationary too, until it is released and the adhesion in the front has become the new back adhesion.

The dotted black lines in Figure 3.2, indicate the locations of the maximum and minimum axial tension applied in the frontal and rear part of the cell, calculated using eq. 2.29. These dotted black lines are parallel to the horizontal axis of the kymograph, which indicates that the location where the maximum and minimum axial tension is applied remains stationary over time. The locations in which the lines are not horizontal, indicate a jump in the position of the maximum and minimum axial tension. This implies in the case of the frontal part of the cell, that the front adhesion becomes the new back adhesion and that a new adhesion is generated at the front. In the case of the rear part, it indicates that the back adhesion is released and a former front adhesion is now the new back adhesion.

Figure 3.3A shows that the locations in which the normal pulling forces are applied coincide with the locations in which the tangential forces are applied, and they also remain stationary over time. The cell translocates its body, but the adhesions remain stationary over time. Figure 3.3B shows the normal tension applied by this cell, calculated through eq. 2.30. The dotted black lines indicate the locations where the maximum normal tension is applied in the front and rear parts of the cell. The spatiotemporal evolution of the maximum normal tension applied at the front and rear parts coincides with the spatiotemporal evolution of the maximum and minimum axial traction tension applied at the front and rear parts, respectively, as is shown in Figure 3.2C and Figure 3.3B.

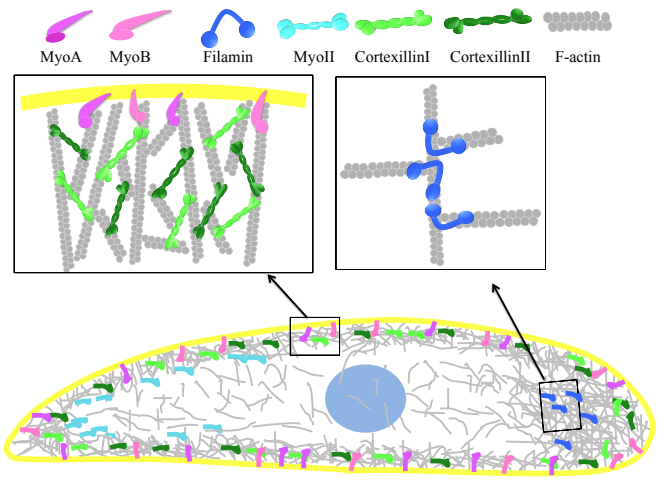


**Figure 3.4**: Sketch of the locations of the proteins that we examined inside the cell, and the interaction with the F-actin filaments.

## 3.3 Cortical tension is an important contributor to cell-substrate forces in cells with defects in the leading edge and posterior F-actin cross-linking

The motor protein myosin II binds actin filaments to form a network that can generate the traction forces and is required for efficient cell motility [104]. F-actin cross-linkers such as filamin stabilize F-actin filaments at the leading edge, providing newly formed pseudopodia with structural integrity by enabling a space-filling network that can transmit traction forces [48] (Figure 3.4). Cells with F-actin cross-linking defects generate lower traction forces that are distributed more laterally and move slower than wild-type cells [63][64]. Nonetheless, these cells still exert appreciable traction forces on their substrate and are able to migrate using mechanisms that are not fully understood yet [40] [24] [30].

To understand the genesis of these forces, we measured the 3D cell-substrate forces in MyoII null cells (*mhcA*$^-$) and filamin null cells (*abp120*$^-$), and those of their wild-type background strains (Ax3 and Ax2). To obtain the average tangential and normal forces exerted by each strain, we used a cell-based reference system with its origin at the centroid of the cell and its horizontal

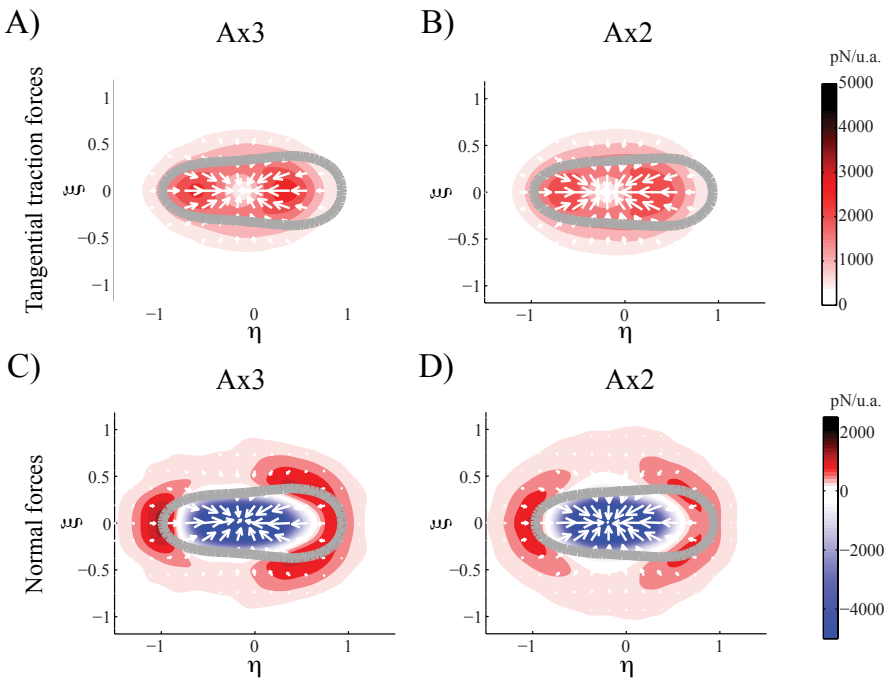


**Figure 3.5**: Average tangential and normal cell-generated force maps for wild-type *Dictyostelium* cells. A) Average tangential traction forces per unit area (in pN, colorbar on the right) exerted by Ax3 cells, (N=13 cells). The white arrows indicate their direction. The average cell contour is represented in gray. B) Average tangential traction forces per unit area (in pN, colorbar on the right) exerted by Ax2 cells, (N=13 cells). The white arrows indicate their direction. The average cell contour is represented in gray. C) Average normal forces per unit area (in pN, colorbar on the right) exerted by Ax3 cells, (N=13 cells). The red color indicates positive normal forces (the cells pull upward) and the blue color indicates negative normal forces (the cells push downward). D) Average normal forces per unit area (in pN, colorbar on the right) exerted by Ax2 cells, (N=13 cells). The red color indicates positive normal forces (the cells pull upward) and the blue color indicates negative normal forces (the cells push downward).

axis aligned along the front-back axis of the cell, and we normalized spatial coordinates with the cell length [90] [24], as explained in chapter 2 section 2.14.

In the wild-type strains Ax3 and Ax2, the tangential forces were concentrated on two areas located at the front and rear ends of the cell (Figures 3.2A, 3.5A-B). The direction of these tangential forces (white arrows in Figure 3.5A-B) indicates that the cells contracted axially. In the normal direction, wild-type cells pulled upward at their front and rear, while they pushed downward on their central region (Figures 3.3A, 3.5C-D). The pulling normal and tangential forces were of similar strength (Figure 3.5).

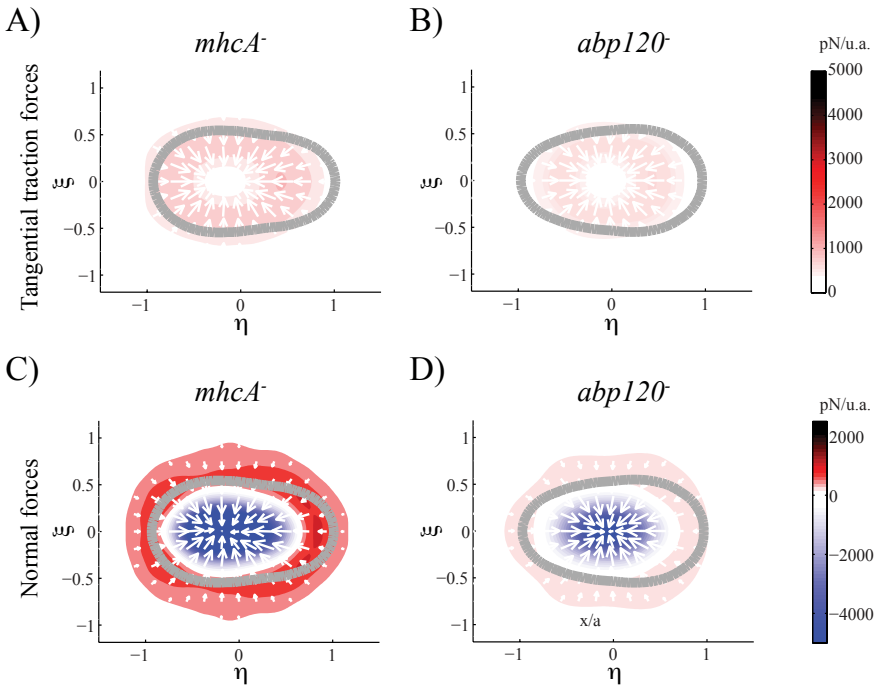


**Figure 3.6**: Average tangential and normal cell-generated force maps for cells with defects in the leading edge and posterior cross-linking. A) Average tangential traction forces per unit area (in pN, colorbar on the right) exerted by *mhcA*$^{-}$ cells, (N=13 cells). The white arrows indicate their direction. The average cell contour is represented in gray. B) Average tangential traction forces per unit area (in pN, colorbar on the right) exerted by *abp120*$^{-}$ cells, (N=12 cells). The white arrows indicate their direction. The average cell contour is represented in gray. C) Average normal forces per unit area (in pN, colorbar on the right) exerted by *mhcA*$^{-}$ cells, (N=13 cells). The red color indicates positive normal forces (the cells pull upward) and the blue color indicates negative normal forces (the cells push downward). D) Average normal forces per unit area (in pN, colorbar on the right) exerted by *abp120*$^{-}$ cells, (N=12 cells). The red color indicates positive normal forces (the cells pull upward) and the blue color indicates negative normal forces (the cells push downward).

In contrast to wild-type cells, *mhcA*$^{-}$ and *abp120*$^{-}$ cells pulled on the substrate in the tangential and normal directions all along their peripheral cortex (Figure 3.6). This is consistently shown for all the time points in all the experiments that we performed involving cells with leading edge and posterior cross-linking defects (Figure 3.7A, 3.8A). The 3D force patterns generated by cells lacking acto-myosin contraction were similar to those observed for liquid drops when placed onto soft substrates, which exert upward forces due to surface tension around their edge, and downward forces due to fluid pressure under their center [114]. These results are consistent with our previous 2D observations that axial cell-substrate forces mediated by acto-myosin contraction

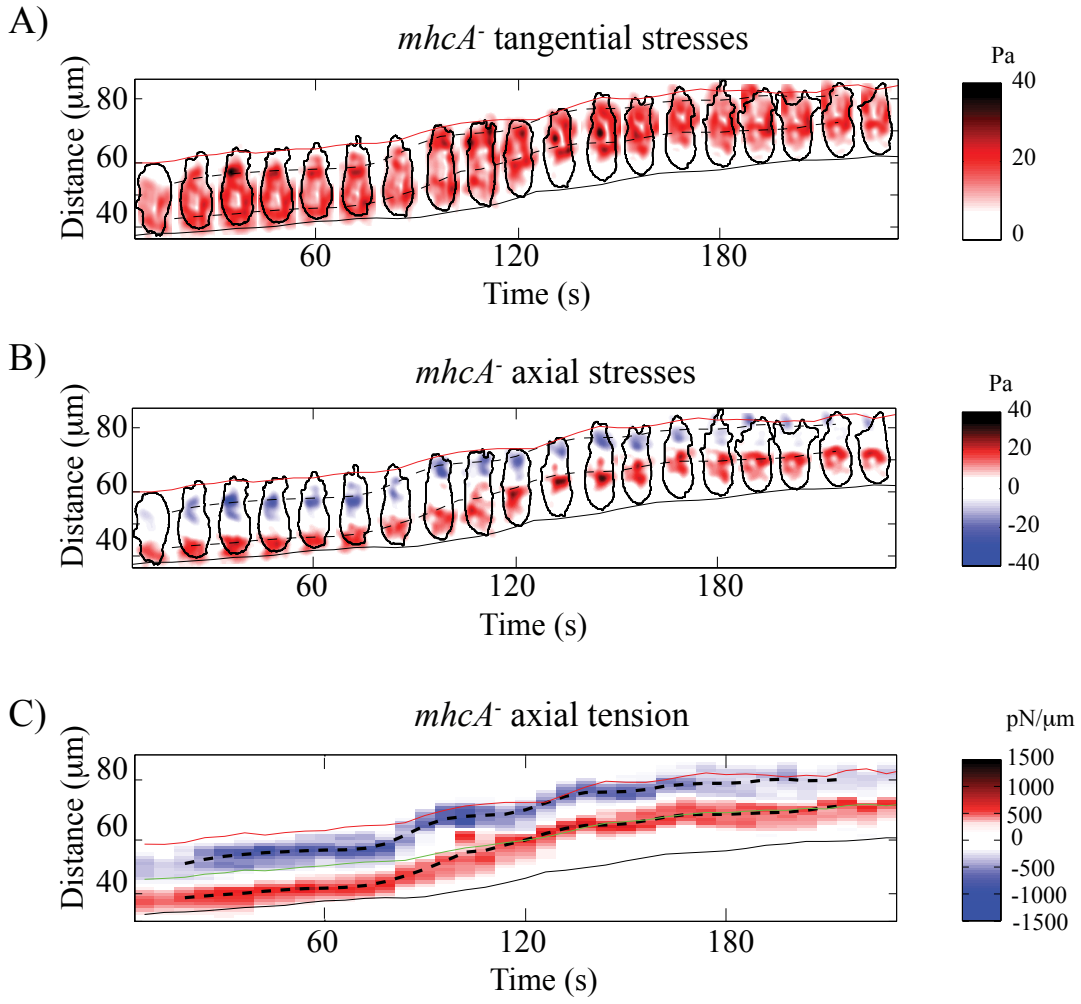


**Figure 3.7**: Kymographic representation of the tangential stresses and axial stresses and tension applied by a representative *mhcA*$^-$ cell. A) Spatiotemporal representation of the instantaneous magnitude of the tangential stresses as a function of the position along the cell trajectory and time for a representative *mhcA*$^-$ cell. The cell contour is represented in black. The colormap on the right indicates the magnitude of the tangential stresses. The red and black lines indicate the instantaneous front and back edges of the cell, respectively. Dotted-black lines denote the location of the maximum front and back absolute value of the axial traction tension, $T_x(x,t)$ (eq. 2.29). B) Spatiotemporal representation of the instantaneous magnitude of the axial stresses as a function of the position along the cell trajectory and time for the same *mhcA*$^-$ cell as in panel A. C) Spatiotemporal representation of the axial tension, $T_x(x,t)$, as a function of the position along the cell trajectory and time for the same *mhcA*$^-$ cell as in panels A and B. The green line indicates the cell's centroid.

are lost in *mhcA*$^-$ and *abp120*$^-$ cells [90] [24] [30], and suggest that cortical and membrane tension generates the three-dimensional cell-substrate forces observed in these cell strains.

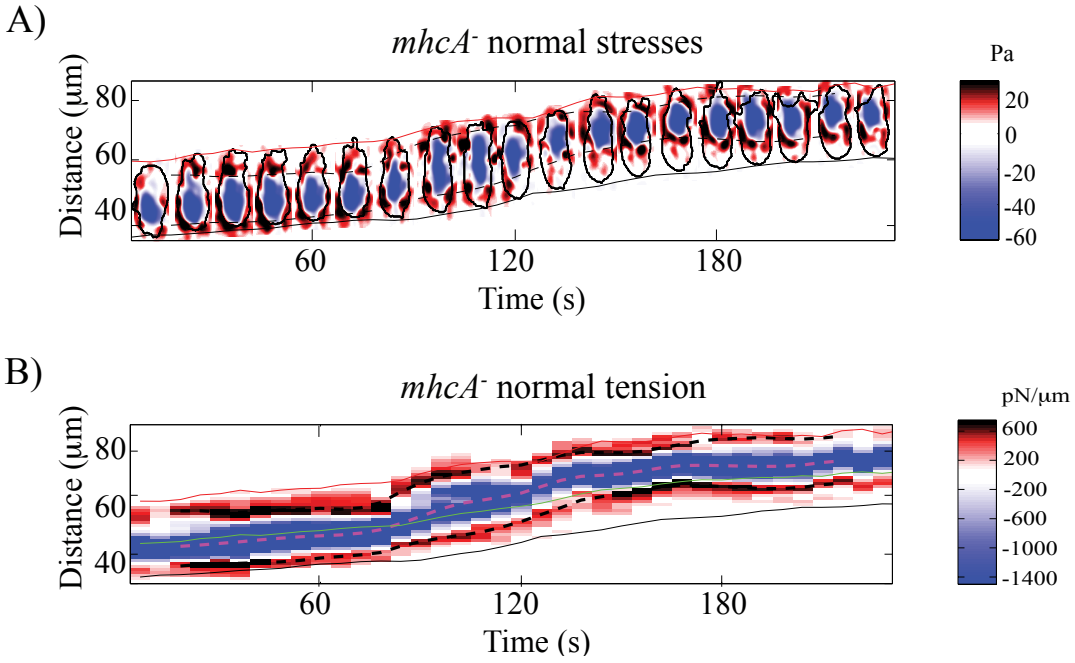


**Figure 3.8**: Kymographic representation of the normal stresses and tension applied by a representative *mhcA*$^-$ cell. A) Spatiotemporal representation of the instantaneous magnitude of the normal stresses as a function of the position along the cell trajectory and time for a representative *mhcA*$^-$ cell. The cell contour is represented in black. The colormap on the right indicates the magnitude and direction of the normal stresses. The red and black lines indicate the instantaneous front and back edges of the cell respectively. Dotted-black lines denote the location of the maximum normal tension, $T_z(x,t)$, (eq. 2.30) at the frontal and rear halves of the cell. B) Spatiotemporal representation of the instantaneous magnitude of the normal tension, $T_z(x,t)$, as a function of the position along the cell trajectory and time for the same *mhcA*$^-$ cell as panel in A.

Figure 3.7A shows the instantaneous tangential stresses exerted by *mhcA*$^-$ cells, we observed that the stresses lack the front-to-back organization exhibited in wild-type cells. As can be observed in Figure 3.7A, *mhcA*$^-$ cells have multiple traction adhesions located around the cell periphery. The shape of these cells is also less elongated, and they form multiple pseudopodia all around their perimeter. Moroever, the location of these peripheral traction adhesions usually coincides with the location of the lateral pseudopodia. In this case, the axial forces are lower than in wild-type cells (Figure 3.7B), and the lateral forces are as high as the axial ones. Therefore, the axial tension kymographs for *mhcA*$^-$ cells do not provide as much information as in the case of wild-type cells. Similarly to wild-type cells, we observed that the traction adhesions in the front are stationary, as well (Figure 3.7B-C). However, in the case of the *mhcA*$^-$ cells, the the tractions

adhesions in the rear part, are not always stationary. This can be due to the important role of the protein myosin II in the retraction of the rear part of the cell [104] [40].

The normal pulling forces exerted by *mhcA*$^-$ cells, are always organized around their peripheral cortex (Figure 3.8A). Figure 3.7A and Figure 3.8A indicate that the location of the pulling normal forces coincides with the location of the tangential traction forces. The pulling normal forces in the front part of the cell remain mostly stationary, contrary to the location of the pulling normal forces in the back, which does not remain stationary over time (Figure 3.8C).

## 3.4 Axial traction forces drive the movement of cells with cortical cross-linking defects

To examine the role of the cell cortex in the generation of cell-substrate forces, we analyzed three mutant strains with cortical cross-linking defects: cortexillin I null cells (*ctxA*$^-$), cortexillin II null cells (*ctxB*$^-$) and cortexillin I and cortexillin II double null cells (*ctxA*$^-$*/B*$^-$). Cortexillin I and cortexillin II are members of the α-actinin/spectrin family that are located in the cortex and involved in the regulation of cell morphology [65] and cell division [66][115][116]. Cortexillin I and cortexillin II are F-actin-binding proteins that form complexes with the IQGAP proteins (IQGAP1 and IQGAP2) and bind the Rac family of small GTPases [117]. These proteins are enriched in the cortex of migrating cells at the front, back, and lateral sides of the cell [118] [65], but are not found in the ventral actin foci [65] (Figure 3.4).

Figure 3.9A-C shows that cortexillin null cells contracted axially similarly to wild-type cells, exerting tangential forces on the substrate that were concentrated at the front and back ends of the cell. The tangential traction forces exerted by cortexillin null cells are even higher than those exerted by wild-type cells and they are distributed even less laterally than in wild-type cells (Figure 3.5B, 3.9A-C). However, compared to wild-type cells, the normal forces were weaker with respect to the tangential ones and were distributed less laterally (Figure 3.9D-F). These results suggest that in cells with cortical cross-linking defects, the tangential traction forces mediated by MyoII contractility are increased and drive cell motion, whereas the cortical tension is weaker and

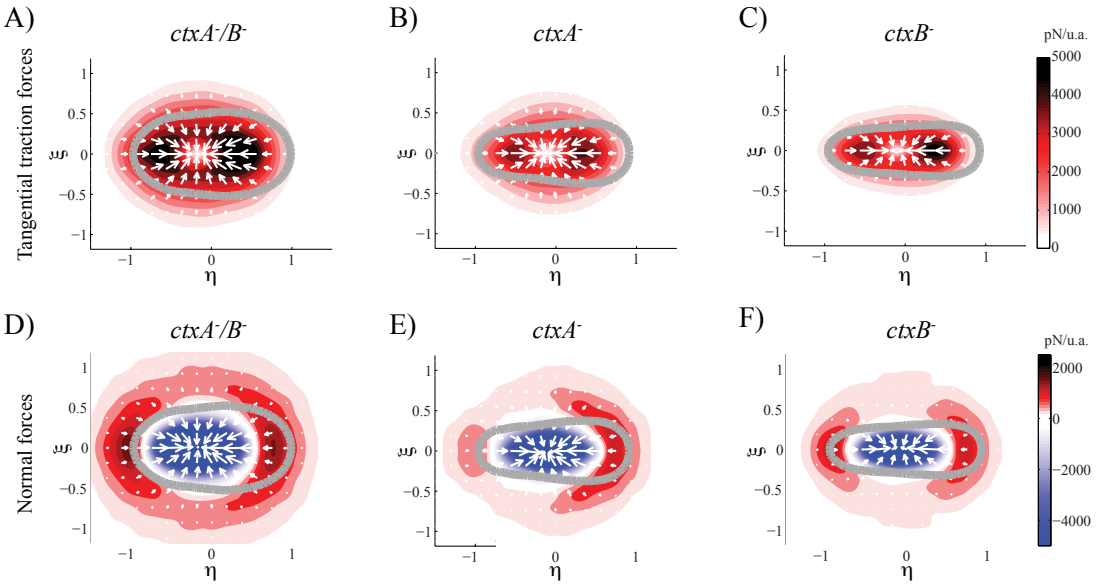


**Figure 3.9**: Average tangential and normal cell-generated force maps for cells with defects in the cortical cross-linking. A) Average tangential traction forces per unit area (in pN, colorbar on the right) exerted by *ctxA⁻/B⁻* cells, (N=11 cells). The white arrows indicate their direction. The average cell contour is represented in gray. B) Average tangential traction forces per unit area (in pN, colorbar on the right) exerted by *ctxA⁻* cells, (N=12 cells). C) Average tangential traction forces per unit area (in pN, colorbar on the right) exerted by *ctxB⁻* cells, (N=13 cells). D) Average normal forces per unit area (in pN, colorbar on the right) exerted by *ctxA⁻/B⁻* cells, (N=11 cells). The red color indicates positive normal forces (the cells pull upward) and the blue color indicates negative normal forces (the cells push downward). E) Average normal forces per unit area (in pN, colorbar on the right) exerted by *ctxA⁻* cells, (N=12 cells). F) Average normal forces per unit area (in pN, colorbar on the right) exerted by *ctxB⁻* cells, (N=13 cells).

is not essential for their movement. Thus, the *ctxA⁻*, *ctxB⁻* and *ctxA⁻/B⁻* cells exhibit an opposite phenotype regarding the generation of tangential and normal forces than the cells with defective leading edge and posterior F-actin cross-linking, *abp120⁻* and *mhcA⁻* cells.

Our finding that both the tangential and normal forces are higher in the *ctxA⁻/B⁻* cells than in wild-type cells could be unexpected. However, we note that in these cells F-actin levels are increased [119] and F-actin is localized around much of the cortex of the cell [65], rather than predominantly in the front as in wild-type cells as shown in Figure 3.10A, C.

To assess the influence of the actin distribution organization in the generation of the traction forces we calculated the average distribution of F-actin as explained in chapter 2 section 2.19. Figure 3.11 shows the average two-dimensional projection of the F-actin distribution in

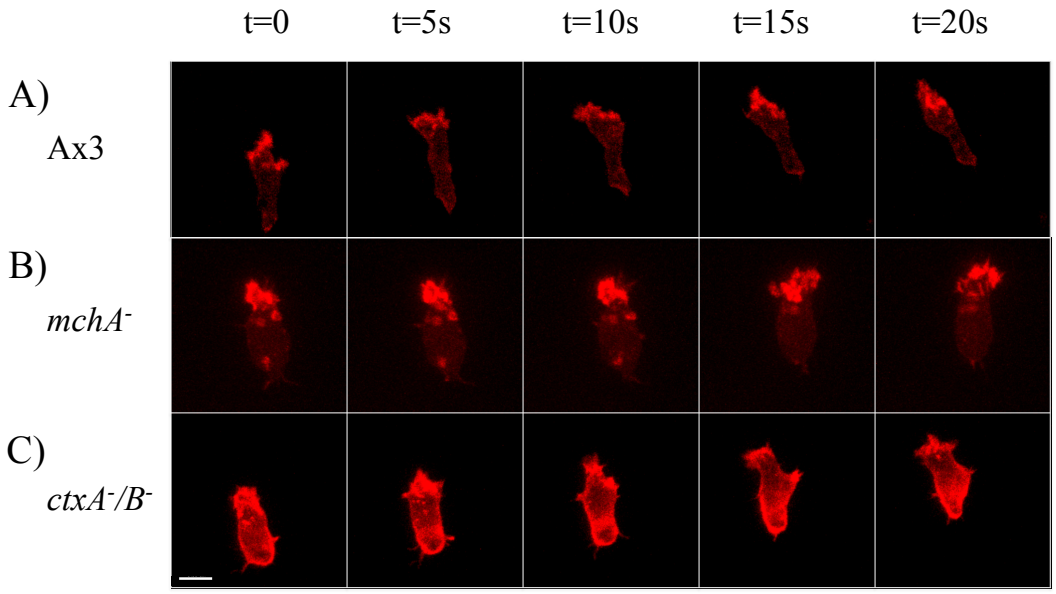


**Figure 3.10**: Projection of the three-dimensional instantaneous distribution of F-actin in wild-type, *mhcA*$^-$ and *ctxA*$^-$*/B*$^-$ cells, the images show the distribution every 5 seconds and the scale bar on the bottom left represents 10 $\mu$m. A) Projection of the instantaneous three-dimensional actin distribution of a chemotaxing representative wild-type cell. B) Projection of the instantaneous three-dimensional actin distribution of a chemotaxing representative *mhcA*$^-$ cell. C) Projection of the instantaneous three-dimensional actin distribution of a chemotaxing representative *ctxA*$^-$*/B*$^-$ cell. The two-dimensional projection of the three-dimensional actin distribution was generated by using IMARIS software (Bitplane).

wild-type, *mhcA*$^-$ and *ctxA*$^-$*/B*$^-$ cells. In *ctxA*$^-$*/B*$^-$ cells the F-actin is organized around the cortex however, in wild-type and *mhcA*$^-$ cells it is localized in the frontal region, (Figure 3.10A-C). Previous studies showed that cells with higher levels of F-actin than wild-type cells, exhibit also higher traction forces and cells with lower levels of F-actin than wild-type cells exert lower traction forces [103]. Therefore, the content of F-actin may be correlated to the level of force exerted by the cell [103]. We suggest that, while these higher cortical F-actin levels lead to increased forces, the resulting misorganization of the F-actin cytoskeleton impacts the cortical integrity compared to the cell's axial contractility.

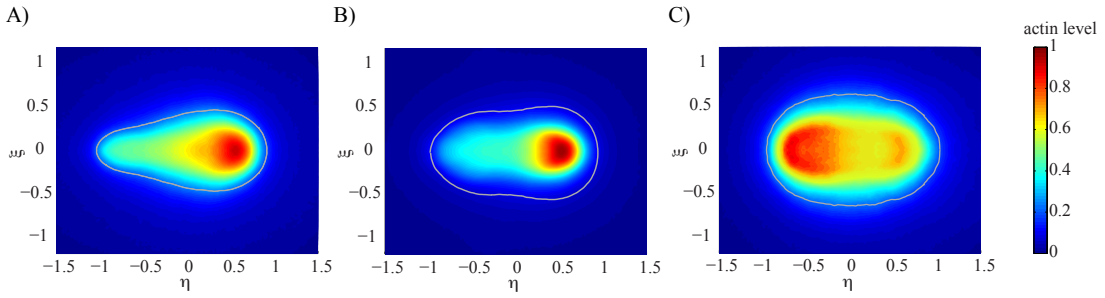


**Figure 3.11**: Average two-dimensional projection of the F-actin distribution in wild-type, *mhcA*$^-$ and *ctxA*$^-$*/B*$^-$ cells. A) Average two-dimensional projection of the F-actin distribution in wild-type cells, (N=14). B) Average two-dimensional projection of the F-actin distribution in *mhcA*$^-$ cells, (N=12). C) Average two-dimensional projection of the F-actin distribution in *ctxA*$^-$*/B*$^-$ cells, (N=12).

## 3.5 Myosin IA and myosin IB are required for intracellular force transmission between the cortex and the internal F-actin network

The results above indicate that chemotaxing amoebae can exert 3D forces on their substrate through two distinct cellular domains, one being the leading edge and posterior F-actin structure and the other being the cortical tension generated by the cellular membrane and cortex. To examine if these mechanical domains are interconnected or independent, we studied the 3D cell-substrate forces exerted by myosin IA null cells (*myoA*$^-$), myosin IB null cells (*myoB*$^-$), and myosin IA and myosin IB double null cells (*myoA*$^-$*/B*$^-$). Myosin IA (MyoA) and myosin IB (MyoB) are single-headed actin molecular motors with a high affinity membrane-binding C-terminal tail domain, which are localized at the membrane/cortex of the cells [120] (Figure 3.4). In these strains, the connections between the plasma membrane, the cortical actin, and the internal F-actin meshwork are impaired [67].

Our results indicate that *myoA*$^-$, *myoB*$^-$ and *myoA*$^-$*/B*$^-$ cells exert axial tangential forces that are concentrated on two regions at their front and back as observed for the wild-type and cortexillin null cells in which the cell-substrate force generation is dominated by acto-myosin contractility (Figure 3.12A-C). However, the normal pulling forces exerted by *myoB*$^-$ and *myoA*$^-$*/B*$^-$

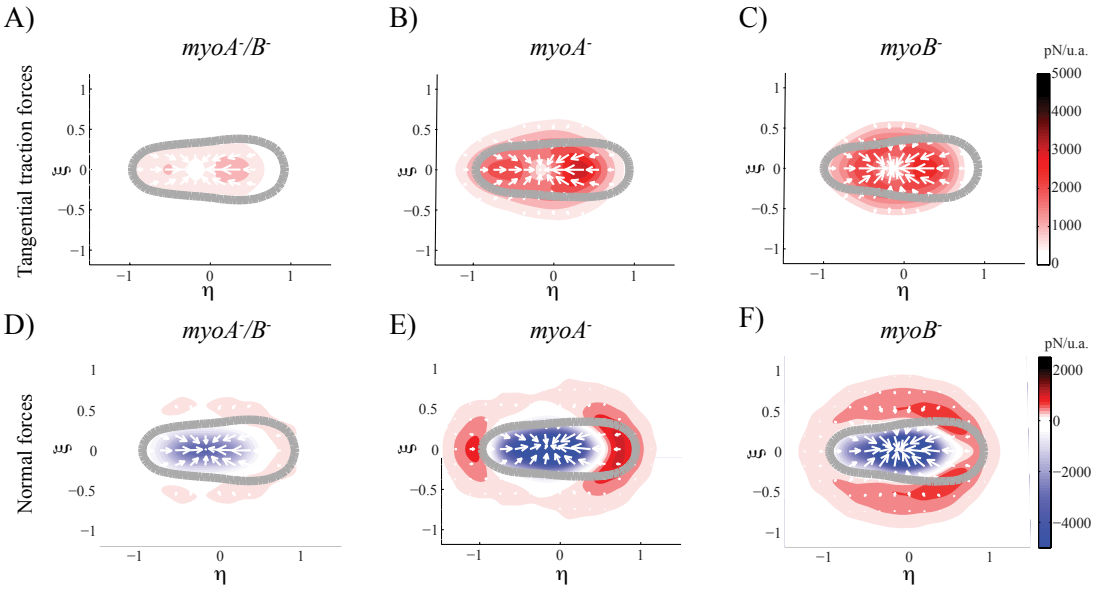


**Figure 3.12**: Average tangential and normal cell-generated force maps for cells with defective linking between the plasma membrane and the cortical and intracellular F-actin. A) Average tangential traction forces per unit area (in pN, colorbar on the right) exerted by *myoA⁻/B⁻* cells, (N=13 cells). The white arrows indicate their direction. The average cell contour is represented in gray. B) Average tangential traction forces per unit area (in pN, colorbar on the right) exerted by *myoA⁻* cells, (N=13 cells). C) Average tangential traction forces per unit area (in pN, colorbar on the right) exerted by *myoB⁻* cells, (N=14 cells). D) Average normal forces per unit area (in pN, colorbar on the right) exerted by *myoA⁻/B⁻* cells, (N=13 cells). The red color indicates positive normal forces (the cells pull upward) and the blue color indicates negative normal forces (the cells push downward). E) Average normal forces per unit area (in pN, colorbar on the right) exerted by *myoA⁻* cells, (N=13 cells). F) Average normal forces per unit area (in pN, colorbar on the right) exerted by *myoB⁻* cells, (N=14 cells).

cells were more evenly distributed along the cell periphery, similar to the *mhcA⁻* and *abp120⁻* cells in which cell-substrate force generation is dominated by cortical tension (Figure 3.12D, F). These results suggest that the acto-myosin contractile compartment of *myoB⁻ and myoA⁻/B⁻* cells is not fully coupled to their cortex. Loss of MyoA (Figure 3.12E) affected the cells in a different manner, causing a traction force phenotype more similar to that of *ctxB⁻* cells.

Figure 3.13A shows the temporal evolution of the instantaneous magnitude of the tangential traction forces exerted by a *myoA⁻/B⁻* cell. These forces are mostly organized in a polar manner, the axial forces are shown in Figure 3.13B. The magnitude of the tangential forces is much lower than in wild-type cells. The traction adhesions in the front and rear part of *myoA⁻/B⁻*

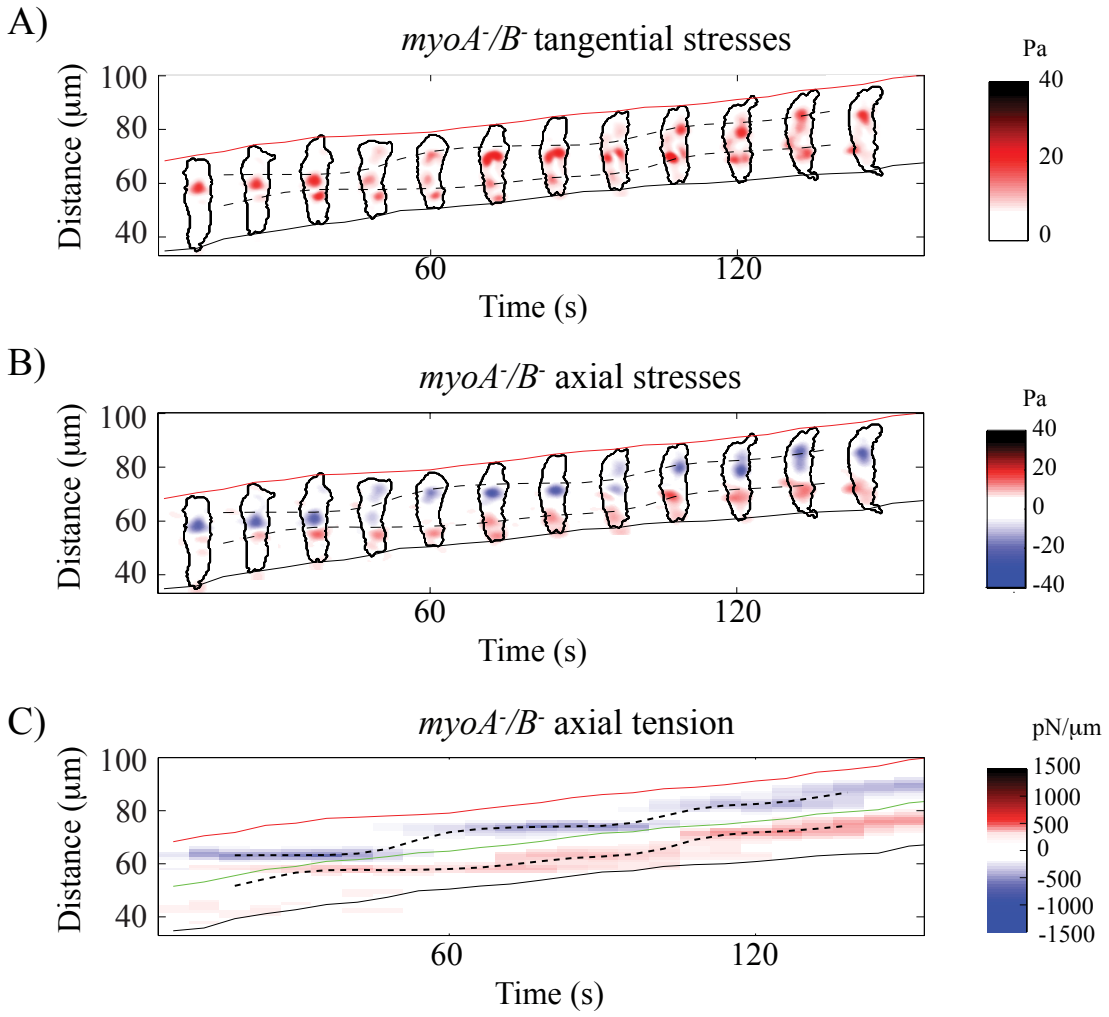


**Figure 3.13**: Kymographic representation of the tangential stresses and the axial stresses and tension applied by a representative *myoA⁻/B⁻* cell. A) Spatiotemporal representation of the instantaneous magnitude of the tangential stresses exerted by a representative *myoA⁻/B⁻* cell as a function of the position along the cell trajectory and time. The cell contour is represented in black. The colormap on the right indicates the magnitude of the tangential stresses. The red and black lines indicate the instantaneous front and back edges of the cell respectively. Dotted-black lines denote the location of the maximum front and back absolute value of the axial traction tension, $T_x(x,t)$ (eq. 2.29). B) Spatiotemporal representation of the instantaneous magnitude of the axial stresses as a function of the position along the cell trajectory and time for the same *myoA⁻/B⁻* cell as in panel A. C) Spatiotemporal representation of the axial tension, $T_x(x,t)$, as a function of the position along the cell trajectory and time for the same *myoA⁻/B⁻* cell as panels in A and B.

cells remain stationary, as in the case of wild-type cells. Figure 3.13C shows the axial tension kymograph for a representative *myoA⁻/B⁻* cell. The dotted-black lines show the spatiotemporal

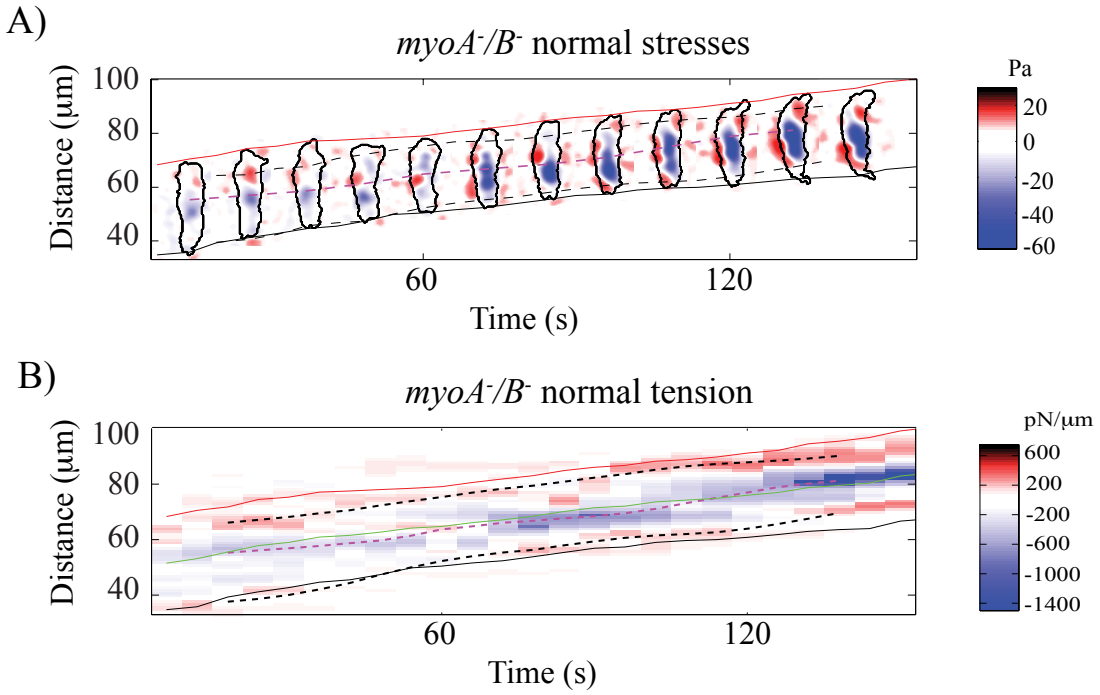


**Figure 3.14**: Kymographic representation of the normal stresses and tension applied by a representative *myoA⁻/B⁻* cell. A) Spatiotemporal representation of the instantaneous magnitude of the normal stresses as a function of the position along the cell trajectory and time for a representative *myoA⁻/B⁻* cell. The cell contour is represented in black. The colormap on the right indicates the magnitude and direction of the normal stresses. The red and black lines indicate the instantaneous front and back edges of the cell respectively. Dotted black lines denote the location of the maximum normal tension, $T_z(x,t)$, (eq. 2.30) at the frontal and rear halves of the cell. B) Spatiotemporal representation of the instantaneous magnitude of the normal tension, $T_z(x,t)$, as a function of the position along the cell trajectory and time for the same *myoA⁻/B⁻* cell as in panel A.

evolution of the maximum and minimum axial tension in the frontal and rear parts of the cell, respectively. These dotted-black lines are parallel to the horizontal axis of the kymograph, which indicates that the traction adhesions remains stationary over time, similarly to the case of wild-type cells. However, Figure 3.14A, represents the magnitude and direction of the normal forces exerted by this same cell. The pulling normal forces exerted by this cell are not organized in a polar manner, but they are more distributed around the peripheral cortex of the cell.

Additionally, the normal tension kymograph, which shows the spatiotemporal evolution of the maximum pulling normal tension in the frontal and rear parts of the cell, indicates that the location where the normal forces are applied is not stationary over time (Figure 3.14B). We

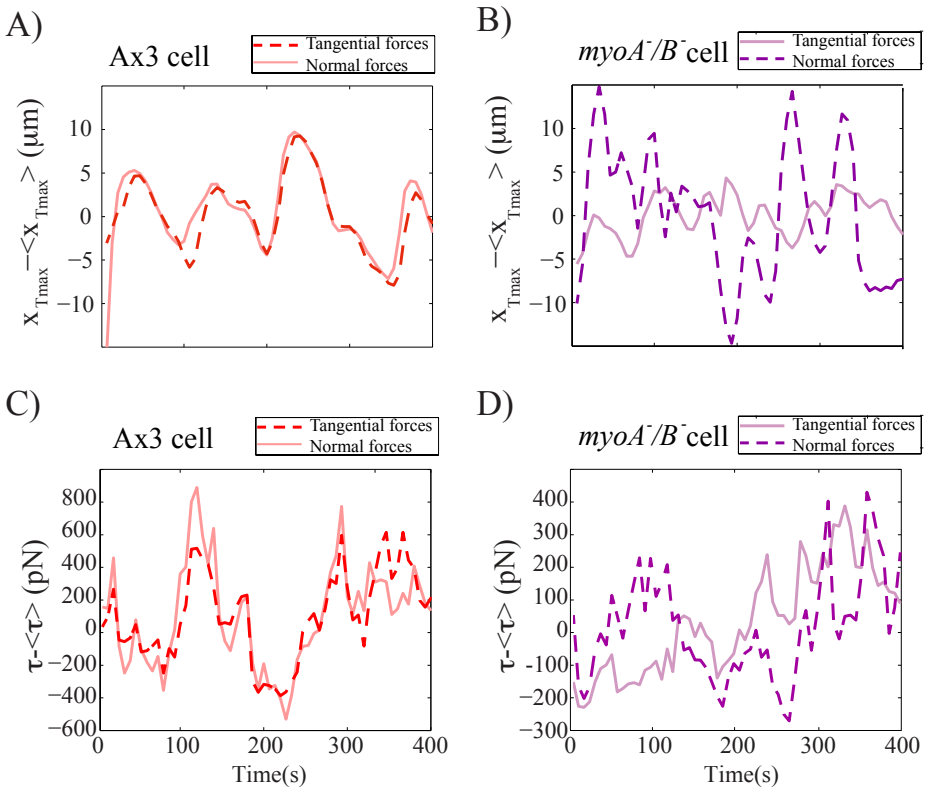


**Figure 3.15**: Time fluctuations of the locations and magnitude of the tangential and normal forces exerted by Ax3 and *myoA⁻/B⁻* cells. A) Time fluctuations of the locations of the maximum tangential and normal tensions in a representative Ax3 cell with respect to the cell center. B) Time fluctuations of the locations of the maximum tangential and normal tensions in a representative *myoA⁻/B⁻* cell with respect to the cell center. C) Time fluctuations of the magnitude of the tangential and normal forces exerted by the same Ax3 cell as in panel A. D) Time fluctuations of the magnitude of the tangential and normal forces exerted by the same *myoA⁻/B⁻* cell as in panel B.

observe, that the tangential and normal forces are not applied in the same locations in the case of *myoA⁻/B⁻* cells (Figure 3.13C, 3.14B), in contrast with the good correlation in the locations between the tangential and normal forces that we find for the other cell lines studied.

To further investigate the interconnection between the actomyosin-mediated axial contractility and cortical tension, we assessed the correlation in the magnitude and co-localization of the tangential and normal pulling forces for each strain, following the methodology explained in chapter 2, section 2.15. In wild-type cells, the tangential and normal pulling forces co-localized in space and their magnitudes followed the same temporal evolution (Figure 3.15A, C), leading

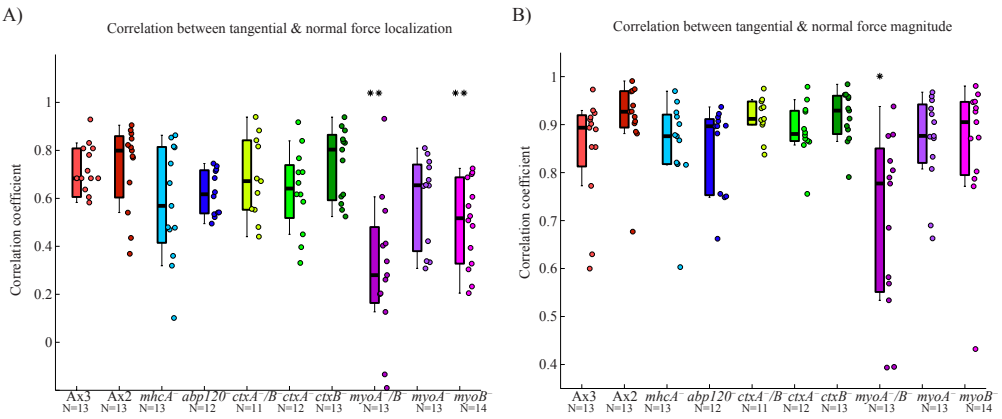


**Figure 3.16**: Correlation in the location and magnitude of the tangential and normal forces. A) Spearman correlation coefficient for the spatiotemporal evolution of the location of the tangential and normal tension in the cell-based coordinate system. B) Spearman correlation coefficient for the temporal evolution of the magnitudes of the tangential and normal forces. The cell lines and number of cells (N) are indicated beneath the boxplot. Asterisks denote statistically significant differences between each specific mutant strain and its corresponding wild-type distribution (Wilcoxon ranksum test, * $p < 0.05$, ** $p < 0.01$).

to high values of the correlation coefficients of co-localization and magnitude, as shown in Figure 3.16. Similar high correlation values were obtained for the *mhcA*$^-$, *abp120*$^-$, *ctxA*$^-$*/B*$^-$, *ctxA*$^-$ and *ctxB*$^-$ cells, suggesting that the cortical and the internal F-actin networks are two independent, yet interconnected generators of cellular force. However, in *myoA*$^-$*/B*$^-$ cells the tangential and pulling normal forces did not co-localize, and their magnitudes evolved differently in time (Figure 3.15B, D). Consequently, both correlation coefficients were significantly lower in *myoA*$^-$*/B*$^-$ than in wild-type cells (Figure 3.16). Loss of MyoB caused a decreased correlation in co-localization but not in magnitude, whereas loss of MyoA did not cause significant changes in either measure of correlation between the tangential and normal forces. Taken together, these results suggest that both MyoA and MyoB play distinct roles in the communication of forces between the internal F-actin network and the cortex. Loss of MyoA alone is not enough to significantly alter this communication, which is completely disrupted in cells lacking both MyoA and MyoB. Additionally, MyoB is involved in the spatial co-localization of the forces generated by acto-myosin contractility and cortical tension, while MyoA is not.

In addition to the high values of the correlation coefficient for the spatio-temporal evolu-

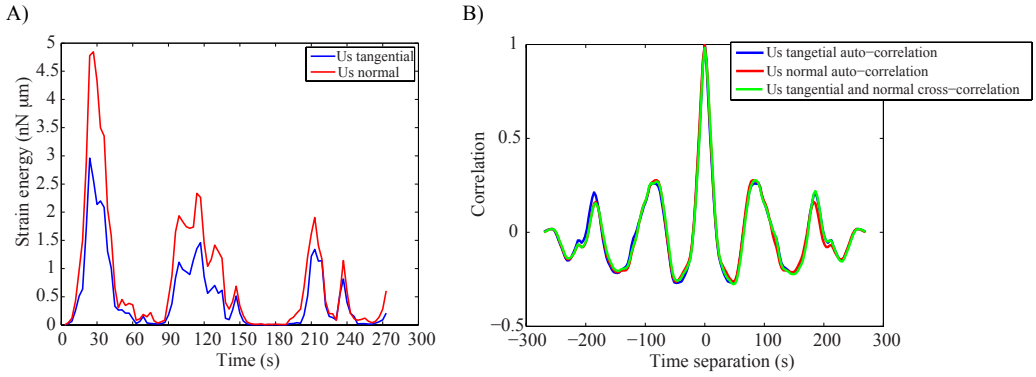


**Figure 3.17**: Strain energy temporal evolution and correlation functions. A) Temporal evolution of the strain energy generated by the tangential (blue) and normal (red) stresses. B) Auto-correlation functions of the strain energy generated by the tangential stresses (blue) and of the strain energy generated by the normal stresses (red) and cross-correlation function of the strain energy generated by the tangential stresses and by the normal stresses (green).

tion and magnitude of the tangential and normal stresses, we also find that these measurements are in phase for wild-type, *mhcA*$^-$, *abp120*$^-$, *ctxA*$^-$*/B*$^-$, *ctxA*$^-$, *ctxB*$^-$ and *myoA*$^-$ cells. Therefore, this indicates that the two mechanisms are connected and the fluctuations of these measurements determine the period of the motility cycle of the cell. Figure 3.17B shows the correlation functions of the strain energy generated by the tangential stresses and the normal stresses for a representative wild-type cell (Figure 3.17A), as explained in chapter 2 section 2.12. The oscillatory behavior of the strain energy defines as well the period of the motility cycle of chemotaxing cells, which is around 80 seconds for all the cell lines that we have examined except for *mhcA*$^-$ cells, which have a longer period [103] [24], as shown in Figure 3.18.

## 3.6 The tangential to normal forces ratio is higher in cells with cortical cross-linking defects and lower in cells with defects in the leading edge and posterior cross-linking

We observe that the cell lines with leading edge and posterior cross-linking defects exert lower tangential traction forces than wild-type cells (Figure 3.19A), but the normal forces have similar strength (Figure 3.19B). On the other hand, cortexillin null cells exert higher tangential

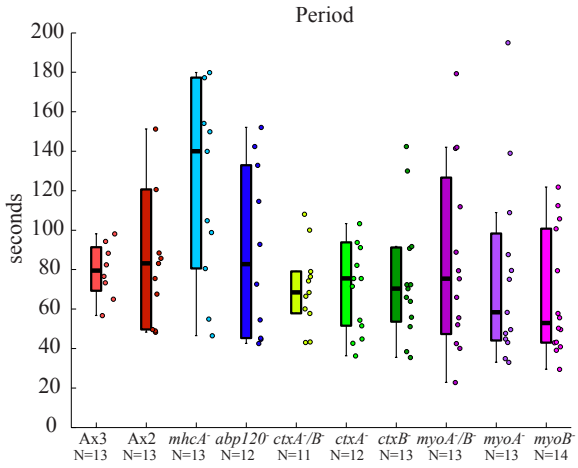


**Figure 3.18**: Period of the motility cycle calculated from the temporal evolution of the strain energy. The cell lines and number of cells (N) are indicated beneath the boxplot.

traction forces than wild-type cells.

Figure 3.19A shows the magnitude of the tangential forces exerted by the cell lines that we have examined. This magnitude is calculated as:

$$|\tau_t| = \int_0^L \int_0^W \sqrt{\tau_{zx}^2 + \tau_{zy}^2} dxdy \tag{3.2}$$

where $L$ represents the length of the cell and $W$ represents the width of the cell. Figure 3.19B shows the magnitude of the normal forces exerted by these same cell lines. The magnitude of the normal forces is calculated as:

$$|\tau_n| = \int_0^L \int_0^W |\tau_{zz}| dxdy \tag{3.3}$$

where $L$ represents the length of the cell and $W$ represents the width of the cell.

We observed that the ratio between the magnitudes of the tangential and normal cell-substrate forces varied considerably between wild-type cells, cells with defective internal cross-linking, and cells with cross-linking defects in the cortical region (Figure 3.19C). The ratio

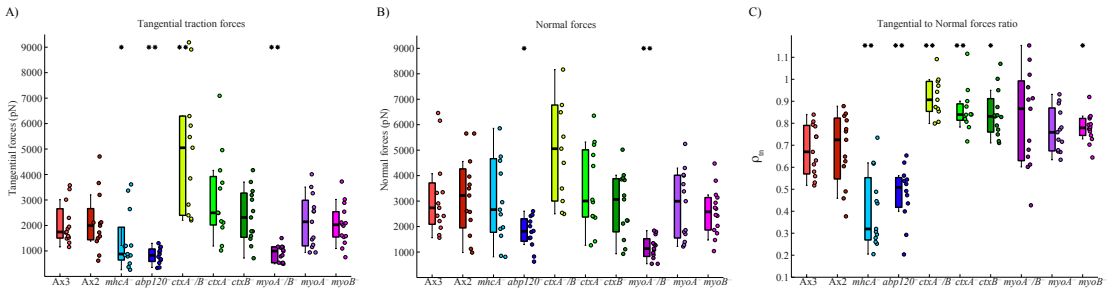


**Figure 3.19**: Tangential and normal forces' magnitude and ratio. (A) Average magnitude of the tangential traction forces in pN. (B) Average magnitude of the normal forces in pN. (C) Ratio between the tangential and normal forces' magnitude. The cell lines and number of cells (N) are indicated beneath the boxplot. Asterisks denote statistically significant differences between each specific mutant strain and its corresponding wild-type distribution (Wilcoxon ranksum test, * $p < 0.05$, ** $p < 0.01$).

between the magnitudes of the tangential and normal forces was quantified as:

$$\rho_{t,n} = \{\frac{< \sqrt{\tau_{zx}^2 + \tau_{zy}^2} >}{< |\tau_{zz}| >}\} \tag{3.4}$$

for each cell, where $<>$ and $\{\}$ denote respectively spatial and temporal average.

For both Ax3 and Ax2 wild-type strains, we calculated a mean value of $\rho_{t,n}$ equal to 0.68. The two cell lines with leading edge and posterior F-actin cross-linking defects, *abp120*$^-$ and *mhcA*$^-$, had similar mean values of $\rho_{t,n}$, which were both lower than the wild-type value: 0.40 for *mhcA*$^-$ cells and 0.48 for *abp120*$^-$ cells. On the other hand, the cell lines with cortical cross-linking defects, *ctxA*$^-$*/B*$^-$, *ctxA*$^-$ and *ctxB*$^-$ also had similar mean values of $\rho_{t,n}$, but these were higher than those of wild-type: 0.92, 0.86 and 0.84 for *ctxA*$^-$*/B*$^-$, *ctxA*$^-$ and *ctxB*$^-$, respectively. The cell lines with defective cross-linking between the membrane/cortex and the F-actin network, *myoA*$^-$*/B*$^-$, *myoA*$^-$ and *myoB*$^-$, also exhibited a higher ratio between the tangential and normal forces than the wild-type cells: 0.82, 0.77 and 0.78 for *myoA*$^-$*/B*$^-$, *myoA*$^-$ and *myoB*$^-$, respectively (Figure 3.19C), these ratios were intermediate between those of wild-type and cortexillin null cells.

For each of these four groups of cell types, the magnitudes of the normal and tangential forces were linearly proportional, but the value of the proportionality factor varied between groups (Figure 3.20). The scatter plots in Figure 3.20 clearly show that the ratio between the magnitude

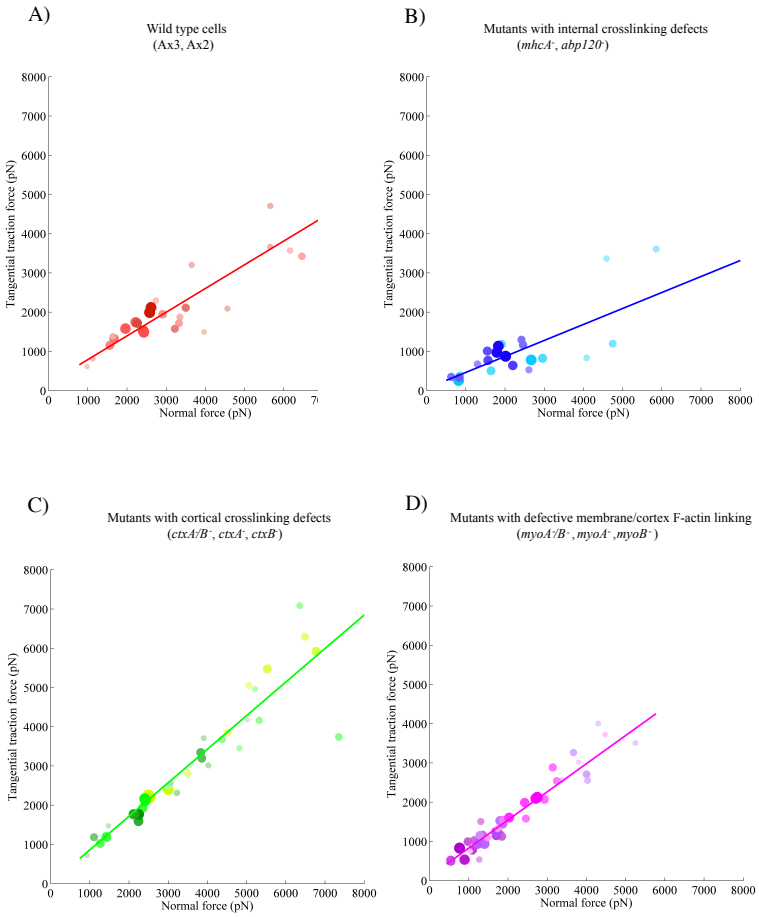


**Figure 3.20**: Scatter plots of the tangential versus normal force magnitudes. A) Scatter plot of the tangential versus normal force magnitudes for wild-type cells (Ax3 and Ax2). The data points represent N = 26 cells and the red line is the linear least-square fit applied to the data. The coefficient of determination of the data to the fitting is 0.83, and the slope of the line is 0.60. To better visualize the correlation, the plane was divided into rectangular tiles of equal area, and size and color of each data point were scaled according to the total number of data points that fall on each specific tile (i.e., its rate of occurrence). As a result, darker, larger circles represent those data points that were observed more often in our experiments, and vice versa. The colors of the circles in the scatter plots from panels A-D corresponding to each cell line are the same as the colors used in Figure 3.16. B) Scatter plot of the tangential versus normal force magnitudes for N = 13 *mhcA*$^{-}$ cells and N = 12 *abp120*$^{-}$ cells. The blue line, which is the linear least-square fit to the data has a slope of 0.41, and the coefficient of determination of the fitting is 0.69. C) Scatter plot of the tangential versus normal force magnitudes for N = 11 *ctxA*$^{-}$*/B*$^{-}$, N = 12 *ctxA*$^{-}$ and N = 13 *ctxB*$^{-}$ cells. The coefficient of determination of the least-square fit to the data is 0.94 and the slope is 0.86. D) Scatter plot of the tangential versus normal force magnitudes for N = 13 *myoA*$^{-}$*/B*$^{-}$, N = 13 *myoA*$^{-}$ and N = 14 *myoB*$^{-}$ cells. The coefficient of determination of the least-square fit to the data is 0.89 and the slope is 0.72.

of the tangential and normal traction forces is constant for each cell type. We observe that for all cell lines, the data fit straight lines with high coefficients of determination. The slopes of the straight lines fitted are approximately equal to the mean value of the ratio between the tangential and normal forces magnitude (0.69 for wild-type cells, 0.41 for mutant strains with leading edge and posterior cross-linking defects, 0.86 for mutant strains with cortical cross-linking defects and 0.72 for mutant strains with impaired connection between the membrane, cortex and intracellular F-actin). Therefore, we found that the ratio of the tangential to normal traction forces in migrating cells is constant for each cell line, but varies between different cell lines.

Mutant strains with cytoskeletal cross-linking defects rely more on the normal forces than wild-type cells when they move. The mutant strains that have their cytoskeletal contractility impaired (*mhcA*$^-$ and *abp120*$^-$) rely more on the pressure generated through cortical tension for the release of the back adhesions and the formation of the new protrusion than on the front-to-back contractility of the cytoskeleton. Mutants with cortical cross-linking defects (*ctxA*$^-$, *ctxB*$^-$ and *ctxA*$^-$*/B*$^-$) rely more on the tangential forces than wild-type cells for their movement, indicating that the traction forces are mainly driven by the axial and lateral contractility of the F-actin cytoskeleton. Myosin I null cells rely more on the tangential forces than wild-type cells for their movement since they have a well-organized F-actin cytoskeleton that provides an efficient, axial contractility.

Taken together, these results suggest that the cortical and the internal F-actin networks are two independent, yet interconnected generators of cellular force. Furthermore, the high scatter in $\rho_{t,n}$ observed in the *myoA*$^-$*/B*$^-$ cell population (Figure 3.19C) implies that the connection between these compartments requires the proteins MyoA and MyoB, which corroborates the conclusion that we inferred from the measurements of the correlation factors for the spatiotemporal evolution of the locations of the tangential and normal forces and for the temporal evolution of the magnitudes of the tangential and normal forces.

## 3.7 The nucleus is not generating the compressive normal forces

Stationary and migrating cells attached on flat surfaces have been shown to exert normal traction forces that are comparable in magnitude to the tangential ones [121] [41] [42]. However, how the various structural components of the cell contribute to the generation of these forces remains in dispute. For all the strains we analyzed, strong normal compressive forces appeared at one location near the cell center (Figures 3.5, 3.6, 3.9, 3.12). It has been speculated that downward compressive forces are due to the nucleus in *Dictyostelium discoideum* [105][71]. Hur et al. have measured the traction forces in bovine, aortic endothelial cells and also speculated that the nucleus must play a dominant role in the generation of the downward normal force that they measure near the cell's center [41], since it is the largest and stiffest compartment in the cell and it is tightly connected to the cytoskeleton [122] [123]. Maskarinec et al. and Franck et al. also measured a downward compression under the nucleus in fibroblasts [42][72]. In contrast, Legant et al., working with mouse embryo fibroblasts, did not measure any normal force under the nucleus and found that both the tangential and normal traction forces were restricted to the leading lamella [121].

To investigate the possible implication of the nucleus in the generation of downward normal forces, we simultaneously measured the three-dimensional cell-substrate forces and determined the location of the nucleus in wild-type *Dictyostelium* cells expressing H2B-GFP, which marks the nucleus fluorescently (*Dictyostelium* wild-type cells with their nucleus tagged by H2B-GFP, as explained in chapter 2 section 2.21).

Figure 3.21A-B shows a kymographic representation of the instantaneous tangential and normal cell-substrate forces together with the contour of the cell and the location of its nucleus. The spatial data are aligned so that the cell axis is parallel to the y-direction at each instant of time, and data from different instants of time are stacked together in the x-direction as explained in chapter 2 section 2.16. Using this representation, we observed that there are considerable periods of time where the nucleus is not located in the area where the cell is compressing the substrate. In fact, there are long periods of time where the nucleus co-localizes with areas in which the cell is

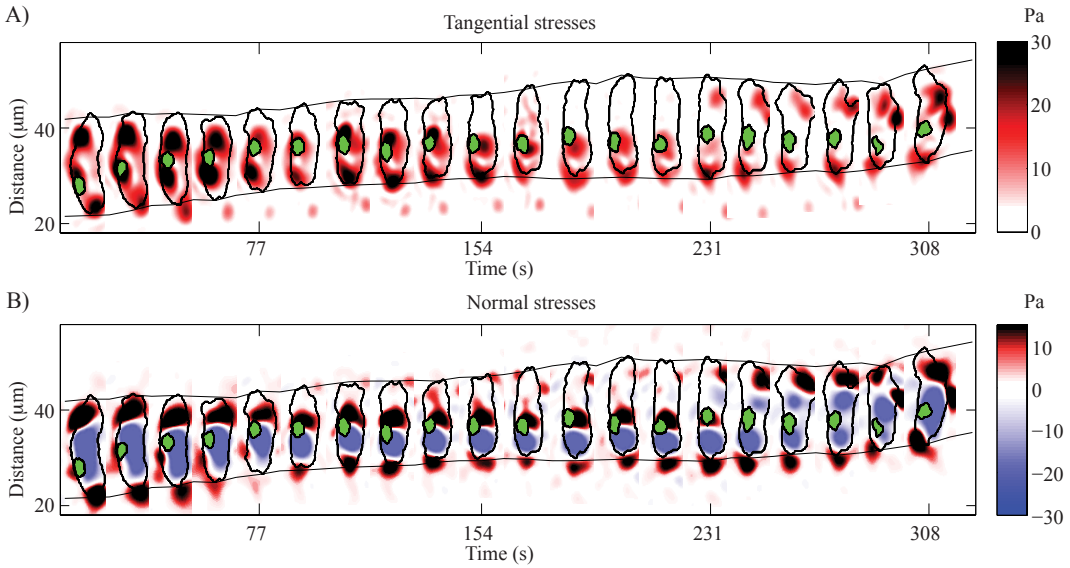


**Figure 3.21**: Kymographs of the tangential and normal stresses' instantaneous magnitude and localization of the nucleus. A) Spatiotemporal kymograph of the instantaneous magnitude of the tangential traction stresses as a function of the position along the cell trajectory and time, for a representative wild-type cell. The instantaneous magnitude of the tangential traction stresses (colorbar on the right), localization of nucleus (green) and cell contours (black) are displayed every 14 s. The grey envelope lines represent the time-evolving position of the front and back edges of the cells. B) Same as in panel A for the instantaneous normal stresses (colormap on the right, red color indicates the cell is pulling upwards while blue indicates the cell is pushing downwards).

pulling upwards (Figure 3.21B).

Interestingly, we found that the normal forces in *myoA⁻/B⁻* cells are approximately 3 times lower than in wild-type cells (Figure 3.19B). We calculated the volume of the nucleus for these two cell lines, as explained in chapter 2 section 2.18 and we found that the volume of their nuclei are very similar (Figure 3.22), indicating that the magnitude of the normal compression forces does not correlate with the size of the nucleus.

We calculated the correlation coefficient between the minimum normal tension exerted by the cell and the location of the nucleus centroid (Figure 3.23), as explained in chapter 2 section 2.15. Consistent with our observations, we found that the coefficient of correlation between nuclear position and the location of maximum compressive force is approximately equal to zero (Figure 3.24). These results indicate that in *Dictyostelium* cells, the nucleus does not take part

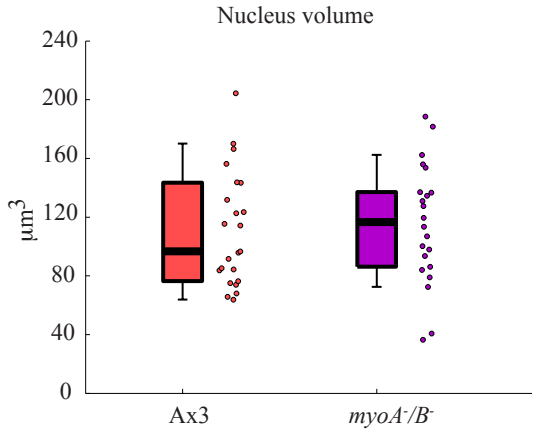


**Figure 3.22**: Nucleus volume for Ax3 cells (N = 23) and *myoA⁻/B⁻* cells (N = 22), calculated using IMARIS software.

in the generation of the normal compressive forces exerted during migration. We note, however, that *Dictyostelium* cells have smaller nuclei compared to other cell types. Our results do not rule out that the stiffness of the nucleus may play some role in the generation of normal compressive forces in mammalian cells or other cell types with a larger nucleus.

## 3.8 Cortical tension is balanced by increased cytoplasmic pressure causing compressive forces on the substrate

The cytosol is an incompressible medium with mechanical properties similar to those of water that can sustain hydrostatic pressure. When the cells migrate, they contract inward producing an internal pressure that is compensated by the cortical tension. Thus, we postulated that cell-substrate compressive forces are mediated by an increase in cytosolic pressure that balances the tension generated at the cell cortex. This model is analogous to the Young-Laplace's theory that describes the increase of pressure created by surface tension across the interface between two fluids.

To test this hypothesis, we estimated the relative intracellular pressure of the different strains from the measurements of the compressive normal stresses applied by cells on the substrate

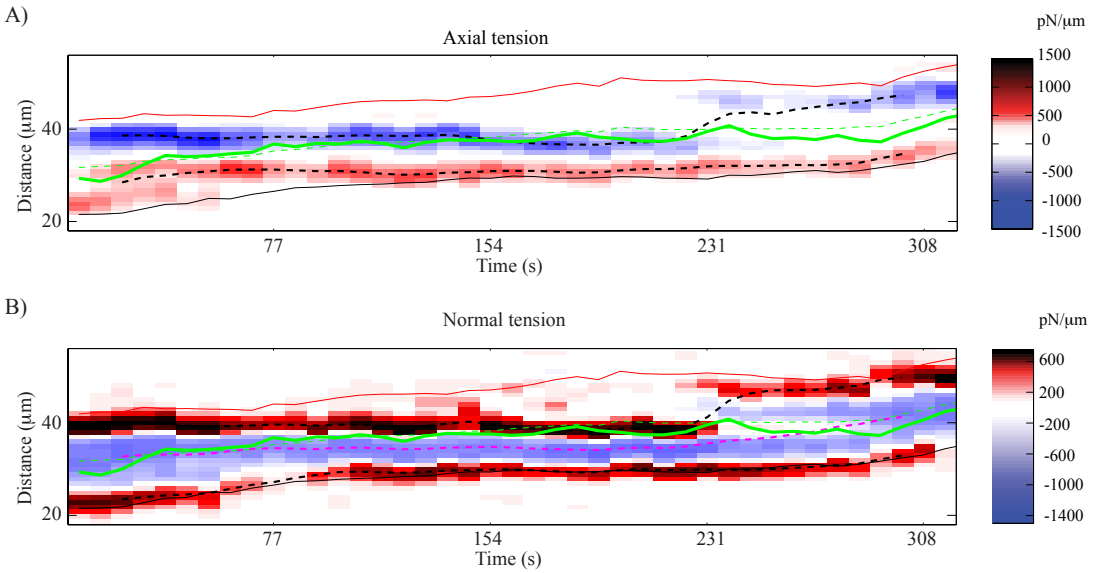


**Figure 3.23**: Kymographic representation of the spatiotemporal evolution of the axial and normal tension and location of the nucleus' centroid. A) Spatiotemporal representation of the axial tension, $T_x(x,t)$, as a function of the position along the cell trajectory and time for a representative wild-type cell expressing H2B-GFP. The solid-red line represents the location of the cell's front. The solid-black line represents the location of the cell's back. The dotted-black lines indicate the location of the maximum and minimum axial tension in the cells's rear and frontal part, respectively. The dotted-green line show the position of the cell's centroid. The solid-green line represents the location of the nucleus' centroid. B) Spatiotemporal representation of the normal tension, $T_z(x,t)$, as a function of the position along the cell trajectory and time for a representative wild-type cell expressing H2B-GFP. The solid-red line represents the location of the cell's front. The solid-black line represents the location of the cell's back. The dotted-black lines indicate the location of the maximum normal tension in the cells's rear and frontal part. The dotted-magenta line shows the location of the minimum normal tension. The dotted-green line show the position of the cell's centroid. The solid-green line represents the location of the nucleus' centroid.

and used Young-Laplace's law to estimate the cortical tension of the cells by applying an equilibrium of forces in the normal direction, as shown in Figure 3.25A-C. We approximated the shape of the cell as an equivalent hemisphere of radius $R$ equal to half the cell length, which is a reasonable assumption for *Dictyostelium* cells [102], leading to:

$$\gamma = \frac{<\tau_{zz}> R}{2} \tag{3.5}$$

where $<\tau_{zz}>$ represents the average of the maximum value of the compressive, normal cell-

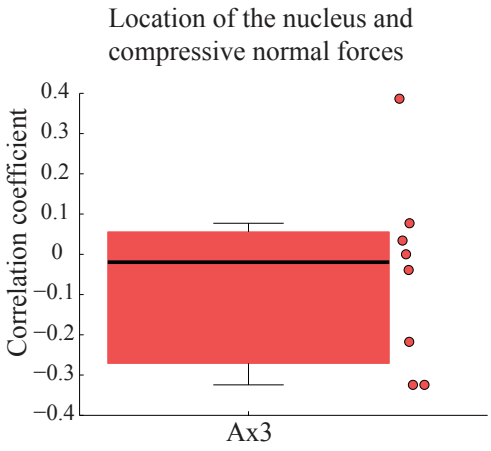


**Figure 3.24**: Boxplot of the Spearman correlation coefficient between the location of the maximum negative normal tension and the location of the nucleus for Ax3 cells expressing H2B-GFP (N=8).

substrate stresses generated by a cell at each instant of time. In the context of our experiments, eq. 3.5 should be taken as an estimation that allowed us to test if the pulling forces exerted by the cells on their substrate are balanced by a rise in intracellular pressure, rather than a model to estimate the cortical tension, for which more accurate techniques are available [124].

However, even if our model neglects the non-spherical shape of the cell, the pressure sustained by the internal cytoskeleton and the regulation of cell-substrate adhesions, the values of the estimated cortical tension (Figure 3.26) are in good agreement with previous data obtained by micropipette aspiration. Previous studies calculating the cortical tension of *Dictyostelium* wild-type cells reported an approximate value of 1mN/m [125][124][126][127]. In *mhcA*$^-$ cells, we measured a 25% reduction in cortical tension compared to wild-type cells (Figure 3.26). This reduction is also in agreement with the 20% decrease previously reported for these mutant stains from micropipette aspiration experiments [126], and the 30% reduction estimated by needle poking methods [128]. In the *myoA*$^-$*/B*$^-$ cells, we measured a 64% reduction in the cortical tension (Figure 3.26), also in agreement with previous micropipette aspiration measurements that reported approximately a 60% reduction [124][129]. In *myoA*$^-$ and *myoB*$^-$ cells we found a 12% reduction which is equal to the reduction reported by Dai et al. through micropippete aspiration

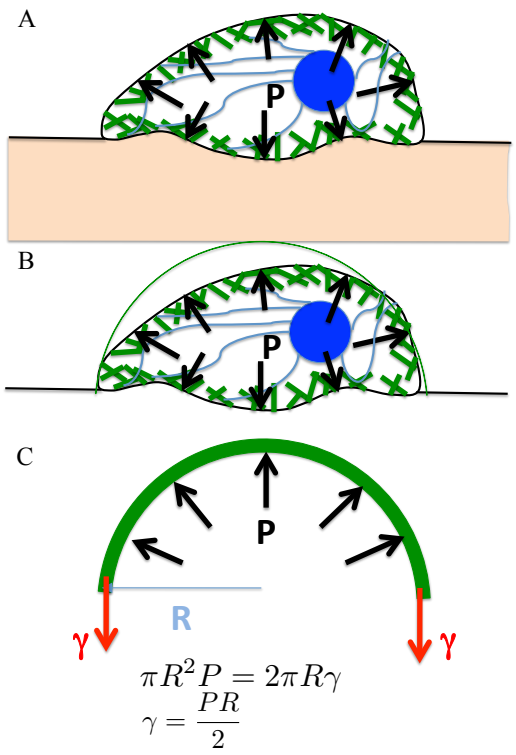


**Figure 3.25**: Sketch of a cell's internal pressure and cortical tension estimation. A) Sketch of a cell that undergoes an internal pressure and exerts a deformation on the substrate while moving. B) Approximation of the cell shape by a sphere of radius equal to the cell's length. C) Cortical tension estimation by balancing the force generated by the cortical tension and the internal pressure of the cell.

[124]. In filamin null cells, Luo et al. found a reduction in cortical tension of approximately 20% using micropipette aspiration [127], whereas in our case, we measured a larger reduction of 46% (Figure 3.26). Kee et al. measured the cortical tension of cortexillin mutant strains using micropipette aspiration. They found that the *cxtB*$^-$ cells had a 16% increase in cortical tension, and that the cortical tension was reduced by 35% and 60% in *cxtA*$^-$ and *cxtA*$^-$*/B*$^-$ respectively [130]. In contrast, we found that the *cxtA*$^-$ and *cxtB*$^-$ mutant strains exhibit a decrease of 8% and 5% respectively, and *cxtA*$^-$*/B*$^-$ cells an increase of 10% (Figure 3.26).

Taken as a whole, the above estimates of the cortical tension from the measured values of the downward compression forces that the cell exerts on the substrate demonstrate that the normal component of the cell traction forces are mainly due to the cortical tension. Thus, we concluded

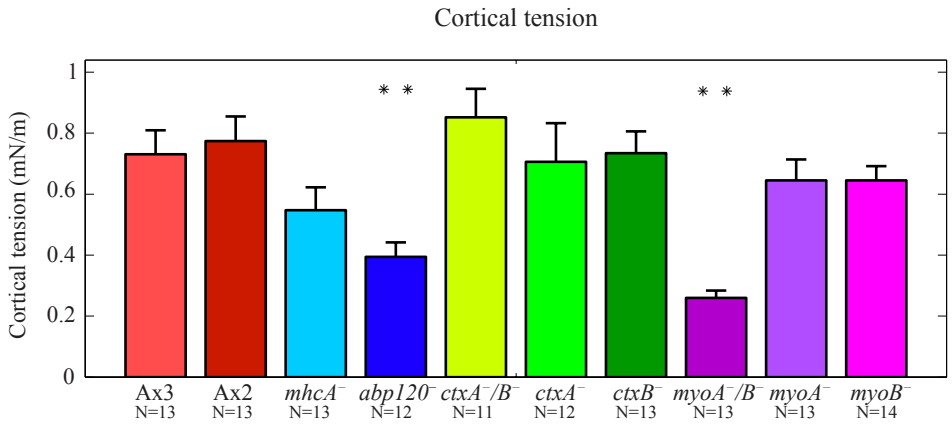


**Figure 3.26**: Barplot of the cortical tension in mN/m for the cell lines and number of cells (N) indicated. Asterisks denote statistically significant differences between each specific mutant strain and its corresponding wild-type distribution (Wilcoxon ranksum test, ** $p < 0.01$)

that cortical tension in migrating amoeboid cells is balanced by increased cytoplasmic pressure that causes the measured compressive forces on the substrate.

To further demonstrate this, we performed experiments with wild-type cells immersed in buffer solutions with different osmolarities. A change in the osmolarity of the surrounding medium produces a variation in the internal pressure of the cells. *Dictyostelium* cells do not accumulate osmolytes to counteract the osmotic pressure applied [131][132]. Instead, they remodel their cytoskeleton and increase their cortical tension, building a rigid network that provides an osmoprotective mechanism [133] [134][135]. We measured the compressive normal stresses in wild-type cells immersed in a 100mM sorbitol medium, and from their magnitude we calculated a cortical tension of $3.03 \pm 1.19$mN/m, which is a 31% increase with respect to the value in the control Na/K phosphate buffer solution. These results demonstrate that the magnitude of the downward normal forces increases as the cortical tension increases, which is consistent with the above statement that the normal traction forces are mainly due to cortical tension.

The force generated through the cortical tension has a direction that follows the contact angle between the cell and the substrate at the edge of the cell (Figure 3.27). The forces that are generated by the cortical tension have components in the tangential and normal directions. There-

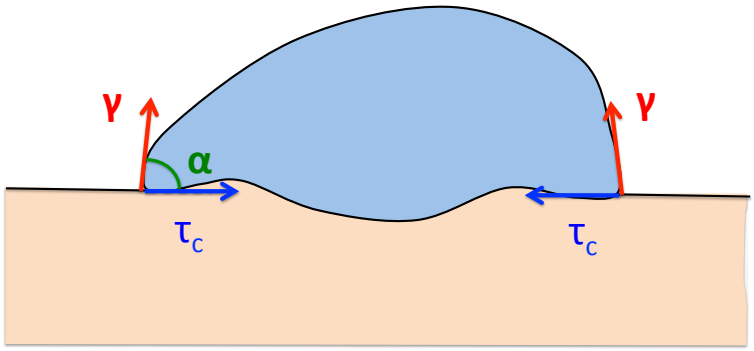


**Figure 3.27**: Sketch showing the proposed two mechanisms for the generation of the forces. $\gamma$ is the cortical tension, $\tau_c$ is the traction force exerted by the acto-myosin contractility of the cytoskeleton, and $\alpha$ is the contact angle between the cell and the substrate.

fore, the tangential forces that we measured come from two contributions, from the cytoskeletal contractility and from the cortical tension. This could be modeled as:

$$\tau_t = \gamma \cdot \frac{L}{2} \cdot cos(\alpha) + \tau_c \tag{3.6}$$

$$\tau_n = \gamma \cdot \frac{L}{2} \cdot sin(\alpha) \tag{3.7}$$

where $\tau_t$ is the tangential traction force, $\tau_n$ is the normal force, $\gamma$ is the cortical tension, $\tau_c$ is the traction force exerted by the acto-myosin contractility of the cytoskeleton, $L$ is the length of the cell, and $\alpha$ is the contact angle between the cell and the substrate. In our case, we can not accurately measure the contact angle between the cell and the substrate. This decomposition implies that the force that is generated by the cortical tension has one component that is tangential and another that is normal, and the ratio between these two components depends on the contact angle $\alpha$. Therefore, the mutant cells that have defective cytoskeletal cross-linking or disrupted contractility (*mhcA*$^-$ and *abp120*$^-$) would have a $\tau_c$ that is small, and the tangential forces that we measured would mainly come from the cortical tension.

## 3.9 The speed of amoeboid movement correlates with the ratio between the magnitudes of the tangential and normal cell-substrate forces

The speed of amoeboid migration is related to the ability of cells to form and release their adhesions and is limited by the rate at which the cell can make the required shape changes to form a new pseudopod and retract their rear part [90] [24] [30]. Efficient amoeboid cell movement requires a contraction driven by the axial forces and a softening of the anterior cortex that allows the cells to form the new protrusion. Thus, we hypothesized that the cells' efficient movement depends on the relative strengths of the front-to-back axial contraction and the force generated through cortical tension. Consistent with this hypothesis, we found clear indications that the cell migration speed, v, increases considerably with the ratio of the tangential to normal cell-substrate forces, $\rho_{t,n}$ (Figure 3.28). Note that while the cell migration speed is v $\approx$ 6 to 8 $\mu$m/min when $\rho_{t,n} < 0.5$, it increases almost 3 fold up to v $\approx$18 to 20 $\mu$m/min when $\rho_{t,n} \approx 1$. Figure 3.28A-B shows the best least-square fit to the observed dependence of the velocity on the ratio between the magnitudes of the tangential and normal forces, that was given by the following equation:

$$\mathrm{v} = a + b\rho_{t,n}^{c} \tag{3.8}$$

The exponent that gave a better fit of the data was, $c \approx 1.8$.

On the other hand, we found no correlation between the velocity of migration and the magnitude of either the tangential or the normal cell-substrate forces alone, as shows Figure 3.29A-B. Therefore, we didn't find any connection between the velocity of migration and the tangential or normal forces independently. This argument is also supported by the fact that cells with lower velocities of migration showed reduced fluctuations in their aspect ratio (Figure 3.30), which may be related to a difficulty in overcoming the cortical tension through the front-to back axial contractility.

Another possible explanation for the cells moving with lower velocity when the ratio

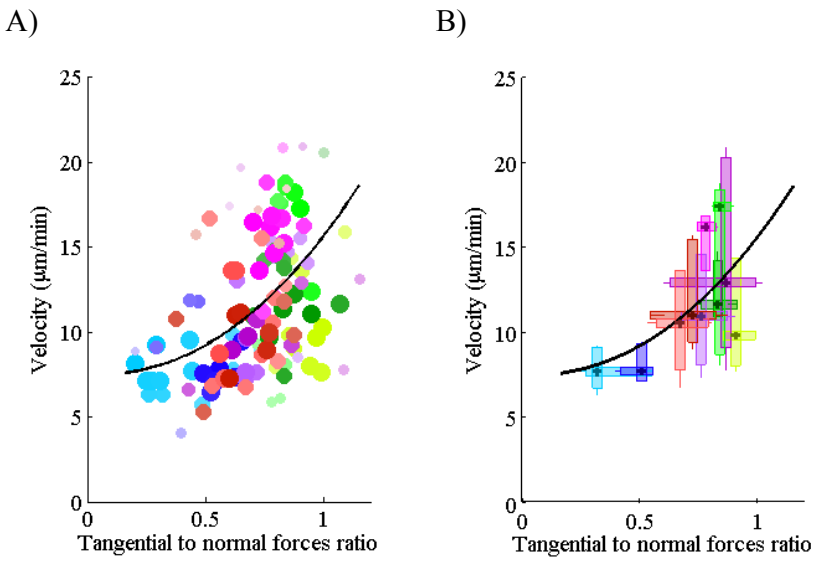


**Figure 3.28**: Scatter plot and box plots of the cells' mean velocity versus the average ratio between the magnitudes of the tangential and normal forces. A) Scatter plot of the cells' mean velocity versus the average ratio between the magnitudes of the tangential and normal forces. The colors of the circles in the scatter plot for each cell line correspond to the colors used in Figure 3.16. The number of cells for each cell line is the same as in Figure 3.16. To better visualize the correlation, the plane was divided into rectangular tiles of equal area, and size and color of each data point were scaled according to the total number of data points that fall on each specific tile (i.e., its rate of occurrence). As a result, darker, larger circles represent those data points that were observed more often in our experiments, and vice versa. B) Vertical boxplots indicate the velocity of migration of the cell lines examined. The colors of the boxplot for each cell line are the same as in Figure 3.16. Horizontal boxplots indicate the tangential to normal force ratio for the same cell lines. The black line represents the best polynomial least-square fit to the data (eq. 3.8), with an exponent $c \approx 1.8$.

of the tangential to the normal forces is lower could be that the normal forces cause the cells to sink deeper into the substrate. However, we did not find a correlation between the migration velocity and the magnitude of the deformation that the cell exerts in the normal direction, as shows Figure 3.29C. Therefore, there is not relationship between the velocity of migration and the z-displacement generated by the cells into the substrate.

We concluded that the cell migration speed increases when the tangential forces generated by the axial acto-myosin contractility are able to balance the normal forces produced through the cellular cortical tension. When this is the case, the cells are able to produce the cell shape changes needed for locomotion and move faster.

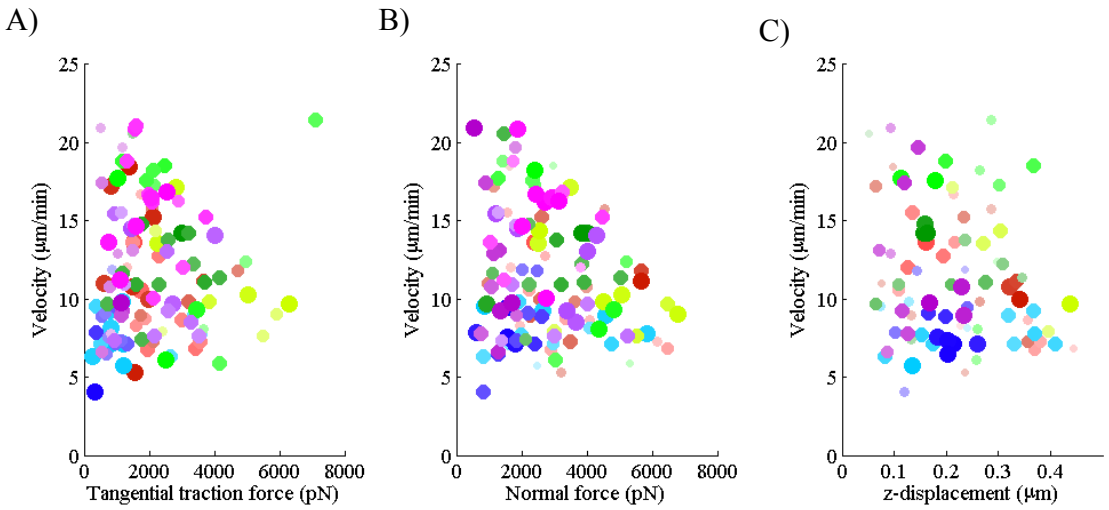


**Figure 3.29**: Scatter plot of the cells' mean velocity versus the average magnitude of the tangential traction forces, the normal forces and the average magnitude of the displacement exerted in the normal direction. A) Scatter plot of the cells' mean velocity versus the average magnitude of the tangential traction forces. B) Scatter plot of the cells' mean velocity versus the average magnitude of the normal forces. C) Scatter plot of the cells' mean velocity versus the average magnitude of the displacement exerted in the normal direction to the substrate. The colors of the circles in the scatter plots for each cell line correspond to the colors used in Figure 3.16. The number of cells for each cell line is the same as in Figure 3.16. To better visualize the correlation, the plane was divided into rectangular tiles of equal area, and size and color of each data point were scaled according to the total number of data points that fall on each specific tile (i.e., its rate of occurrence). As a result, darker, larger circles represent those data points that were observed more often in our experiments, and vice versa.

## 3.10 Cortical tension and cell shape relationship

Cortical tension also plays a major role in controlling cells' shape. When the cells have lower cortical tension, they are flatter and more spread out over the substrate compared to cells with higher internal pressure that have a more spherical shape. In order to calculate the volume of the cells, we transformed the cells with a vector encoding Lifeact fused to GFP [99] and acquired z-stack of fluorescent images. We performed a volume rendering for each instant of time using IMARIS software (Bitplane) and calculated the volume of each cell. The area of the cell was calculated through the maximum intensity projection of the actin distribution, using MATLAB. We found that the non-dimensional ratio between the volume and the contact area in wild-type cells is higher than in *mhcA*$^{-}$ cells, suggesting that the cells are flatter when the cortical tension

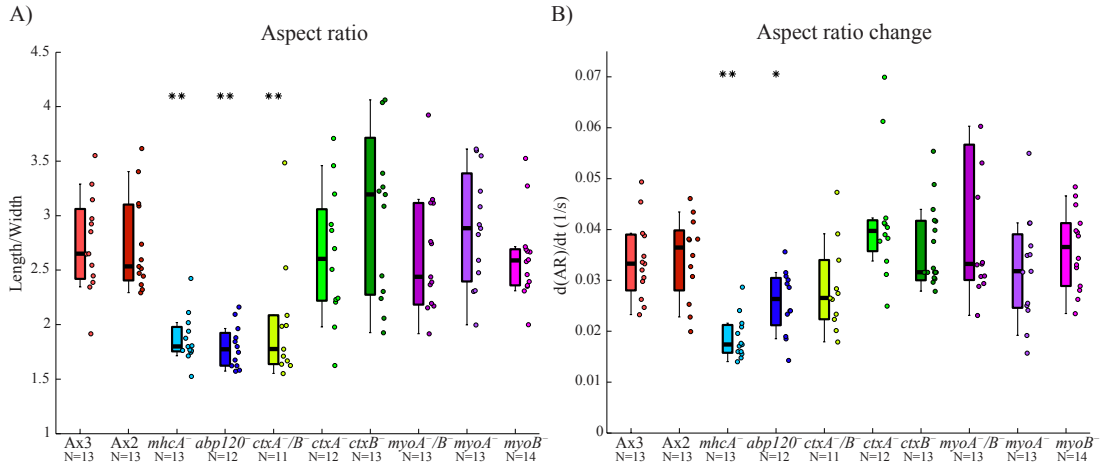


**Figure 3.30**: Cell aspect ratio and change with time of the cell's aspect ratio. A) Cell shape aspect ratio (ratio between the cell length and width) for the cell lines and number of cells (N) indicated. B) Aspect ratio change with time (derivative of the aspect ratio with respect to the time) for the cell lines and number of cells (N) indicated.

is lower (Figure 3.31). The decrease in volume to contact area ratio in *mhcA*$^-$ cells with respect to wild-type cells is 24%, similar to the 25% decrease in cortical tension that we find for these cells. Figure 3.31 shows that the non-dimensional volume to area ratio of *mhcA*$^-$ cells is similar to that of a semi-sphere, whereas for the case of wild-type cells this non-dimensional ratio is significantly higher.

## 3.11 Cell migration requires either cortical integrity or acto-myosin contractility

To study the interplay between the mechanisms generating the axial acto-myosin contractility and the cortical tension, we examined the migration of cells lacking the cortical cross-linking and the myosin II mediated contractility. We used blebbistatin, which is a cell-permeable inhibitor with high affinity and selectivity towards myosin II [136]. Cells treated with blebbistatin have the myosin II dependent processes inhibited [137]. Blebbistatin binds to the motor domain of myosin II and it potently inhibits *Dictyostelium* myosin II [138].

We calculated the forces generated by wild-type cells chemotaxing in 50$\mu$M blebbistatin

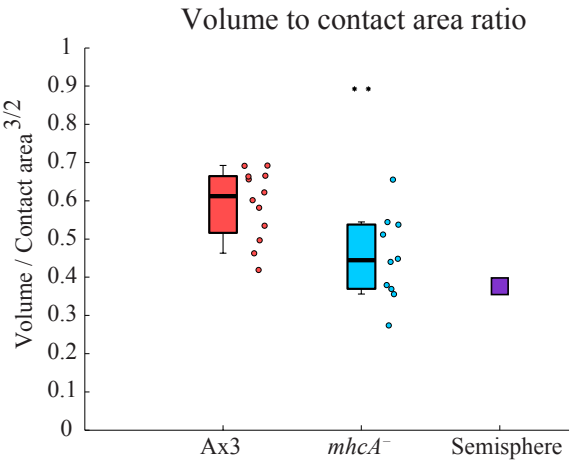


**Figure 3.31**: Non-dimensional ratio between the cell volume and contact area (Volume/Contact area$^{3/2}$) for Ax3 cells (N= 12) and *mhcA*$^-$ cells (N=10) and the value for a semi-sphere. Two asterisks denote statistically significant differences between medians ($p < 0.01$).

Na/K buffer, as explained in chapter 2 section 2.3. We found that the magnitude and distribution of the tangential and normal cell-substrate forces generated by wild-type cells treated with blebbistatin are very similar to the forces exerted by *mhcA*$^-$ cells, as shown in Figure 3.32. The tangential traction forces and the pulling normal forces are localized around the peripheral cortex in both, *mhcA*$^-$ cells and blebbistatin-treated wild-type cells. The ratio between the magnitudes of tangential and normal forces, $\rho_{tn}$, in blebbistatin-treated wild-type cells was similar to that of *mhcA*$^-$ cells and lower than in wild-type cells, as shown in Figure 3.33. This indicates that the mechanism generating the cell-substrate forces when blebbistatin is added relies more in the cortical tension generated by the cells than in the axial contractility.

Blebbistatin reduces the migration velocity of wild-type cells, as expected, and the speed of wild-type cells in the presence of blebbistatin is approximately equal to that of *mhcA*$^-$ cells, as shown in Figure 3.34. Additionally, the average shape of the wild-type cells when they are treated with blebbistatin becomes more rounded and it is very similar to the average shape of *mhcA*$^-$ cells, as can be observed in the average contours from Figure 3.32. Consequently, the effect of the 50$\mu$M blebbistatin treatment in wild-type cells is analogous to that of the depletion of myosin II in *mhcA*$^-$ cells, in terms of shape, speed of migration, magnitude and distribution of

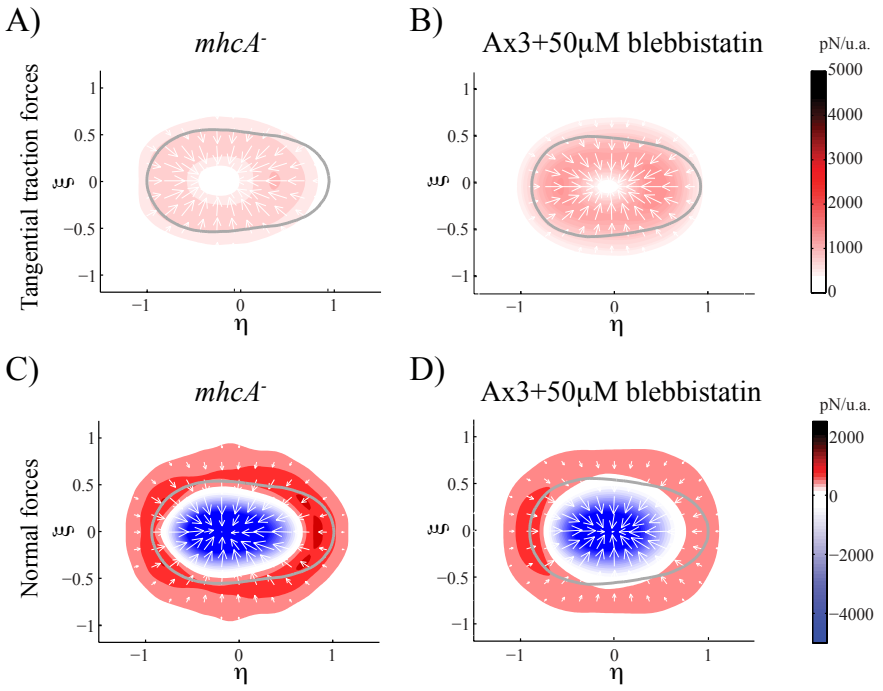


**Figure 3.32**: Tangential and normal cell-substrate forces exerted by *mhcA*$^-$ cells and blebbistatin-treated wild-type cells. A) Average tangential traction forces per unit area in pN per unit area (colorbar on the right) exerted by *mhcA*$^-$ cells, (N=13 cells). The gray line indicates the average contour of the cells. The white arrows show the direction of the cell-substrate forces. B) Average tangential traction forces per unit area in pN per unit area (colorbar on the right) exerted by wild type cells that have myosin II inhibited by blebbistatin (50 $\mu$M), (N=11 cells). The gray line indicates the average contour of the cells. The white arrows show the direction of the cell-substrate forces. C) Average normal forces per unit area in pN per unit area (colorbar on the right) exerted by *mhcA*$^-$ cells, (N=13 cells). B) Average normal forces per unit area in pN per unit area (colorbar on the right) exerted by wild type cells that have myosin II inhibited by blebbistatin (50 $\mu$M), (N=11 cells).

the tangential and normal forces.

To study the joint effect of the inhibition of the cortical integrity and the acto-myosin contractility, we treated cortexillin null cells with 50$\mu$M blebbistatin. When myosin II is inhibited by blebbistatin treatment in cells laking cortexillin I, cortexillin II or both proteins, these cells are not able to migrate over the substrate. We calculated the tangential and normal forces exerted by *ctxA*$^-$, *ctxB*$^-$ and *ctxA*$^-$*/B*$^-$ cells treated with 50$\mu$M blebbistatin, but in this case, since the cells do not move, the reference image necessary to calculate the forces was acquired by detaching the cells by adding SDS, as explained in chapter 2 section 2.7. *CtxA*$^-$, *ctxB*$^-$ and *ctxA*$^-$*/B*$^-$ cells

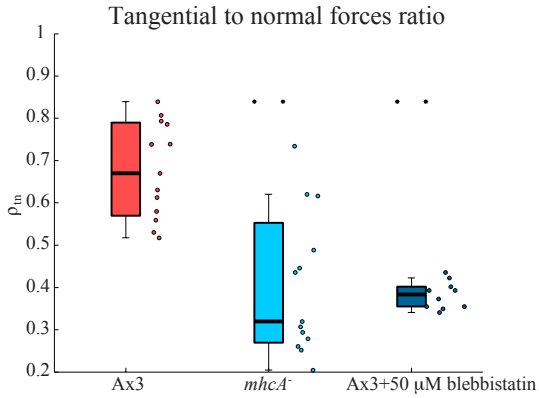


**Figure 3.33**: Ratio between the tangential and normal forces' magnitude for *mhcA*$^-$ cells (N = 13 cells) and blebbistatin-treated wild-type cells (N = 11 cells). The cell lines are indicated beneath the boxplot. Asterisks denote statistically significant differences between each specific cell line and the corresponding wild-type distribution (Wilcoxon ranksum test, ** $p < 0.01$).

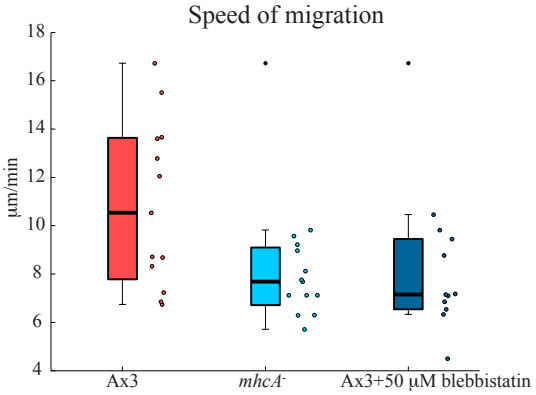


**Figure 3.34**: Speed of migration of *mhcA*$^-$ cells (N=13 cells) and blebbistatin-treated wild-type cells (N=11 cells). The cell lines are indicated beneath the boxplot. Asterisks denote statistically significant differences between each specific cell line and the wild-type distribution (Wilcoxon ranksum test, * $p < 0.05$).

treated with 50$\mu$M blebbistatin generate high contractile tangential traction forces and pulling normal forces all around the cell periphery, as shown in Figure 3.35. However, although they are able to generate high forces, they can to move. These cells are not able to modulate their cortical tension to produce movement. In this case, the cells are not able to generate axial contractions that counterbalance their cortical tension and therefore they can not migrate. This indicates that

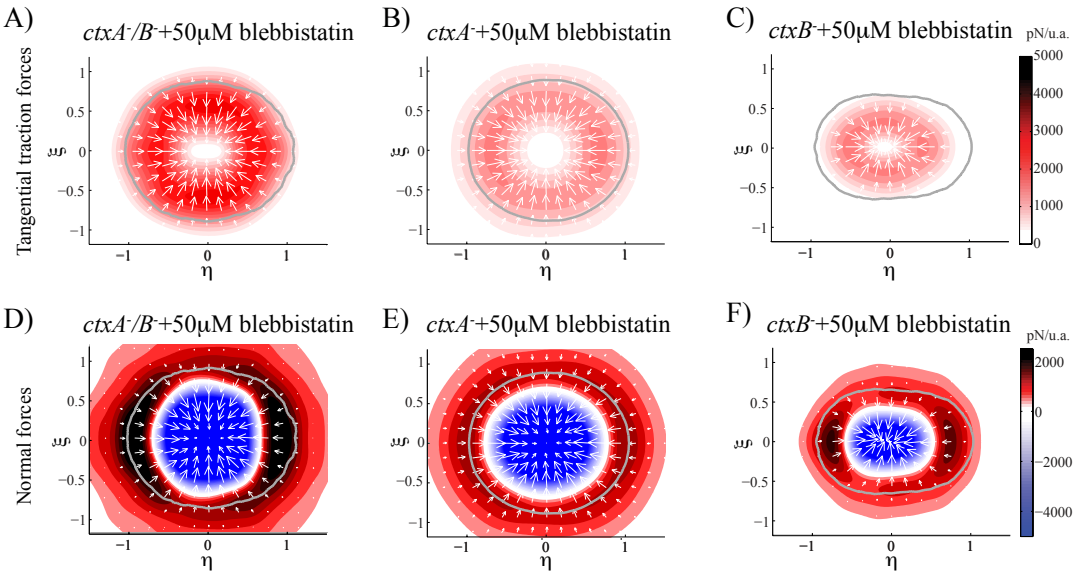


**Figure 3.35**: Tangential and normal cell-substrate forces exerted by cortexillin null cells that have myosin II inhibited by blebbistatin. A) Average tangential traction forces per unit area in pN per unit area (colorbar on the right) exerted by *ctxA⁻/B⁻* cells that have myosin II inhibited by blebbistatin, (N=6 cells). The white arrows indicate the direction of the average tangential traction forces. The gray line indicates the average contour of the cells. B) Average tangential traction forces per unit area in pN per unit area (colorbar on the right) exerted by *ctxA⁻* cells that have myosin II inhibited by blebbistatin, (N=5 cells). C) Average tangential traction forces per unit area in pN per unit area (colorbar on the right) exerted by *ctxB⁻* cells that have myosin II inhibited by blebbistatin, (N=5 cells). D) Average normal forces per unit area in pN per unit area (colorbar on the right) exerted by *ctxA⁻/B⁻* cells that have myosin II inhibited by blebbistatin, (N=6 cells). E) Average normal forces per unit area in pN per unit area (colorbar on the right) exerted by *ctxA⁻* cells that have myosin II inhibited by blebbistatin, (N=5 cells). F) Average normal forces per unit area in pN per unit area (colorbar on the right) exerted by *ctxB⁻* cells that have myosin II inhibited by blebbistatin, (N=5 cells).

the cortical integrity and the acto-myosin contractility are two counteracting mechanisms for the generation of the cell-substrate forces and cells can move when one of these mechanisms is working properly, but they can not if both mechanisms are impaired.

The F-actin distribution in wild-type cells that have myosin II inhibited by blebbistatin is very similar to the actin distribution of *mhcA⁻* cells and the actin is localized at the cells' front, as shown in Figures 3.36A and Figure 3.11B. Consequently, this corroborates as well that blebbistatin has a similar effect than the depletion of myosin II in *Dictyostelium* cells.

We showed that the F-actin in *ctxA⁻/B⁻* cells is distributed all around the periphery of the cells (Figure 3.11C and Figure 3.10C). Nevertheless, the F-actin reorganizes when *ctxA⁻/B⁻*

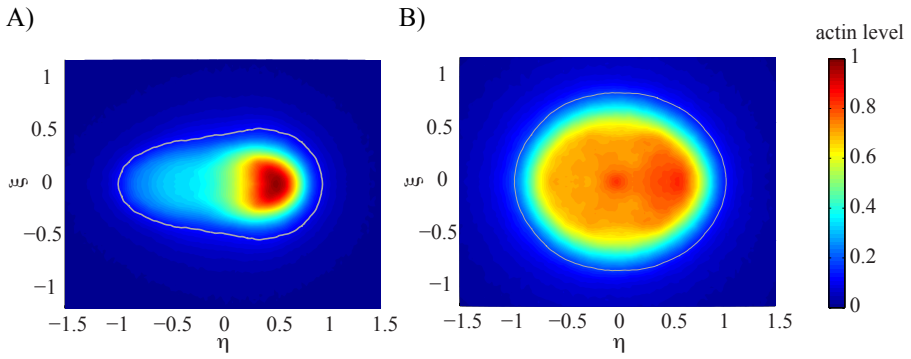


**Figure 3.36**: Average two-dimensional projection of the F-actin distribution in wild-type cells and *ctxA⁻/B⁻* cells that have myosin II inhibited by blebbistatin. A) Average two-dimensional projection of the F-actin distribution in wild-type cells treated with blebbistatin (50 $\mu$M), (N=10 cells). B) Average two-dimensional projection of the F-actin distribution in *ctxA⁻/B⁻* cells treated with blebbistatin (50 $\mu$M), (N=9 cells).

cells are treated with blebbistatin and in this case it is not localized around the cortex, but it is evenly distributed inside the cytoskeleton. The F-actin cytoskeleton needs to be organized in a way that allows the cells to counterbalance the cortical tension through axial contractions, and when cortexillin and myosin are impaired, the cells fail to initiate the movement.

## 3.12 Discussion

Fast amoeboid cell migration involves large cell shape changes [102] and requires cells to apply mechanical forces on their surroundings via transient adhesions [104] [139]. However, the role of the cell-generated forces in this process is not understood, to the point that a relationship between the strength of these forces and the migration speed is yet to be found [90] [40]. This lack of understanding contrasts with the case of slower migrating mesenchymal cells such as fibroblasts, where the dependence between cell speed and the strength of cell-substrate adhesions has been demonstrated experimentally [140] and theoretically [141]. Furthermore, amoeboid cells move in a highly three-dimensional manner and exert three-dimensional forces even while crawling on flat surfaces [105] [43] [142], but the vast majority of existing measurements of cell-generated forces are two-dimensional, neglecting the possible role that the forces perpendicular

to the substrate may play in the migration process.

To investigate the role of the cellular forces in establishing the speed of amoeboid migration, we measured the three-dimensional forces exerted by chemotaxing *Dictyostelium* cells on flat elastic substrates using 3DTFM [43]. We considered wild-type cells and eight different mutant strains with defective actin cross-linking and cortical integrity. Our measurements suggest that cells can modulate their three-dimensional shape and move faster if they are able to generate periodic axial contractions that counterbalance the tension of their cortex. For a long time, the tangential traction forces exerted by crawling cells were known to be much greater than needed to overcome the external resistance of the environment [90] [75], but the biological or mechanical reasons why the cells exert these forces were unknown. Our findings suggest a reasonable mechanistic explanation for the existence of such large traction forces.

The new three-dimensional force measurements presented in this study revealed that amoeboid cells exert forces on their substrate using two distinct mechanisms. In addition to the axial forces mediated by acto-myosin contractility that had been previously described by 2D force microscopy [90] [24], we demonstrated that the thin actin cortex at the cell membrane can generate significant 3D forces. The spatial pattern of this cortical force was isolated in cells lacking internal F-actin cross-linking (*mhcA*$^{-}$ and *abp120*$^{-}$), which exhibit reduced acto-myosin contractility. It consists of an annular region of inward and upward pulling at the cell edge, surrounding a central region where the cell pushes down on the substrate. Similar patterns have been shown to be caused by liquid drops or liposomes when placed onto soft substrates [114] [143], where interface tension is the only source for the measured forces. Mathematical models for the generation of traction forces have suggested the importance of interface tension as well [144] [145] [146].

Plasma membrane tension is reported to be approximately 1000 times lower than cortical tension in *Dictyostelium* [127] [147]. Furthermore, liposomes that have an actin cortex attached to the membrane can withstand tensions up to 0.3 mN/m when placed onto soft substrates before breaking [143], which is similar to the cortical tension reported for *Dictyostelium*. Therefore, the membrane should contribute little to the generation of 3D substrate forces in comparison to the

actin cortex. Consequently, the cortical component of the cell-generated forces was found to be significantly lower than the axial contractility component in strains with cortical cross-linking defects (*ctxA⁻/B⁻*, *ctxA⁻*, *ctxB⁻*), and in strains that are defective in linking the F-actin to the plasma membrane (*myoA⁻/B⁻*, *myoA⁻*, *myoB⁻*).

In *Dictyostelium* cells, axial contractile forces are generated and transmitted by a dense F-actin network that is regulated by F-actin cross-linking and acto-myosin contractility [48] [24] [30]. In the absence of axial contractility, the shape of the cell is rounder and less dynamic, as expected for a compartment confined by its surface tension, and the frequency of pseudopod protrusion is decreased [24] [148]. Cells lacking F-actin cross-linkers may rely on the in-situ modulation of cortical tension to control their shape and migrate [59].

Our measurements indicate that the interplay between the axial contractility and the cortical tension controls the forces exerted by migrating cells and their speed. Mechanical tension in the plasma membrane plays an important role in cell migration by spatially confining the signals for F-actin polymerization [149]. In cells moving by extending thin, stable lamellipodia, membrane tension has been shown to determine lamellipodial shape and extension rate [54] [150]. However, the actual mechanisms used by migrating cells to actively regulate their membrane tension are not well understood. Our studies suggest that axial contraction and cortical cross-linking may contribute to this function jointly. Furthermore, the lack of correlation between cortical tension and axial contractility that we observed in *myoA⁻/B⁻* cells suggests that myosin I may be necessary for the proper communication of forces between the plasma membrane and the cortical and intracellular cytoskeletal networks.

The nature and molecular receptors controlling cell-substrate adhesion in *Dictyostelium* are not fully identified [31] [113]. However, actin-rich structures often referred to as actin foci are localized in the adhesion regions of migrating cells [100] [46]. Our study revealed that pulling forces require formation of firm adhesion to the substrate co-localized with actin foci regions and are directly transmitted by the actin cytoskeleton [139]. In contrast, we did not observe actin foci in the regions where cells were generating compressive, normal forces on the substrate. Because the cell nucleus did not co-localize with these regions either, we concluded that the

compressive forces are transmitted directly by cytosolic pressure. We corroborated this hypothesis by estimating the cortical tension using our measurements of normal compressive cell-substrate forces, and a simple Young-Laplace's model that assumes that cortical tension is balanced by an increase in cytoplasmic pressure with respect to the extracellular medium. The cortical tensions estimated in this manner were found to be in good agreement with previously reported data measured by micropipette aspiration or cell poking for the cell lines considered in this study [124] [127] [126] [125].

Thus, our experiments indicate that amoeboid cells can exert strong compressive forces on their substrate by increasing their cytoplasmic pressure. We previously showed that in *Dictyostelium* cells whose F-actin polymerization at the front is impaired by lack of F-actin cross-linking (*abp120*$^{-}$), lateral squeezing generates the required pressure rise to propel their cytoplasmic material [30]. These results agree with studies showing motion driven by internal hydrostatic pressure in other amoeboid cells [151] and supports the hypothesis that hydrostatic pressure is one of the forces driving pseudopod extension during cell crawling [152]. Amoeboid cells migrating in three-dimensional matrices may use similar mechanisms to push off the surrounding obstacles without establishing specific cell-matrix adhesions[153] [154]. Cell malleability is recognized as an important factor in the migratory efficiency of amoeboid cells embedded in 3D matrices. Emerging studies suggest that leukocytes squeeze through small gaps in the extracellular matrix by actomyosin-regulated contractility without significant remodeling of the surrounding environment; however, the mechanistic details of this process are still not well understood [155]. Thus, the results of our study could contribute to a better understanding of cell migration, not only on flat surfaces, but also in more complex environments.

Chapter 3 has been in part published in *Biophysical Journal*, "Three-dimensional Balance of Cortical Tension and Axial Contractility Enables Fast Amoeboid Migration" by B. Álvarez-González, R. Meili, E. Bastounis, R. A. Firtel, J. C. Lasheras and J. C. del Álamo (2015), 108 (4), 821-832. The thesis author is the primary investigator in this publication.

# Chapter 4

# Three-dimensional force measurements improved by Lagrange multipliers optimization

## 4.1 Introduction

Traction Force Microscopy (TFM) is a powerful approach for quantifying the interactions between cells and their surroundings [72]. The results obtained though Fourier Traction Force Microscopy have some limitations. A shortcoming is that this method doesn't impose that the stress field in each of the three directions needs to be in equilibrium in order to satisfy the second law of Newton. The net force applied by an isolated cell to the substrate is known to be zero [156]. However, there are some spurious measurements of the stress field that usually result in a non-zero net force. This artifact can be taken into account to guarantee a zero net force applied by the cell on the substrate. Another limitation is that Fourier Traction Force Microscopy doesn't restrict the traction forces to be applied just in the area where the cell is located and it doesn't force the the traction forces outside the cell to be zero [33].

There are various solutions that have been used to solve these limitations. A simple

approach to address the first limitation is to subtract the mean value of the displacements to the entire displacement field, in this way the stress field is in equilibrium. But this solution requires subtracting a constant value to all the measurements and forces the equilibrium. To solve the second limitation, Butler et al. [33] developed an approach that consists of an iterative process. First, they measured the displacement field without any constraint. Second, they calculated the traction force field with no restrictions and set the tractions outside the cell equal to zero. Third, they calculated the displacement field induced by this new traction field. Fourth, they defined a new displacement field by replacing the displacements of the calculated displacement field within the cell boundaries by the experimentally measured displacement field and repeated these steps until convergence, which is reached at a tolerance level. A shortcoming of this methodology is that by doing this the traction force field obtained may not be compatible with the measured displacement field.

We propose a Lagrange multipliers method for the optimization of the displacement field obtained through the cross-correlation functions of the z-stack of images deformed by a migrating cell and the non-deformed z-stack of images used as reference. Besides, we imposed two constraints for the calculation of the deformation field at each point. The first constraint is the equilibrium of the displacements and the second restriction is that the traction forces must be equal to zero outside the cell. By optimizing the value of the cross-correlation function used to calculate the displacement field applied by the cell at each point, we are also taking into account the signal to noise ratio of each measurement of the deformation field when we apply the constrains.

Here, we present the theoretical formulation of an improved TFM method by applying a Lagrange Multipliers optimization. This method results in a constrained solution of the stresses exerted by migrating cells that are in equilibrium and applied only in the area where the cell is located. We show the results of the TFM method improved with Lagrange multipliers optimization for a representative *Dictyostelium discoideum* cell and compare them to the results obtained by using the unconstrained TFM.

## 4.2 Methodology and theory

The traction forces exerted by the cells when moving over elastic flat substrates can be calculated form the displacement field suffered by the beads embedded in the elastic substrate through an exact analytical solution, by solving the elasticity equation of equilibrium, as explained in chapter 2 section 2.10. We obtained the z-stack of images needed to perform the three-dimensional correlation by imaging a range of 9$\mu$m centered in the plane of the gel where the beads are in focus. To acquire all the information related to the deformation of the gel, we acquired a total of 24 planes, one every 0.4$\mu$m.

The displacement fields applied to the beads were measured by an image correlation method similar to Particle Image Velocimetry (PIV) [157][158]. This method is based on correlation techniques, we calculated the displacement field through the cross-correlation between two z-stacks of images one of the deformed substrate where the cell is applying forces and the other of the reference z-stack, in which the substrate is not deformed. We used interrogation windows of 24x24x24 pixels with an overlap of 12 pixels in the horizontal plane to increase the resolution. In order to increase the accuracy of the displacement estimation, we used the interpolation to obtain the maximum peak in the cross-correlation function with sub-pixel accuracy. The gaussian interpolation works for correlation peaks and it is standard in PIV processing [92][93]. We used a Gaussian regression by minimizing the norm of a three dimensional parabolic fit to the logarithmic values of the correlation function.

### 4.2.1 Sub-pixel interpolation through three-dimensional gaussian regression

The sub-pixel interpolation is done through a three dimensional gaussian regression. We consider a 3D gaussian function:

$$Z(x,y,z) = a\exp[b(x-\Delta x)^2 + c(y-\Delta y)^2 + d(z-\Delta z)^2 + e(x-\Delta x)(y-\Delta y) + \\ + f(x-\Delta x)(z-\Delta z) + g(y-\Delta y)(z-\Delta z)] \tag{4.1}$$

with maximum at $[\Delta x, \Delta y, \Delta z]$. This could also be written as:

$$Z(x,y,z) = \exp[A_1 + A_2 x + A_3 y + A_4 z + A_5 x^2 + A_6 y^2 + A_7 z^2 + A_8 xy + A_9 xz + A_{10} yz] \quad (4.2)$$

These 10 coefficients can be derived using a regression analysis. Therefore we need to minimize the norm of the logarithmic value of the following function :

$$L = \sum_{k=-n}^{n} \sum_{j=-n}^{n} \sum_{i=-n}^{n} [A_1 + A_2 i + A_3 j + A_4 k + A_5 i^2 + A_6 j^2 + A_7 k^2 + A_8 ij + A_9 ik + A_{10} jk + \quad (4.3)$$
$$- ln(Z(i,j,k))]^2$$

To obtain the coefficients $A_1$, $A_2$, ... , $A_{10}$, we need to minimize the norm of $L$. This is done by taking the partial derivatives of this function with respect to these 10 coefficients and making them equal to zero. It is necessary to take into account the summation when doing these derivatives. In this way we get the 10 coefficients as a function of $n$, which is the number of pixels around the maximum of the correlation function that we use to obtain the gaussian interpolation. The values of the coefficients obtained through this method, and that we use for the sub-pixel interpolation, are the following:

$$A_1 = \frac{[\sum_{k=-n}^{n} \sum_{j=-n}^{n} \sum_{i=-n}^{n} (19n^2 + 19n - 15i^2 - 15j^2 - 15k^2 - 3) ln(Z(i,j,k))]}{(8n^2 + 12n^2 + 6n + 1)(-3 + 4n + 4n^2)} \quad (4.4)$$

$$A_2 = \frac{3[\sum_{k=-n}^{n} \sum_{j=-n}^{n} \sum_{i=-n}^{n} i \cdot ln(Z(i,j,k))]}{n(7n + 1 + 18n^2 + 20n^3 + 8n^4)} \quad (4.5)$$

$$A_3 = \frac{3[\sum_{k=-n}^{n} \sum_{j=-n}^{n} \sum_{i=-n}^{n} j \cdot ln(Z(i,j,k))]}{n(7n + 1 + 18n^2 + 20n^3 + 8n^4)} \quad (4.6)$$

$$A_4 = \frac{3[\sum_{k=-n}^{n} \sum_{j=-n}^{n} \sum_{i=-n}^{n} k \cdot ln(Z(i,j,k))]}{n(7n + 1 + 18n^2 + 20n^3 + 8n^4)} \quad (4.7)$$

$$A_5 = \frac{[\sum_{k=-n}^{n}\sum_{j=-n}^{n}\sum_{i=-n}^{n}(-15(n^2+n-3i^2))ln(Z(i,j,k))]}{(-3+4n+4n^2)(8n^3+12n^2+6n+1)n(n+1)} \tag{4.8}$$

$$A_6 = \frac{[\sum_{k=-n}^{n}\sum_{j=-n}^{n}\sum_{i=-n}^{n}(-15(n^2+n-3j^2))ln(Z(i,j,k))]}{(-3+4n+4n^2)(8n^3+12n^2+6n+1)n(n+1)} \tag{4.9}$$

$$A_7 = \frac{[\sum_{k=-n}^{n}\sum_{j=-n}^{n}\sum_{i=-n}^{n}(-15(n^2+n-3k^2))ln(Z(i,j,k))]}{(-3+4n+4n^2)(8n^3+12n^2+6n+1)n(n+1)} \tag{4.10}$$

$$A_8 = \frac{9[\sum_{k=-n}^{n}\sum_{j=-n}^{n}\sum_{i=-n}^{n} j\cdot i\cdot ln(Z(i,j,k))]}{n^2(8n^5+28n^4+8n+1+25n^2+38n^3)} \tag{4.11}$$

$$A_9 = \frac{9[\sum_{k=-n}^{n}\sum_{j=-n}^{n}\sum_{i=-n}^{n} i\cdot k\cdot ln(Z(i,j,k))]}{n^2(8n^5+28n^4+8n+1+25n^2+38n^3)} \tag{4.12}$$

$$A_{10} = \frac{9[\sum_{k=-n}^{n}\sum_{j=-n}^{n}\sum_{i=-n}^{n} j\cdot k\cdot ln(Z(i,j,k))]}{n^2(8n^5+28n^4+8n+1+25n^2+38n^3)} \tag{4.13}$$

where $n$ is the number of pixels around the maximum of the correlation function that we used to obtain the gaussian interpolation.

### 4.2.2 Lagrange multipliers optimization for the calculation of the displacement field

The traction forces exerted by the cell when is moving over a flat substrate must be in static equilibrium, therefore the displacements measured with the PIV method need to satisfy this requirement. The constraint that we used to optimize the measurements of the PIV is that the displacement field in a box surrounding the cell must be in equilibrium. Since the image that we take with the microscope can contain more than one cell, in order impose this condition, we need to find the position of the particular cell, as shown in Figure 4.1A, and locate a box around the cell, which dimensions we choose to be 3 times the length of the cell. In this box where the cell is located, there are multiple boxes of 24x24x24 pixels (Figure 4.1B), in which the displacements are measured through the PIV method.

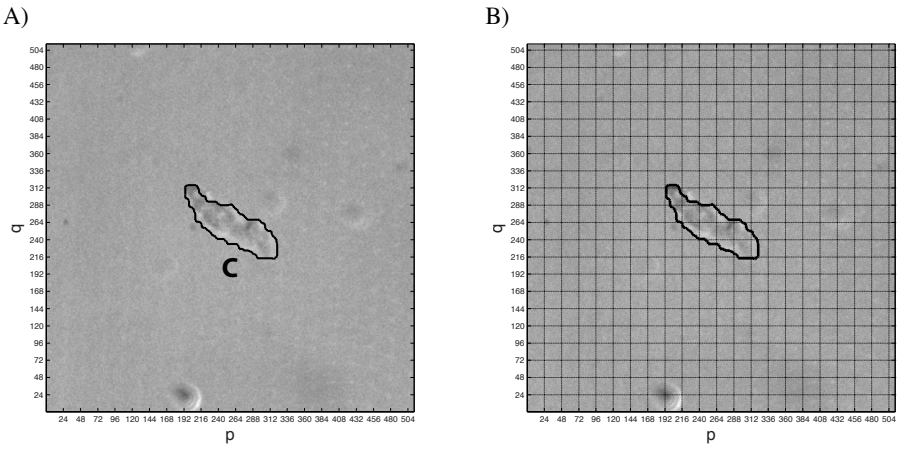


**Figure 4.1**: Detection of the cell's contour and distribution of the small boxes used for the calculation of the correlation functions that provide the displacement field at each point. A) Bright field image of the cell and detection of the contour needed to locate the area where the cell is. The box taken around the cell is chosen to be square with a size three times the length of the cell. B) The box surrounding the cell used for the calculation of the displacement field is divided in small boxes of 24x24 pixels. We calculate the displacement applied in each of these small boxes.

The cross-correlation function is calculated with the PIV method in each of the small boxes of 24x24x24 pixels, and it is obtained from the 10 coefficients that determine the gaussian fitting. Therefore, the functions that need to be maximized in the optimization problem are the correlation functions calculated for each of the small boxes. In this way, since we are maximizing the cross-correlation function of each window, the signal to noise ratio of the measurements is taken into account. The variation of the point used for determining the displacement field for the measurements with a high signal to noise ratio will affect more the value of the cross-correlation function maximum value. Consequently, with this method the points with higher values of the signal to noise ratio are going to be less affected than the ones with lower values. Therefore, the less accurate values of the displacement field are going to be more modified whereas the values that should be very accurate, since they have very high values of the signal to noise ratio for the correlation function would be slightly modified (Figure 4.2).

The constraints imposed to this optimization problem are the equilibrium of the displacement field in each of the three directions and zero traction forces outside the region in which the

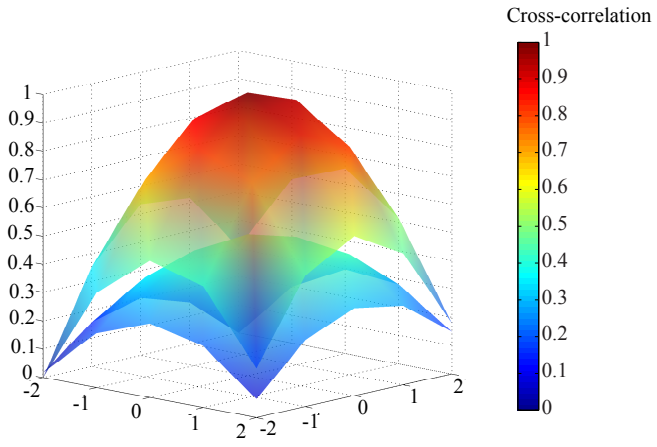


**Figure 4.2**: Comparison of a cross-correlation function for a sub-window in which the signal to noise ratio of the correlation is equal to 4.54 and for a sub-window in which the signal to noise ratio is equal to 2.43.

cell is located. Since the relationship between displacement field and stress field is linear, when the displacement field is in equilibrium the stress field is in equilibrium too. These constraints can be formulated as follows:

$$C_1 = \int_p \int_q u^{p,q} dxdy \tag{4.14}$$

$$C_2 = \int_p \int_q v^{p,q} dxdy \tag{4.15}$$

$$C_3 = \int_p \int_q w^{p,q} dxdy \tag{4.16}$$

$$\tau_{zx}\Big|_{\text{outside C}} = 0 \tag{4.17}$$

$$\tau_{zy}\Big|_{\text{outside C}} = 0 \tag{4.18}$$

$$\tau_{zz}\Big|_{\text{outside C}} = 0 \tag{4.19}$$

where $p$ and $q$ are meant for all the small boxes in which the box around the cell is divided when we perform the PIV method, in this case we used 24x24 pixels' windows and C indicates the contour of the cell.

The correlation function in each of the small boxes is given by equation 4.2. Therefore we need to maximize the value of this function in each of the small boxes subject to the imposed constraints. Applying a Lagrange multipliers optimization, the function that is maximized is the following:

$$\begin{aligned} L_i = {} & A_i + B_i + C_i u_i^2 + D_i v_i + E_i v_i^2 + F_i w_i + G_i w_i^2 + H_i u_i v_i + J_i u_i w_i + k_i v_i w_i + \\ & + \lambda_1 \sum_{j=1}^{N} u_j + \lambda_2 \sum_{j=1}^{N} v_j + \lambda_3 \sum_{j=1}^{N} w_j + \lambda_4 \tau_{x_1}(u_i, v_i, w_i) + \ldots + \lambda_{M+3} \tau_{x_M}(u_i, v_i, w_i) + \\ & + \lambda_{M+4} \tau_{y_1}(u_i, v_i, w_i) + \ldots + \lambda_{2M+3} \tau_{y_M}(u_i, v_i, w_i) + \ldots + \\ & + \lambda_{2M+4} \tau_{z_1}(u_i, v_i, w_i) + \ldots + \lambda_{3M+3} \tau_{z_M}(u_i, v_i, w_i) \end{aligned} \tag{4.20}$$

$L_i$ are the Lagrange functions and the constants $\lambda_1$, ..., $\lambda_{3M+3}$ are called Lagrange multipliers.

The values of the stresses at each point are calculated from the displacement field through the Green's function, $G$, which is given in closed analytical form by del Álamo et al. [43], as follows:

$$\tau_{x_j} = \sum_i G_{x_j u_i} u_i \Delta x + \sum_i G_{x_j v_i} v_i \Delta x + \sum_i G_{x_j w_i} w_i \Delta x \tag{4.21}$$

$$\tau_{y_j} = \sum_i G_{y_j u_i} u_i \Delta x + \sum_i G_{y_j v_i} v_i \Delta x + \sum_i G_{y_j w_i} w_i \Delta x \tag{4.22}$$

$$\tau_{z_j} = \sum_i G_{z_j u_i} u_i \Delta x + \sum_i G_{z_j v_i} v_i \Delta x + \sum_i G_{z_j w_i} w_i \Delta x \tag{4.23}$$

Therefore, being:

$$G_{x_1 u_i} = \frac{\partial \tau_{x_1}}{\partial u_i} \frac{1}{\Delta x^2} \tag{4.24}$$

$$G_{x_1 v_i} = \frac{\partial \tau_{x_1}}{\partial v_i} \frac{1}{\Delta x^2} \tag{4.25}$$

$$G_{x_1 w_i} = \frac{\partial \tau_{x_1}}{\partial w_i} \frac{1}{\Delta x^2} \tag{4.26}$$

The Lagrange multipliers optimization consists on equating the partial derivatives of $L_i$ with respect to $u_i$, $v_i$, $w_i$, $\lambda_1$, ..., $\lambda_{3M+3}$ to zero and solving the resulting system of equations. In this case, the system of equation that results from the Lagrange multipliers optimization can be written in a matrix form, as follows:

$$Px = q \tag{4.27}$$

Where $P$ is the following matrix:

$$P = \left[\begin{array}{c|c|c|c|c|c|c} C & H & J & I_1 & Gxu & Gyu & Gzu \\ \hline H & E & K & I_2 & Gxv & Gyv & Gzv \\ \hline J & K & G & I_3 & Gxw & Gyw & Gzw \\ \hline I_1^T & I_2^T & I_3^T & 0 & 0 & 0 & 0 \\ \hline Gxu^T & Gxv^T & Gxw^T & 0 & 0 & 0 & 0 \\ \hline Gyu^T & Gyv^T & Gyw^T & 0 & 0 & 0 & 0 \\ \hline Gzu^T & Gzv^T & Gzw^T & 0 & 0 & 0 & 0 \end{array}\right] \tag{4.28}$$

Where:

$$C = \begin{bmatrix} 2C_1 & 0 & \cdots & 0 \\ 0 & 2C_2 & \ddots & 0 \\ \vdots & \ddots & \ddots & \vdots \\ 0 & \cdots & 0 & 2C_N \end{bmatrix} \tag{4.29}$$

$$H = \begin{bmatrix} H_1 & 0 & \cdots & 0 \\ 0 & H_2 & \ddots & 0 \\ \vdots & \ddots & \ddots & \vdots \\ 0 & \cdots & 0 & H_N \end{bmatrix} \tag{4.30}$$

$$J = \begin{bmatrix} J_1 & 0 & \cdots & 0 \\ 0 & J_2 & \ddots & 0 \\ \vdots & \ddots & \ddots & \vdots \\ 0 & \cdots & 0 & J_N \end{bmatrix} \tag{4.31}$$

$$E = \begin{bmatrix} 2E_1 & 0 & \cdots & 0 \\ 0 & 2E_2 & \ddots & 0 \\ \vdots & \ddots & \ddots & \vdots \\ 0 & \cdots & 0 & 2E_N \end{bmatrix} \tag{4.32}$$

$$K = \begin{bmatrix} K_1 & 0 & \cdots & 0 \\ 0 & k_2 & \ddots & 0 \\ \vdots & \ddots & \ddots & \vdots \\ 0 & \cdots & 0 & k_N \end{bmatrix} \tag{4.33}$$

$$G = \begin{bmatrix} 2G_1 & 0 & \cdots & 0 \\ 0 & 2G_2 & \ddots & 0 \\ \vdots & \ddots & \ddots & \vdots \\ 0 & \cdots & 0 & 2G_N \end{bmatrix} \tag{4.34}$$

$$I1 = \begin{bmatrix} 1 & 0 & 0 \\ 1 & 0 & 0 \\ \vdots & \vdots & \vdots \\ 1 & 0 & 0 \end{bmatrix} \tag{4.35}$$

$$I2 = \begin{bmatrix} & & \\ 0 & 1 & 0 \\ & & \\ 0 & 1 & 0 \\ & & \\ \vdots & \vdots & \vdots \\ & & \\ 0 & 1 & 0 \\ & & \end{bmatrix} \tag{4.36}$$

$$I3 = \begin{bmatrix} & & \\ 0 & 0 & 1 \\ & & \\ 0 & 0 & 1 \\ & & \\ \vdots & \vdots & \vdots \\ & & \\ 0 & 0 & 1 \\ & & \end{bmatrix} \tag{4.37}$$

$$Gxu = \begin{bmatrix} G_{x_1u_1} & G_{x_2u_1} & \cdots & G_{x_Mu_1} \\ G_{x_1u_2} & G_{x_2u_2} & \cdots & G_{x_Mu_2} \\ \vdots & \vdots & \vdots & \vdots \\ G_{x_1u_N} & G_{x_2u_N} & \cdots & G_{x_Mu_N} \end{bmatrix} \tag{4.38}$$

$$Gyu = \begin{bmatrix} G_{y_1u_1} & G_{y_2u_1} & \cdots & G_{y_Mu_1} \\ G_{y_1u_2} & G_{y_2u_2} & \cdots & G_{y_Mu_2} \\ \vdots & \vdots & \vdots & \vdots \\ G_{y_1u_N} & G_{y_2u_N} & \cdots & G_{y_Mu_N} \end{bmatrix} \tag{4.39}$$

$$Gzu = \begin{bmatrix} G_{z_1u_1} & G_{z_2u_1} & \cdots & G_{z_Mu_1} \\ G_{z_1u_2} & G_{z_2u_2} & \cdots & G_{z_Mu_2} \\ \vdots & \vdots & \vdots & \vdots \\ G_{z_1u_N} & G_{z_2u_N} & \cdots & G_{z_Mu_N} \end{bmatrix} \tag{4.40}$$

$$Gxv = \begin{bmatrix} G_{x_1v_1} & G_{x_2v_1} & \cdots & G_{x_Mv_1} \\ G_{x_1v_2} & G_{x_2v_2} & \cdots & G_{x_Mv_2} \\ \vdots & \vdots & \vdots & \vdots \\ G_{x_1v_N} & G_{x_2v_N} & \cdots & G_{x_Mv_N} \end{bmatrix} \tag{4.41}$$

$$Gyv = \begin{bmatrix} G_{y_1v_1} & G_{y_2v_1} & \cdots & G_{y_Mv_1} \\ G_{y_1v_2} & G_{y_2v_2} & \cdots & G_{y_Mv_2} \\ \vdots & \vdots & \vdots & \vdots \\ G_{y_1v_N} & G_{y_2v_N} & \cdots & G_{y_Mv_N} \end{bmatrix} \tag{4.42}$$

$$Gzv = \begin{bmatrix} G_{z_1v_1} & G_{z_2v_1} & \cdots & G_{z_Mv_1} \\ G_{z_1v_2} & G_{z_2v_2} & \cdots & G_{z_Mv_2} \\ \vdots & \vdots & \vdots & \vdots \\ G_{z_1v_N} & G_{z_2v_N} & \cdots & G_{z_Mv_N} \end{bmatrix} \tag{4.43}$$

$$Gxw = \begin{bmatrix} G_{x_1w_1} & G_{x_2w_1} & \cdots & G_{x_Mw_1} \\ G_{x_1w_2} & G_{x_2w_2} & \cdots & G_{x_Mw_2} \\ \vdots & \vdots & \vdots & \vdots \\ G_{x_1w_N} & G_{x_2w_N} & \cdots & G_{x_Mw_N} \end{bmatrix} \tag{4.44}$$

$$Gyw = \begin{bmatrix} G_{y_1w_1} & G_{y_2w_1} & \cdots & G_{y_Mw_1} \\ G_{y_1w_2} & G_{y_2w_2} & \cdots & G_{y_Mw_2} \\ \vdots & \vdots & \vdots & \vdots \\ G_{y_1w_N} & G_{y_2w_N} & \cdots & G_{y_Mw_N} \end{bmatrix} \tag{4.45}$$

$$Gzw = \begin{bmatrix} G_{z_1w_1} & G_{z_2w_1} & \cdots & G_{z_Mw_1} \\ G_{z_1w_2} & G_{z_2w_2} & \cdots & G_{z_Mw_2} \\ \vdots & \vdots & \vdots & \vdots \\ G_{z_1w_N} & G_{z_2w_N} & \cdots & G_{z_Mw_N} \end{bmatrix} \tag{4.46}$$

The vector $x$ is:

$$x = \begin{bmatrix} d \\ \hdashline \lambda \end{bmatrix} \tag{4.47}$$

where:

$$d = \begin{bmatrix} u_1 \\ u_2 \\ \vdots \\ u_N \\ - - - \\ v_1 \\ v_2 \\ \vdots \\ v_N \\ - - - \\ w_1 \\ w_2 \\ \vdots \\ w_N \end{bmatrix} \tag{4.48}$$

$$\lambda = \begin{bmatrix} \\ \lambda_1 \\ \\ \lambda_2 \\ \\ \lambda_3 \\ \text{- - - - -} \\ \lambda_4 \\ \\ \vdots \\ \\ \lambda_{M+3} \\ \text{- - - - -} \\ \lambda_{M+4} \\ \\ \vdots \\ \\ \lambda_{2M+3} \\ \text{- - - - -} \\ \lambda_{2M+4} \\ \\ \vdots \\ \\ \lambda_{3M+3} \end{bmatrix} \tag{4.49}$$

And the vector $q$ is:

$$q = \left[\begin{array}{c} \\ -B_1 \\ \\ \vdots \\ \\ -B_N \\ \hdashline \\ -D_1 \\ \\ \vdots \\ \\ -D_N \\ \hdashline \\ -F_1 \\ \\ \vdots \\ \\ -F_N \\ \hdashline \\ 0 \\ \\ \vdots \\ \\ 0 \end{array}\right] \tag{4.50}$$

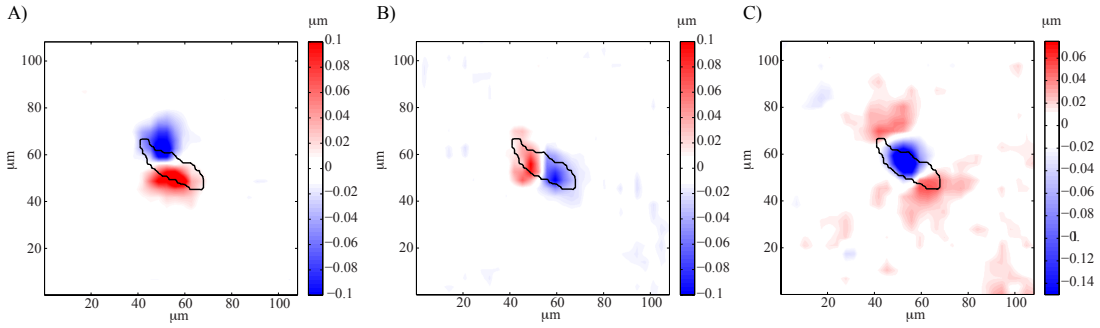


**Figure 4.3**: Displacement field applied by a representative *Dictyostelium* cell obtained through the unconstrained PIV technique. A) Displacement field applied by the cell in the plane of the substratum in the x-direction (direction of the major axis of the cell) obtained through the unconstrained PIV technique. B) Displacement field applied by the cell in the plane of the substratum in the y-direction (perpendicular direction to the major axis of the cell) obtained through the unconstrained PIV technique. C) Displacement field applied by the cell in the z-direction, direction perpendicular to the plane of the substratum, obtained through the unconstrained PIV technique.

## 4.3 Results

### 4.3.1 Three-dimensional forces exerted by migrating amoeboid cells calculated by constrained 3DTFM improved by Lagrange multipliers optimization

When we applied the Lagrange multipliers optimization explained in section 4.2.2 to the correlation functions computed through the PIV method, we obtained a new displacement field that satisfies the required constraints. We calculated the displacements field exerted by a *Dictyostelium discoideum* cell in the three directions by using the PIV technique and the Lagrange multipliers optimization method explained in section 4.2.2. Figure 4.3 shows the displacement field obtained by applying the unconstrained PIV method and Figure 4.4 shows the displacement field obtained through the constrained method by applying Lagrange multipliers optimization.

The traction forces were obtained in both cases by multiplying the correspondent displacement field with the Green's function, $G$, that was given in closed analytical form by del Álamo et al. [43]. Figure 4.5 shows the traction forces in the three-dimensions obtained by using the unconstrained 3DTFM method explained in section 2.10. The forces obtained for the same cell and instant of time through constrained 3DTFM improved by the Lagrange multipliers

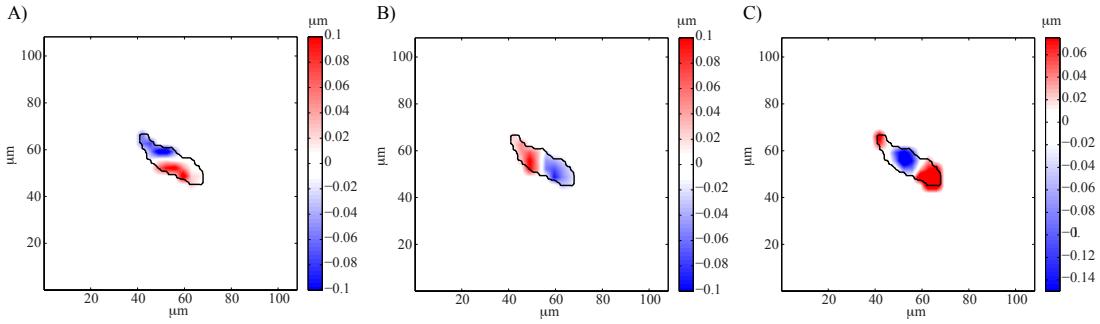


**Figure 4.4**: Displacement field applied by a representative *Dictyostelium* cell obtained through the constrained Lagrange multipliers optimization method. A) Displacement field applied by the cell in the plane of the substratum in the x-direction (direction of the major axis of the cell) obtained through the constrained Lagrange multipliers optimization method. B) Displacement field applied by the cell in the plane of the substratum in the y-direction (perpendicular direction to the major axis of the cell) obtained through the constrained Lagrange multipliers optimization method. C) Displacement field applied by the cell in the z-direction, direction perpendicular to the plane of the substratum, obtained through the constrained Lagrange multipliers optimization method.

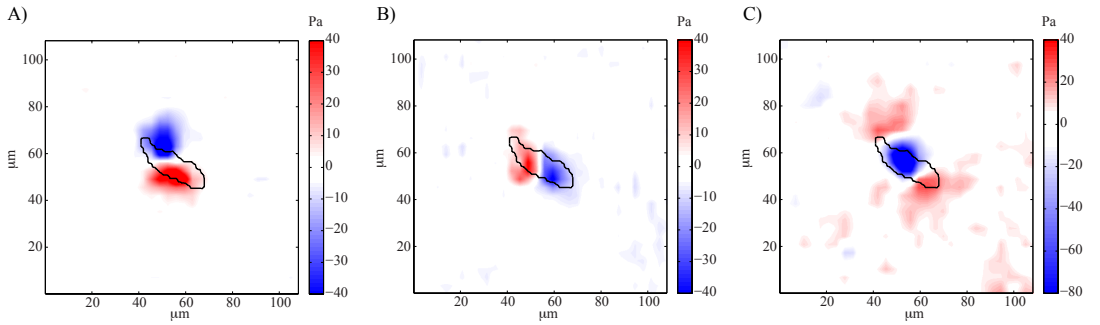


**Figure 4.5**: Stress field exerted by a representative *Dictyostelium* cell obtained by unconstrained 3DTFM. A) Stresses exerted by the cell in the plane of the substratum in direction of the major axis of the cell, $\tau_{zx}$, obtained by unconstrained 3DTFM. B) Stresses exerted by the cell in the plane of the substratum in the perpendicular direction to the major axis of the cell, $\tau_{zy}$, obtained by unconstrained 3DTFM. C) Stresses exerted by the cell in the plane perpendicular to the substratum, $\tau_{zz}$, obtained by unconstrained 3DTFM.

optimization are shown in Figure 4.6. When we used the 3DTFM method, the results show stresses applied in a region that is outside the contour of the cell. On the contrary, when we used 3DTFM improved by Lagrange multipliers optimization, the forces are confined in the region where the cell is located.

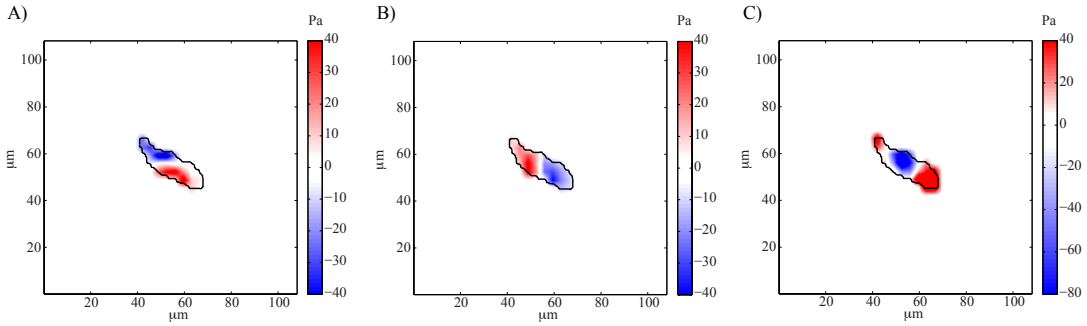


**Figure 4.6**: Stress field exerted by a representative *Dictyostelium* cell obtained by Lagrange multipliers optimization improved 3DTFM. A) Stresses exerted by the cell in the plane of the substratum in direction of the major axis of the cell, $\tau_{zx}$, obtained by Lagrange multipliers optimization improved 3DTFM. B) Stresses exerted by the cell in the plane of the substratum in the perpendicular direction to the major axis of the cell, $\tau_{zy}$, obtained by Lagrange multipliers optimization improved 3DTFM. C) Stresses exerted by the cell in the plane perpendicular to the substratum, $\tau_{zz}$, obtained by Lagrange multipliers optimization improved 3DTFM.

### 4.3.2 Comparison of the results obtained by unconstrained and constrained 3DTFM

To compare the results obtained by 3DTFM and by the new method improved by Lagrange multipliers optimization, we quantified the percentage of unbalance that we measured in the instantaneous stress field exerted in the three-dimensions by the representative *Dictyostelium* cell shown in Figures 4.3 - 4.6. We showed that we measured equilibrium of the forces when we used the constrained 3DTFM method, contrary to the case in which we used the unconstrained 3DTFM. We defined the relative unbalanced as follows:

$$\%\ \text{unbalanced in}\ \tau_{zx} = \left| \frac{\int_A \tau_{zx} dA}{\int_A |\tau_{zx}| dA} \right| \cdot 100 \tag{4.51}$$

$$\%\ \text{unbalanced in}\ \tau_{zy} = \left| \frac{\int_A \tau_{zy} dA}{\int_A |\tau_{zy}| dA} \right| \cdot 100 \tag{4.52}$$

$$\%\ \text{unbalanced in}\ \tau_{zz} = \left| \frac{\int_A \tau_{zz} dA}{\int_A |\tau_{zz}| dA} \right| \cdot 100 \tag{4.53}$$

We found fairly unbalance in the measurements of the stresses obtained using the 3DTFM

method without any constraint, whereas the unbalanced is negligible ($\sim 0$) when we applied the Lagrange multipliers optimization. Table 4.1 shows the unbalance of the force measurements that we calculated for this cell with the two methods, when Lagrange multipliers optimization is applied and when is not. The comparison of these results indicates that the Lagrange multipliers optimization corrects the existent unbalance.

**Table 4.1**: Percentage of unbalance in the stresses in the three-directions when using unconstrained 3DTFM and when using 3DTFM improved by Lagrange multipliers optimization. The table lists the percentage of unbalance of the forces measured in the three-dimensions ($\tau_{zx}, \tau_{zy}, \tau_{zz}$), when using the unconstrained and constrained 3DTFM. The percentage of unbalance is significant when using unconstrained 3DTFM, but it is negligible when applying the constrained 3DTFM improved by Lagrange multipliers optimization.

| % unbalance | Unconstrained 3DTFM | Constrained 3DTFM |
|---|---|---|
| $\tau_{zx}$ | 23.17 | 0.0017 |
| $\tau_{zy}$ | 69.53 | 0.0002 |
| $\tau_{zz}$ | 6.79 | 0.0021 |

The strain energy deposited by the cell on the substratum is equal to the mechanical work exerted by the cell. The total strain energy applied by a cell is defined as follows:

$$U_s = \frac{1}{2}\int_0^L \int_0^W (\tau_{zx}(x,y,h)\cdot u(x,y,h) + \tau_{zy}(x,y,h)\cdot v(x,y,h) + \tau_{zz}(x,y,h)\cdot w(x,y,h))dxdy \quad (4.54)$$

The values of the strain energy when using unconstrained and constrained 3DTFM are listed in Table 4.2. The value of the strain energy is quite different, the strain energy is quadratic with the stresses and displacements and integrated through the area. In the case of the 3DTFM improved by Lagrange multipliers optimization, the area in which there are stresses and displacements is much smaller than when using 3DTFM.

**Table 4.2**: Total strain energy when using unconstrained and constrained 3DTFM. The table lists the total stain energy ($U_s$), when using the unconstrained 3DTFM method and when using the constrained 3DTFM improved by Lagrange multipliers optimization.

| Strain energy | Unconstrained 3DTFM | Constrained 3DTFM |
|---|---|---|
| $U_s$ | 0.95 | 0.43 |

## 4.4 Discussion

The stresses exerted by a cell determine the deformation that it applies on the substratum. We calculate the forces applied by the cells from the displacement field measured experimentally, which is called the inverse problem [159]. We solved this problem by solving the elastic equation of equilibrium by using Fourier series [43].

There are several methods for the calculation of the stresses exerted by migrating cells, most of them are based on measurements of the deformation of a flat elastic substrate on which the cells crawl, and the subsequent calculation of the traction forces from the measured deformation [80][33][81]. But these methods are not ensuring that the stresses are in equilibrium or that stresses do not appear in the regions outside the cell contour. Our novel approach to calculate the stresses exerted by the cells is more consistent with the physics behind the problem.

We propose a constrained 3DTFM method improved by Lagrange multipliers optimization, that maximizes the values of the correlation functions that provide the displacements applied at each point of the substratum subject to two constraints, in this way we are obtaining results that are consistent with the measurements obtained from the experiments. The first constraint is the equilibrium of the displacement field and therefore the stress field, and the second one is that the stresses need to be applied in the area in which the cell is located and not outside. Therefore the results are compatible with the physics of the problem and they also account for the experimental measurements.

The noise that can appear in the forces calculated with the 3DTFM method is due only to the noise that appear in the estimation of the displacement field from the images used for their calculation. Therefore, the only possible source of inaccuracy that can be accounted is the calculation of the displacement field through the PIV technique. Consequently, we are improving these measurements with our new methodology.

There are advantages and disadvantages for the 3DTFM method and for this new 3DTFM improved by the Lagrange multipliers optimization. An advantage of the unconstraint Fourier Traction Force method is that it gives the forces that are measured from the displacement field by

using the exact analytical solution of the elastic equation of equilibrium, without imposing any constraint. Therefore, in this way the forces that are measured are not affected by any imposed restriction. Another advantage of the unconstrained 3DTFM method is that all the observed data are used.

On the other hand, the advantages of the 3DTFM improved by the Lagrange multipliers optimization, are that the stresses are in equilibrium and only applied in the region where the cell is located. This means that this constraint method results in measurements that are physically more reasonable, since it ensures that the forces are zero in the regions outside the cell and also that there is not a net force applied. Single cells are in static equilibrium and the existence of a net force is due to the unbalanced in the forces attributable merely to errors in the measurement of the displacement field.

Chapter 4 is currently being prepared for publication, “Cellular Traction Forces Quantification Improved by Lagrange Multipliers Optimization” by B. Álvarez-Gonzálezand, R. A. Firtel, J. C. Lasheras and J. C. del Álamo. The thesis author is the primary investigator in this publication.

# Chapter 5

# Novel elastometric microscopy to characterize the extracellular matrix

## 5.1 Introduction

The mechanical properties of the substratum affect cellular behavior and processes such as locomotion, proliferation, growth, differentiation and spreading [160][161][162]. Cells can feel the properties of the extracellular environment and regulate adhesion by a process called mechanosensing [163][164][165]. An accurate calculation of the properties of materials used as extracellular matrix in real time is essential to study the influence of the environment characteristics in the behavior of cells. Therefore methods for the quantification of these properties will contribute to a better understanding of the relationship between cells and their environment.

There is a great interest in unravelling cellular mechanics. Increase attention is being paid to understand the way cells exert forces in the extracellular matrix (ECM) and their relationship with adhesion and migration [8]. Therefore, many methods have been developed for the measurement of the forces that cells exert on their ECM when moving, both in two and three dimensions [80][33][105][90]. Most of the methods for measuring traction forces use elastic materials [33][41]. Polyacrylamide is an extensively used material in Traction Force Microscopy

(TFM) [81][42][106], due to its elastic properties [166][167][160]. A precise characterization of the elastic properties of these substrates is essential for the accurate calculation of the traction forces that cells exert. There is a strong dependence on the calculation of the traction forces on the value of the Poisson ratio of the substratum, especially in the forces exerted in the perpendicular direction to the substratum [43]. An accurate method to characterize its value would guarantee more reliable results.

Polyacrylamide gels exhibit linear elasticity even for 15-25% strains [88][167], these values are larger than the ones generated typically by cells. The elastic behavior of polyacrylamide gels is kept in TFM experiments and the constitutive equations for linear elasticity are satisfied as long as the Young modulus has a proper value so the strain exerted on the gel is lower than 25%. The constitutive equations for linear elasticity depend only on two parameters: the Young modulus and the Poisson ratio [168]. Since the magnitude of the forces is proportional to the value of the Young modulus of the substratum, a lot of effort has been made to characterize it and there are established methods for its measurement [167]. On the contrary, there are not many studies on the characterization of the Poisson ratio. Flexible polymer hydrogels have been shown to exhibit a value for the Poisson ratio lower than 0.5, but there is a wide range of values that can be found in the literature varying from 0.27 to 0.49 [94][95][96]. It has also been suggested that this value depends on the specific composition of the gel [95][94].

We propose a new elastometry method to measure the elastic properties of polymer-based flexible substrates used in cell culture studies. Our method is suitable for measuring the elasticity of gel substrates in situ, which poses a big advantage with respect to previous methods. Existent procedures don't allow measuring the Poisson ratio and performing TFM experiments in the same gel [169][95]. On the contrary, our new methodology enables the simultaneous calculation of the Poisson ratio of the gel and the traction forces that a cell is exerting when moving over it. Polyacrylamide gels are not homogeneous [170][171], which suggests the requirement of a method that allows the characterization of their properties in real time. In this regard, our method enables calculating the Poisson ratio at each specific location of the gel in which a cell is moving, and therefore it can be calculated for the time point and location in which the traction

forces, tensions or other factors related to the extracellular matrix properties are measured in an experiment.

This novel elastometry method is based on the exact solution to the elastic equation of equilibrium, the measurement of the deformation exerted by cells when moving over an elastic substrate and the application of an iterative optimization algorithm for solving a non-linear least-squares problem. It is based on an extended procedure from the one used extensively in Fourier Traction Force Microscopy, with a novel application as Elastometric Microscopy. For the first time, the same principles used in TFM are used for calculating the properties of the materials used as ECM for cells. We used synthetic displacement fields to asses the performance of our new elastometry method. The results of the simulations show very accurate results for the values of the Poisson ratio. We also apply our method for the calculation of the Poisson ratio of polyacrylamide gels in real time, by measuring the deformations applied by *Physarum* cells moving over these substrates. Our method could be extended for the calculation of the parameters in the constitutive equations of other ECM based on more physiologically relevant materials, such as collagen. This new methodology opens a wide range of possibilities in the study of cell migration mechanics. The possibility of real time quantification of the ECM properties could elucidate the mechanism behind processes, such as the alterations in the ECM properties when tumorgenic cells are present.

## 5.2 Materials and Methods

### 5.2.1 Physarum cell culture

We grew a culture of *Physarum polycephalum* in agarose plates with oatmeal [172][173]. We took small pieces of this culture, and grew small pieces of *Physarum polycephalum* on agarose plates without oatmeal during 10 hours, to obtain a more motile amoeboid cell movement free of bacteria. From this culture, we cut pieces of approximately 200$\mu$m, which are in the amoeboid form (motile stage) [174], with a scalpel and placed them over the polyacrylamide gel. We removed the surrounding water by using a small glass capillary. We made an agar cap for

preventing the polyacrylamide gel from drying. To fabricate the agar cap we boiled a 100mM agar solution and put 100$\mu$l of this solution onto a glass coverslip mounted with a washer of 12mm diameter. When the agar cap was solidified, we placed it on top of the polyacrylamide gel over which the *Physarum* amoebae were located.

### 5.2.2 Substrate fabrication

We fabricated 12mm diameter, polyacrylamide gels of 5% acrylamide and 0.225% bisacrylamide (Young modulus approximately 8000 Pa [89]) mounted on 12-mm square # 1 glass coverslips [87][88]. In order to measure accurate displacement fields in the surface of the gel and in a plane below the surface, we fabricated the polyacrylamide gel as four adjacent layers with the bottom one containing no beads, a second layer containing 0.07% carboxylate modified yellow latex beads of 0.5$\mu$m diameter (Fluospheres, Invitrogen, Carlsbad CA), a third layer containing no beads, and the fourth one in the surface of the gel containing 0.07% carboxylate modified red latex beads of 0.5$\mu$m diameter (Fluospheres, Invitrogen, Carlsbad CA). The layers were verified to adhere well to each other under experimental conditions by confirming continuous registration of two layers using gels with beads of a second color in the bottom layer [43]. We mounted the coverslips with the gels in Petri dishes with a circular opening in the bottom using silicon grease (Dow Corning, Midland, Michigan). We made the gels physiologically compatible by cross-linking collagen I to the surface of the polyacrylamide. We used 1mM Sulfo-SANPAH (Thermo Sci, Rockford, Il) after UV activation to cross-link 0.25mg/ml collagen I. The gels were incubated overnight at room temperature. After washing, the gels were stored in HEPES buffer and antibiotic (40$\mu$M Ampicillin) for up to a week. The thickness of the gels was around 100$\mu$m and the distance between the two layers containing beads was around 15$\mu$m. We measured the exact substrate thickness and the distance between the layers congaing beads for each gel. The thickness was measured by locating the top and bottom planes of the gel and subtracting their z-positions and in a similar way the distance between the two layers containing beads was measured by locating and subtracting their z-positions. Figure 5.1 shows a sketch of the experimental configuration and Figure 5.2 shows a reconstruction of a z-stack of images taken

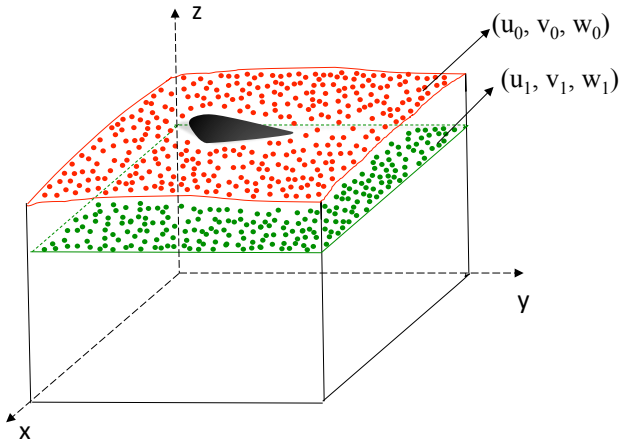


**Figure 5.1**: Sketch of the configuration of the experiment. Substrate with a layer embedded with red beads at the surface and with another layer embedded with green beads in a plane below the surface. A cell moves over the substrate and the deformation that it applies in both layers embedded with beads is measured.

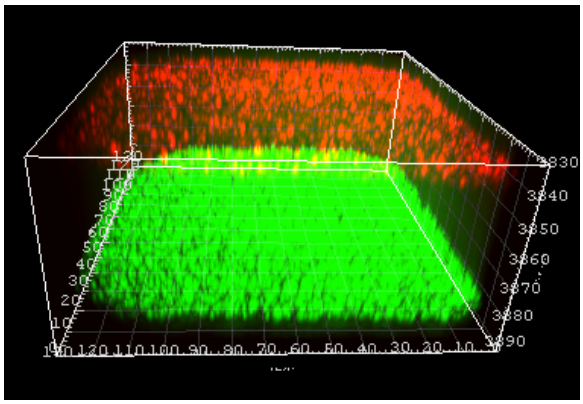

**Figure 5.2**: Three-dimensional image of a substratum with two layers of beads in two different planes. Reconstruction of a z-stack of images taken with a confocal microscope of a substratum with the surface plane embedded with red beads and a plane located below the surface embedded with green beads.

with a confocal microscope for this type of substratum.

### 5.2.3 Microscopy

The three-dimensional deformation in two different planes of the substrate was calculated form the displacements of the fluorescents beads embedded in each plane. We acquired time-lapse sequences consisting on z-stacks of images using a Leica DMI6000 B inverted microscope (Leica

Microsystems, Inc., Buffalo Grove, IL) equipped with a high speed Zyla 4.2 sCMOS camera (Andor Technology Ltd., Belfast, UK) and a 20x objective lens. The imaging setup was controlled by the open source microscopy software Micro-Manager [175][176][177]. To determine the displacement field in the surface plane, we acquired a z-stack of images consisting on 20 planes of fluorescent images obtained with a red laser. The middle plane of the z-stacks was located in the plane of maximum intensity of the beads using the autofocus system. The vertical distance between planes was 0.5 $\mu$m. To determine the displacement field in the plane below the surface, we acquired a z-stack of images consisting on 20 planes of fluorescent images obtained with a green laser. The middle plane of the z-stacks was located in the plane of maximum intensity using the autofocus system. The vertical distance between planes was 0.5 $\mu$m. The position and shape of the cell at each instant of time was recorded with an additional bright-field phase contrast image. We acquired the z-stacks containing the fluorescent images of the beads in the red and green channels and the phase-contrast image of the cell every 60 seconds.

### 5.2.4 Measurement of the substratum deformation

The z-stacks of images acquired enabled the calculation of the deformation exerted by the cell in each of the two planes of the substratum embedded with beads. We calculated the three-dimensional deformation in each of the two planes by cross-correlating each instantaneous z-stack of images in which the substratum is deformed and a non-deformed z-stack used as reference. In each experiment, the reference z-stack was obtained after the cell moved out of the field of view. The instantaneous and reference z-stacks were divided into smaller three-dimensional interrogation boxes of size 64x64x20 pixels in the x, y and z directions, to balance resolution and signal-to-noise while minimizing phototoxic effects. Therefore we measured the three components of the displacement field on the surface of the substrate (z=h) and on a plane a certain distance below the surface (z=$h_1$). The displacement fields at z=h, $\mathbf{u^h}$, are used as boundary conditions for solving analytically the elasticity equation of equilibrium, and calculating the deformation field in the whole substratum.

### 5.2.5 Method for the determination of the Poisson ratio

A force exerted on the surface of an elastic substrate produces a deformation. This deformation decays with the distance to the region where the force is applied. Cells placed on an elastic flat substrate exert three-dimensional forces that result on a three-dimensional deformation field inside the substrate where they move.

Solving the elasticity equation of equilibrium for a linear, homogeneous, isotropic material characterized by its Poisson ratio, $\sigma$, gives the strain and stress tensors everywhere in the substrate [43]. Therefore the displacement fields for all the z-positions in the substrate produced by a stress exerted in the surface can be calculated by solving the elasticity equation of equilibrium:

$$(1-2\sigma)\nabla^2\mathbf{u}+\nabla(\nabla\cdot\mathbf{u})=0 \tag{5.1}$$

The boundary conditions are zero displacements, $\mathbf{u}=\mathbf{0}$, at the bottom of the gel and the measured displacement field, $\mathbf{u}=\mathbf{u^h}$, at the surface of the gel. The inertial stresses can be neglected, since the ratio between the inertial and the elastic stresses is very small ($\sim 10^{-12}$). We solve the elasticity equation of equilibrium, eq. 5.1, by using Fourier series.

$$\mathbf{u}=\sum_{\alpha=-\infty}^{\infty}\sum_{\beta=-\infty}^{\infty}\hat{\mathbf{u}}_{\alpha\beta}exp(i\alpha x)exp(i\beta y) \tag{5.2}$$

Following the methodology shown in del Álamo et al. [43], we calculate the Fourier transform of the deformation field as:

$$\hat{\mathbf{u}}_{\alpha\beta}(z)=\left[\mathbf{U}_{\alpha\beta}(z)|\mathbf{V}_{\alpha\beta}(z)|\mathbf{W}_{\alpha\beta}(z)\right]=U_{\alpha\beta}(z)d_z\hat{\mathbf{u}}^{\mathbf{0}}_{\alpha\beta} \tag{5.3}$$

where $\mathbf{U}_{\alpha\beta}$, $\mathbf{V}_{\alpha\beta}$, $\mathbf{W}_{\alpha\beta}$ are three fundamental solutions of the problem, and $U_{\alpha\beta}(z)$ is the resolvant matrix. The vector $d_z\hat{\mathbf{u}}^{\mathbf{0}}_{\alpha\beta}$ contains the z-derivatives of the displacements Fourier coefficients at z=0, which are unknown, but can be related to the measured displacements in the surface as

follows from inverting eq. 5.3:

$$d_z\hat{\mathbf{u}}^{\mathbf{0}}_{\alpha\beta} = {U_{\alpha\beta}}^{-1}(z)\hat{\mathbf{u}}_{\alpha\beta}(z) \tag{5.4}$$

particularizing at z=h, we can calculate $d_z\hat{\mathbf{u}}^{\mathbf{0}}_{\alpha\beta}$ from the measured displacement fields in the surface of the substrate:

$$d_z\hat{\mathbf{u}}^{\mathbf{0}}_{\alpha\beta} = {U_{\alpha\beta}}^{-1}(h)\hat{\mathbf{u}}_{\alpha\beta}(h) \tag{5.5}$$

Therefore the Fourier coefficients of the measured displacements at z=h, $\hat{\mathbf{u}}_{\alpha\beta}(h)$, can be determined from combining eq. 5.2 and eq. 5.3 particularized at z=h:

$$\hat{\mathbf{u}}_{\alpha\beta}(z) = U_{\alpha\beta}(z){U_{\alpha\beta}}^{-1}(h)\hat{\mathbf{u}}_{\alpha\beta}(h) \tag{5.6}$$

The matrix $U_{\alpha\beta} = [\mathbf{U}_{\alpha\beta}(z)|\mathbf{V}_{\alpha\beta}(z)|\mathbf{W}_{\alpha\beta}]$ is the following:

$$\mathbf{U}_{\alpha\beta}(z) = \begin{bmatrix} \frac{\alpha^2 z cosh[(\alpha^2+\beta^2)^{1/2}z]}{4(\alpha^2+\beta^2)(1-\sigma)} + \frac{[4(1-\sigma)(\alpha^2+\beta^2)-\alpha^2]sinh[(\alpha^2+\beta^2)^{1/2}z]}{4(\alpha^2+\beta^2)^{3/2}(1-\sigma)} \\ \\ \frac{\alpha\beta z cosh[(\alpha^2+\beta^2)^{1/2}z]}{4(\alpha^2+\beta^2)(1-\sigma)} - \frac{\alpha\beta sinh[(\alpha^2+\beta^2)^{1/2}z]}{4(\alpha^2+\beta^2)^{3/2}(1-\sigma)} \\ \\ \frac{-i\alpha z sinh[(\alpha^2+\beta^2)^{1/2}z]}{4(\alpha^2+\beta^2)^{1/2}(1-\sigma)} \end{bmatrix} \tag{5.7}$$

$$\mathbf{V}_{\alpha\beta}(z) = \begin{bmatrix} \frac{\alpha\beta z cosh[(\alpha^2+\beta^2)^{1/2}z]}{4(\alpha^2+\beta^2)(1-\sigma)} - \frac{\alpha\beta sinh[(\alpha^2+\beta^2)^{1/2}z]}{4(\alpha^2+\beta^2)^{3/2}(1-\sigma)} \\ \frac{\beta^2 z cosh[(\alpha^2+\beta^2)^{1/2}z]}{4(\alpha^2+\beta^2)(1-\sigma)} + \frac{[4(1-\sigma)(\alpha^2+\beta^2)-\beta^2]sinh[(\alpha^2+\beta^2)^{1/2}z]}{4(\alpha^2+\beta^2)^{3/2}(1-\sigma)} \\ \frac{-i\beta z sinh[(\alpha^2+\beta^2)^{1/2}z]}{4(\alpha^2+\beta^2)^{1/2}(1-\sigma)} \end{bmatrix} \tag{5.8}$$

$$\mathbf{W}_{\alpha\beta}(z) = \begin{bmatrix} \frac{-i\alpha z sinh[(\alpha^2+\beta^2)^{1/2}z]}{4(\alpha^2+\beta^2)^{1/2}(1-2\sigma)} \\ \frac{-i\beta z sinh[(\alpha^2+\beta^2)^{1/2}z]}{2(\alpha^2+\beta^2)^{1/2}(1-2\sigma)} \\ \frac{-z cosh[(\alpha^2+\beta^2)^{1/2}z]}{2(1-2\sigma)} + \frac{(3-4\sigma)sinh[(\alpha^2+\beta^2)^{1/2}z]}{2(1-2\sigma)} \end{bmatrix} \tag{5.9}$$

Eq. 5.6 provides the value of the displacement fields in the three directions generated at each plane of the substrate in the Fourier domain. By performing the inverse Fourier transform, we obtain the displacement fields in the three directions. They are calculated from the measured displacement fields in the surface of the gel and depend on the z-distance from the bottom of the gel and on the Poisson ratio's value. We measured the deformation fields in the three-dimensions on the surface of the gel, z=h, ($\mathbf{u_0}(x,y)$, $\mathbf{v_0}(x,y)$, $\mathbf{w_0}(x,y)$), and by solving eq. 5.6 we compute the displacement fields in all the substrate positions. We also measured the deformation fields in the three-dimensions at a certain distance from the surface, z=$h_1$, ($\mathbf{u_1}(x,y)$, $\mathbf{v_1}(x,y)$, $\mathbf{w_1}(x,y)$). Solving eq. 5.6 and performing the inverse Fourier transform, we calculate analytically the deformation fields at z=$h_1$, ($\mathbf{u_2}(x,y)$, $\mathbf{v_2}(x,y)$, $\mathbf{w_2}(x,y)$).

In order to calculate the Poisson ratio of the substrate, we solve a non-linear least squares problem using a Levenberg-Marquardt algorithm. We minimize the difference between the

displacement calculated analytically ($\mathbf{u_2}(x,y)$, $\mathbf{v_2}(x,y)$, $\mathbf{w_2}(x,y)$) and the measured ones at the same z-position ($\mathbf{u_1}(x,y)$, $\mathbf{v_1}(x,y)$, $\mathbf{w_1}(x,y)$). We perform an optimization method to minimize the value of a function that quantifies the difference between the displacement fields analitically calculated and the measured ones. We have used three different optimization functions to obtain the Poisson ratio's value:

$$\text{Function 1} = \left[(|\mathbf{u_2}|+|\mathbf{u_1}|)(\mathbf{u_2}-\mathbf{u_1}),(|\mathbf{v_2}|+|\mathbf{v_1}|)(\mathbf{v_2}-\mathbf{v_1}),(|\mathbf{w_2}|+|\mathbf{w_1}|)(\mathbf{w_2}-\mathbf{w_1})\right] \quad (5.10)$$

$$\text{Function 2} = \left[\int\int \left(|\mathbf{u_1}|^2(\mathbf{u_2}-\mathbf{u_1})^2+|\mathbf{v_1}|^2(\mathbf{v_2}-\mathbf{v_1})^2+|\mathbf{w_1}|^2(\mathbf{w_2}-\mathbf{w_1})^2\right)dx\,dy\right]^{1/2} \quad (5.11)$$

$$\text{Function 3} = \left[1-\text{corr coeff.}(\mathbf{u_2},\mathbf{u_1}),1-\text{corr coeff.}(\mathbf{v_2},\mathbf{v_1}),1-\text{corr coeff.}(\mathbf{w_2},\mathbf{w_1}))\right] \quad (5.12)$$

where corr coeff. signifies correlation coefficient between the displacement fields indicated.

Function 1 calculates the difference between the magnitudes of the displacements calculated analytically and the measured ones at z=$h_1$ at each point. Function 2 calculates the square root of the integral of the difference between the magnitudes of the square value of the displacements calculated analytically and the measured ones at z=$h_1$. Function 3 calculates the maximum correlation coefficient between the displacements calculated analytically and the measured ones at z=$h_1$. The solution of the displacement fields ($\mathbf{u_2}(x,y)$, $\mathbf{v_2}(x,y)$, $\mathbf{w_2}(x,y)$) calculated analytically depends on the Poisson ratio, $\sigma$, since the components of $U_{\alpha\beta}$ depends on $\sigma$ (eq. 5.7-5.9). Therefore, the parameter that varies in the optimization for the minimization of the difference between the displacements calculated analytically and the measured ones is the Poisson ratio, $\sigma$. The value of the Poisson ratio of the substrate is the value that minimizes the optimization function.

## 5.3 Results

### 5.3.1 Analysis of the effect of the Poison ratio's value in the displacement fields transmitted inside the substratum

The deformation exerted by a force applied on the surface of an elastic substratum propagates towards its interior. The propagation of this deformation towards the interior of the substratum is different depending of its Poisson ratio, as can be inferred from eq. 5.6 . To systematically study the change of the deformation fields in each z-position of the substratum depending on the Poisson ratio and to avoid errors due to difference in experimental noise, we use synthetic displacement fields in the three directions. We design gaussian synthetic deformation fields in the three-directions to simulate the deformation applied on the surface of the substratum by a cell:

$$u(x,y,z=h) = U_0 e^{\frac{(X-\Delta)^2}{\mu^2}-\frac{(Y)^2}{\mu^2}} - U_0 e^{\frac{(X+\Delta)^2}{\mu^2}-\frac{(Y)^2}{\mu^2}} \tag{5.13}$$

$$v(x,y,z=h) = V_0 e^{\frac{(X)^2}{\mu^2}-\frac{(Y-\Delta)^2}{\mu^2}} - V_0 e^{\frac{(X)^2}{\mu^2}-\frac{(Y+\Delta)^2}{\mu^2}} \tag{5.14}$$

$$w(x,y,z=h) = \frac{W_0}{2} e^{\frac{(X-\Delta)^2}{\mu^2}-\frac{(Y)^2}{\mu^2}} + \frac{W_0}{2} e^{\frac{(X+\Delta)^2}{\mu^2}-\frac{(Y)^2}{\mu^2}} - W_0 e^{\frac{(X)^2}{\mu^2}-\frac{(Y)^2}{\mu^2}} \tag{5.15}$$

We add a random noise with a determined standard deviation, to approximate these deformation fields to the experimental conditions, as shown in Figure 5.3A . These synthetic fields were chosen because they are are similar to the displacement fields exerted by *Physarum* cells in the surface of the substratum where they move.

The displacement fields applied on the surface are ($\mathbf{u_0}(x,y)$, $\mathbf{v_0}(x,y)$, $\mathbf{w_0}(x,y)$). The value of the displacement fields for each z-position depends on the value of the Poisson ratio of the substrate. Figure 5.3B-E shows the decay of the displacement fields with the z-position in two transversal sections located at the positions A and B indicated in Figure 5.3A for two different values of the Poisson ratio.

The synthetic displacement fields applied 5$\mu$m below the surface, ($\mathbf{u_1}(x,y)$, $\mathbf{v_1}(x,y)$, $\mathbf{w_1}(x,y)$), are created by the propagation of ($\mathbf{u_0}(x,y)$, $\mathbf{v_0}(x,y)$, $\mathbf{w_0}(x,y)$), for the specific Poisson

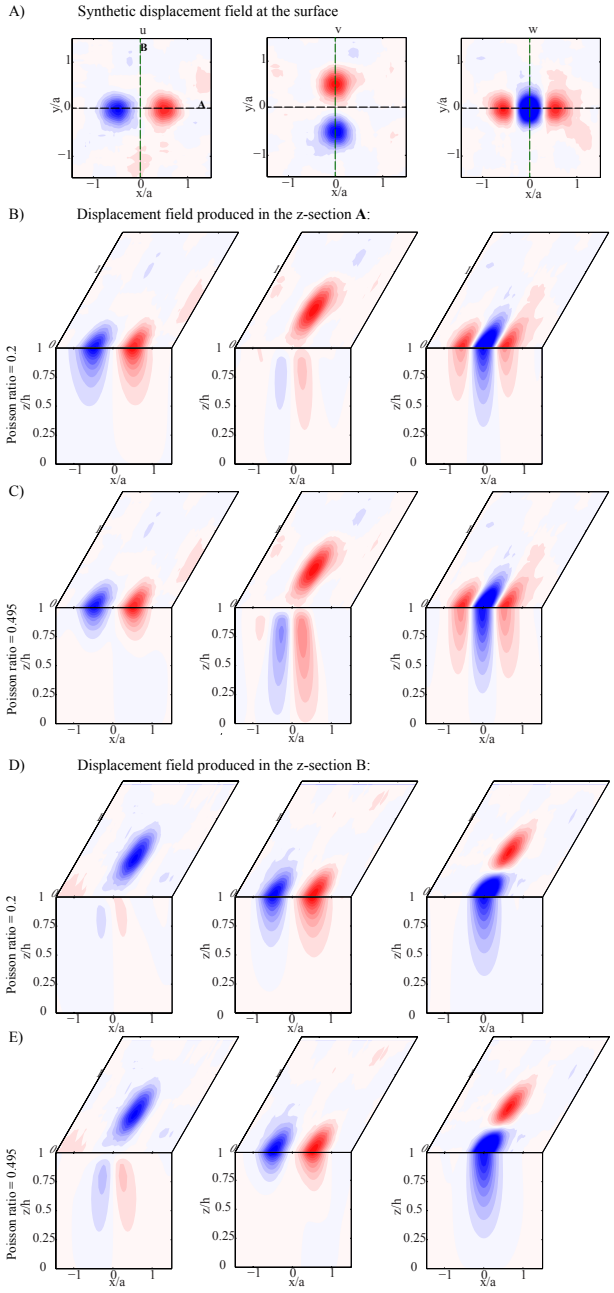


**Figure 5.3**: Simulated displacement field and decay within the z-direction of the substrate for different values of the Poisson ratio. A) Simulated displacement fields in the three dimensions applied in the surface of the substratum, given by eqs. 5.13-5.15. B) Decay of the displacement fields in section A when the Poisson ratio of the substratum is 0.2. C) Decay of the displacement fields in section A when the Poisson ratio of the substratum is 0.495. D) Decay of the displacement fields in section B when the Poisson ratio of the substratum is 0.2. E) Decay of the displacement fields in section B when the Poisson ratio of the substratum is 0.495.

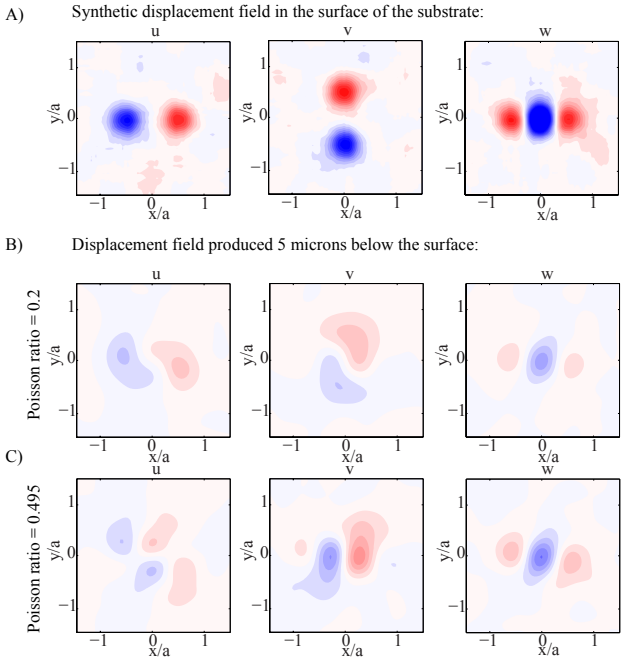


**Figure 5.4**: Displacement fields in a plane located 5$\mu$m below the surface for different values of the Poisson ratio for a gaussian displacement field. A) Simulated displacement fields in the three dimensions applied in the surface of the substratum, given by eqs. 5.13- 5.15. B) Displacement fields calculated in a plane located 5$\mu$m below the surface when the Poisson ratio of the substratum is 0.2. C) Displacement fields calculated in a plane located 5$\mu$m below the surface when the Poisson ratio of the substratum is 0.495.

ratio of the substrate using eq. 5.6 and adding a random noise with a determined standard deviation to approximate them to the experimental conditions. Figure 5.4A shows the simulated deformation fields assumed to be applied on the surface plane of a substratum and Figure 5.4B-C shows the deformation fields 5$\mu$m below the surface of this substratum for two different values of the Poisson ratio. It can be seen that the propagation of the deformation towards the interior of the substratum highly depends on the value of its Poisson ratio.

To characterize the influence of the Poisson ratio in the decay of the displacement field independently of the specific type of the synthetic displacement field, we have examined various simulated displacement fields. Figure 5.5 shows the influence of the Poisson ratio in the decay of

the displacement field given by:

$$u(x,y,z=h)=U_0(e^{\frac{(X-\Delta)^2}{\mu^2}-\frac{(Y)^2}{\mu^2}}+e^{\frac{(X-0.19\Delta)^2}{\mu^2}-\frac{(Y-0.12\Delta)^2}{\mu^2}})-U_0(e^{\frac{(X+0.14\Delta)^2}{\mu^2}-\frac{(Y+0.17\Delta)^2}{\mu^2}}-e^{\frac{(X+0.03\Delta)^2}{\mu^2}-\frac{(Y+0.05\Delta)^2}{\mu^2}}) \tag{5.16}$$

$$v(x,y,z=h)=V_0(e^{\frac{(X)^2}{\mu^2}-\frac{(Y-\Delta)^2}{\mu^2}}+e^{\frac{(X-0.12\Delta)^2}{\mu^2}-\frac{(Y-0.19\Delta)^2}{\mu^2}})-V_0(e^{\frac{(X+0.17\Delta)^2}{\mu^2}-\frac{(Y+0.14\Delta)^2}{\mu^2}}-e^{\frac{(X+0.05\Delta)^2}{\mu^2}-\frac{(Y+0.03\Delta)^2}{\mu^2}}) \tag{5.17}$$

$$\begin{aligned} w(x,y,z=h)=&\frac{W_0}{2}e^{\frac{(X-0.04\Delta)^2}{\mu^2}-\frac{(Y-0.5\Delta)^2}{\mu^2}}+\frac{W_0}{2}e^{\frac{(X-0.03\Delta)^2}{\mu^2}-\frac{(Y-0.03\Delta)^2}{\mu^2}}+\frac{W_0}{2}e^{\frac{(X+0.5\Delta)^2}{\mu^2}-\frac{(Y-0.08\Delta)^2}{\mu^2}}+\\ &+\frac{W_0}{2}e^{\frac{(X+0.1\Delta)^2}{\mu^2}-\frac{(Y+0.17\Delta)^2}{\mu^2}}-W_0e^{\frac{(X)^2}{\mu^2}-\frac{(Y)^2}{\mu^2}} \end{aligned} \tag{5.18}$$

A third type of displacement field that we simulated to characterize the performance of our method is shown in Figure 5.6. This displacement field decays faster than the previous ones, and is given by:

$$u(x,y,z=h)=\frac{U_0}{\sqrt{(x-\Delta)^2+y^2}}-\frac{U_0}{\sqrt{(x+\Delta)^2+y^2}} \tag{5.19}$$

$$v(x,y,z=h)=\frac{V_0}{\sqrt{x^2+(y-\Delta)^2}}-\frac{V_0}{\sqrt{x^2+(y+\Delta)^2}} \tag{5.20}$$

$$w(x,y,z=h)=\frac{W_0/2}{\sqrt{(x-\Delta)^2+y^2}}+\frac{W_0/2}{\sqrt{(x+\Delta)^2+y^2}}-\frac{W_0}{\sqrt{x^2+y^2}} \tag{5.21}$$

### 5.3.2 Analysis of the method's accuracy

We assumed that the displacement fields applied on the surface are the ones calculated in eqs. 5.13- 5.15, ($\mathbf{u_0}(x,y)$, $\mathbf{v_0}(x,y)$, $\mathbf{w_0}(x,y)$), with a random noise added as shown in Figure 5.4A. The displacement fields exerted in a plane 5$\mu$m below the surface, ($\mathbf{u_1}(x,y)$, $\mathbf{v_1}(x,y)$, $\mathbf{w_1}(x,y)$), are calculated form eq. 5.6 using a determined Poisson ratio and adding a random noise. Then we use our optimization algorithm, and the displacements fields, ($\mathbf{u_2}(x,y)$, $\mathbf{v_2}(x,y)$, $\mathbf{w_2}(x,y)$), that minimize the optimization function will be the ones that are calculated by using the actual Poisson ratio of the substratum.

We used in our simulations different values of the Poisson ratio and 15 different synthetic

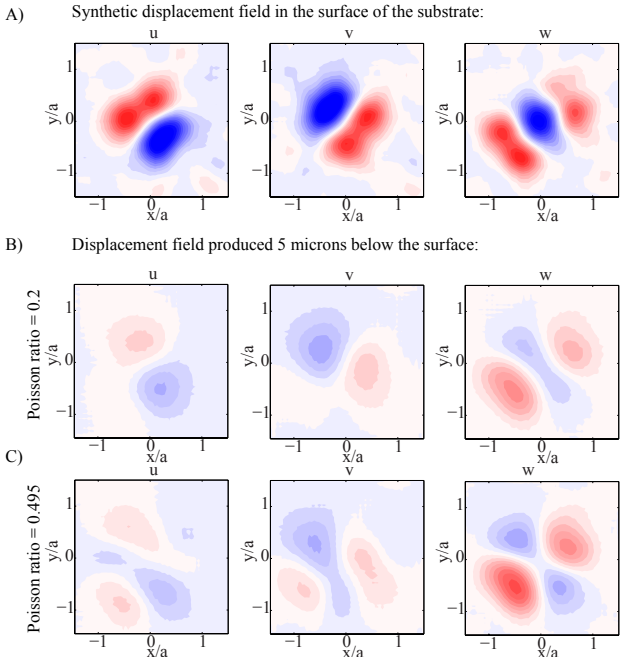


**Figure 5.5**: Displacement fields in a plane located 5$\mu$m below the surface of the substratum for different values of the Poisson ratio for the displacement field given by eqs. 5.16-5.18. A) Simulated displacement fields in the three dimensions applied in the surface of the substratum, given by eqs. 5.16-5.18. B) Predicted displacement fields in a plane located 5$\mu$m below the surface when the Poisson ratio of the substratum is 0.2. C) Predicted displacement fields in a plane located 5$\mu$m below the surface when the Poisson ratio of the substratum is 0.495.

displacements fields of each type, built as explained in section 5.3.1 for each value of the Poisson ratio. Figure 5.7A-C, shows the average value and standard mean error of the Poisson ratio calculated versus the exact one for the 15 simulated displacement fields for each value of the noise standard deviation, when using the three optimization functions indicated in section 5.2.5, given by eqs. 5.10- 5.12. We repeated the same analysis when using the displacement fields given by eqs. 5.16- 5.18. Figure 5.8 shows the he average value and standard mean error of the Poisson ratio calculated versus the exact one for the 15 simulated displacement fields with different random noise of a specific standard deviation added when using the three optimization functions. For these two types of displacement fields, the accuracy of the method decreases with the noise level of the simulated displacement fields, mainly when using the optimization functions 1 and 2 and when the value of the Poisson ratio is lower than 0.4. Figures 5.7C and 5.8C show

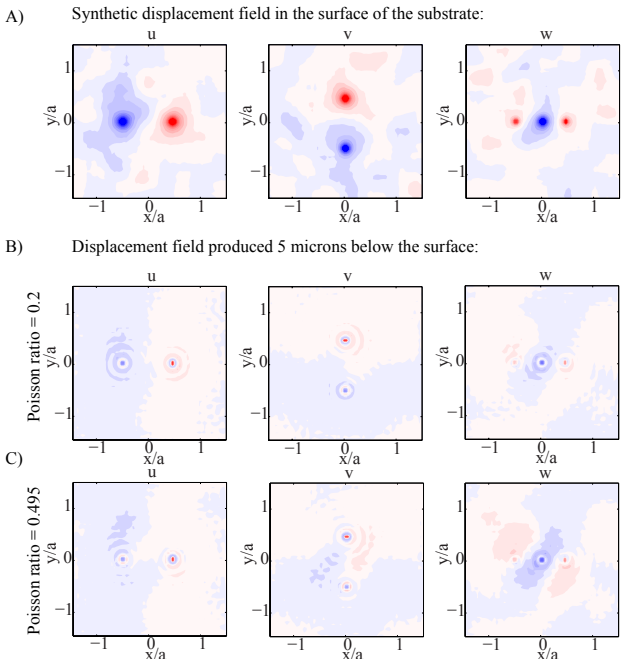


**Figure 5.6**: Displacement fields in a plane located 5$\mu$m below the surface of the substratum for different values of the Poisson ratio for a fast-decaying displacement field. A) Simulated fast-decaying displacement fields in the three dimensions applied in the surface of the substratum, given by eqs. 5.19- 5.21. B) Predicted displacement fields in a plane located 5$\mu$m below the surface when the Poisson ratio of the substratum is 0.2. C) Predicted displacement fields in a plane located 5$\mu$m below the surface when the Poisson ratio of the substratum is 0.495.

that the optimization function 3, which maximizes the value of the correlation coefficient between the displacement fields, is more robust than the other two optimization functions when the noise level increases. The standard mean error decreases when the value of the Poisson ratio increases for the three optimization functions. This method is very precise when the noise level is small and when the value of the Poisson ratio is bigger than 0.4 for any optimization function used.

We also performed this analysis when using the displacement fields shown in Figure 5.6, given by eqs. 5.19-5.21. This displacement field decays faster, and in this case the optimization functions given by eq. 5.10 and eq. 5.11 have a poorer performance as it is seen in Figure 5.9A-B. However, the results obtained with the optimization function based on the cross-correlation of the displacement fields, given by eq. 5.12 are very accurate even for high levels of noise. Therefore, we concluded that the optimization function based on the cross-correlation of the

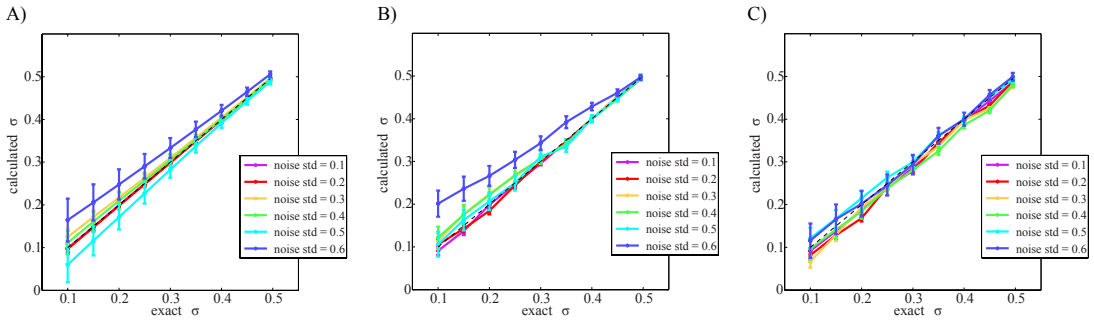


**Figure 5.7**: Comparison of the Poisson ratio calculated with our method and the exact one when using three different optimization functions. A) Comparison of the Poisson ratio calculated with our method and the exact one when using the function 1 (eq. 5.10) in the optimization algorithm for the displacement field shown in Figure 5.4. The mean value and standard mean error are shown for the Poisson ratio calculated when using 15 synthetic displacement fields based on eqs. 5.13- 5.15 for each different noise level. We examined six different noise levels depending on their standard deviation as indicated on the right. B) Same as in panel A when using the optimization function 2 (eq. 5.11). C) Same as in panel A when using the optimization function 3 (eq. 5.12).

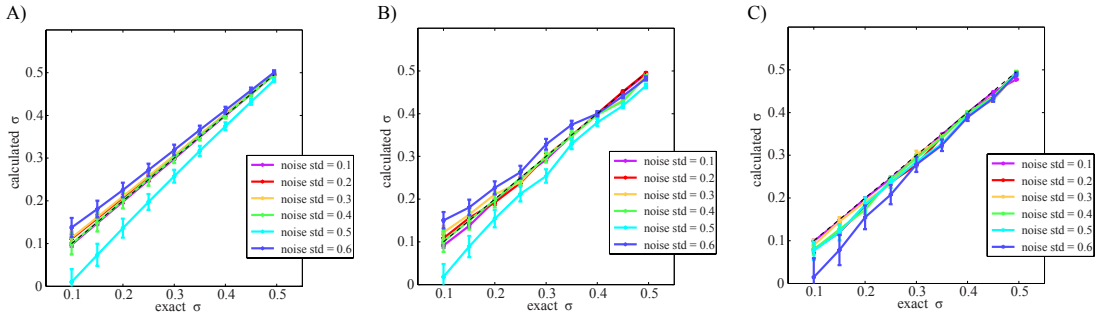


**Figure 5.8**: Comparison of the Poisson ratio calculated with our method and the exact one when using three different optimization functions for thehe displacement field shown in Figure 5.5. A) Comparison of the Poisson ratio calculated with our method and the exact one when using the function 1 (eq. 5.10) in the optimization algorithm for the displacement field shown in Figure 5.5. The mean value and standard mean error are shown for the Poisson ratio calculated when using 15 synthetic displacement fields based on eqs. 5.16- 5.18 for each different noise level. The noise level depends on the standard deviation as indicated on the right. B) Same as in panel A when using the optimization function 2 (eq. 5.11). C) Same as in panel A when using the optimization function 3 (eq. 5.12).

displacement field is the most robust one, and the results obtained through our algorithm using this optimization function are very accurate, specially if the value of the Poisson ratio is higher than 0.3 (Figures 5.7C, 5.8C and 5.9C).

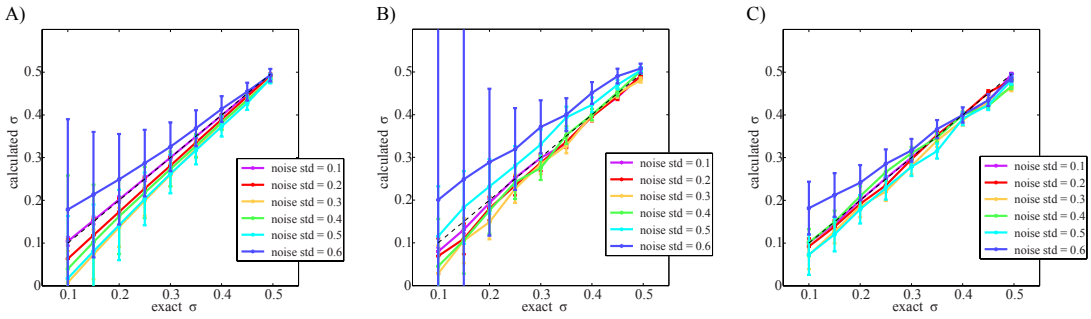


**Figure 5.9**: Comparison of the Poisson ratio calculated with our method and the exact one when using three different optimization functions for the displacement field shown in Figure 5.6. A) Comparison of the Poisson ratio calculated with our method and the exact one when using the function 1 (eq. 5.10) in the optimization algorithm for the displacement field shown in Figure 5.6. The mean value and standard mean error are shown for the Poisson ratio calculated when using 15 synthetic displacement fields based on eqs. 5.19- 5.21 for each different noise level. The noise level depends on the standard deviation as indicated on the right. B) Same as in panel A when using the optimization function 2 (eq. 5.11). C) Same as in panel A when using the optimization function 3 (eq. 5.12).

### 5.3.3 Experimental calculation of the Poison ratio for polyacrylamide gels

To characterize the Poisson ratio of polyacrylamide gels, we measured the displacement fields exerted in the three dimensions by a *Physarum* cell moving over a polyacrylamide gel. We measured the displacement fields exerted on the two layers of the polyacrylamide gel embedded with fluorescent markers beads, using correlation techniques as explained in section 5.2.4. Once we have measured the displacements fields in the surface of the gel, $(\mathbf{u_0}(x,y), \mathbf{v_0}(x,y), \mathbf{w_0}(x,y))$, we calculate the displacement fields which are the propagation of these fields at a plane below the surface, located at a distance equal to the one at which the second plane with beads is, using eq. 5.6, $(\mathbf{u_2}(x,y), \mathbf{v_2}(x,y), \mathbf{w_2}(x,y))$. We measured the displacement fields in the plane embedded with green fluorescent beads, $(\mathbf{u_1}(x,y), \mathbf{v_1}(x,y), \mathbf{w_1}(x,y))$, using the same correlation techniques. Figure 5.10C-F shows an example of the displacement fields exerted by a representative *Physarum* cell at the surface of the polyacrylamide gel, $(\mathbf{u_0}(x,y), \mathbf{v_0}(x,y))$, and 16$\mu$m below the surface of the gel, $(\mathbf{u_1}(x,y), \mathbf{v_1}(x,y))$. Figure 5.10G-H shows the displacement fields resulting from the propagation of the ones exerted in the surface when the Poisson ratio of the substratum is the one calculated by our method for the specific substrate ($\sigma = 0.45$), $(\mathbf{u_2}(x,y), \mathbf{v_2}(x,y))$. We can see that

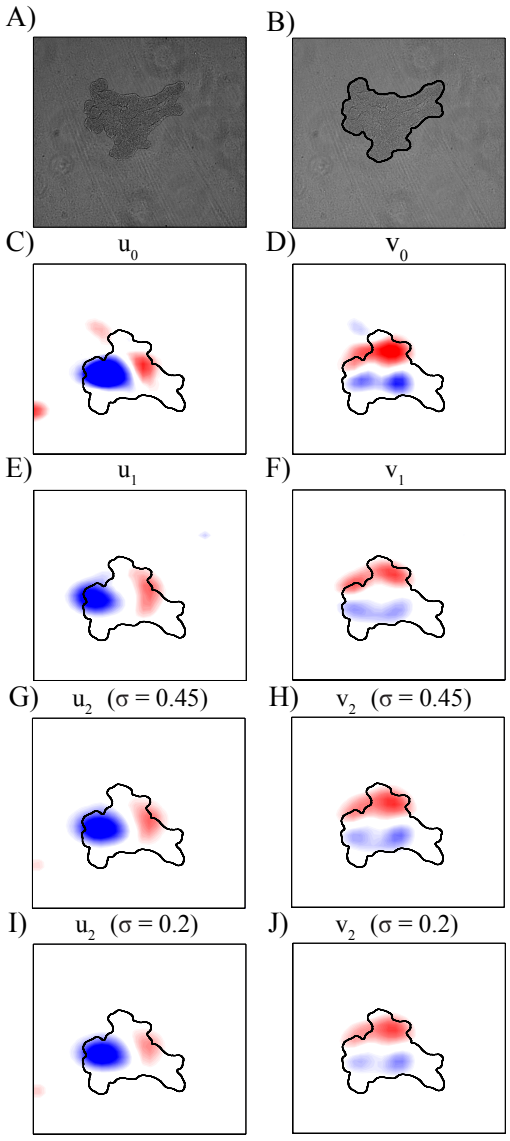


**Figure 5.10**: A) Bright field image of a representative *Phyrarum* cell at a specific instant of time. B) Bright field image and contour detection of this cell. C) Displacement field in the x-direction (direction of the cell major axis), $\mathbf{u_0}(x,y)$, exerted in the surface plane of the substratum measured by using our PIV method. D) Displacement field in the y-direction (perpendicular direction to the cell major axis), $\mathbf{v_0}(x,y)$, exerted in the surface plane of the substratum measured by using our PIV method. E) Displacement field in the x-direction exerted in a plane located 16$\mu$m below the surface of the substratum measured by using our PIV method, $\mathbf{u_1}(x,y)$. F) Same as in panel E for the displacement field in the y-direction, $\mathbf{v_1}(x,y)$. G) Displacement field in the x-direction calculated analytically in a plane located 16$\mu$m below the surface for the Poisson ratio measured for the specific substrate with our method ($\sigma = 0.45$), $\mathbf{u_2}(x,y)$. H) Same as in panel G for the displacement field in the y-direction, $\mathbf{v_2}(x,y)$. I) Same as in panel G for a Poisson ratio equal to 0.2. J) Same as in panel H for a Poisson ratio equal to 0.2.

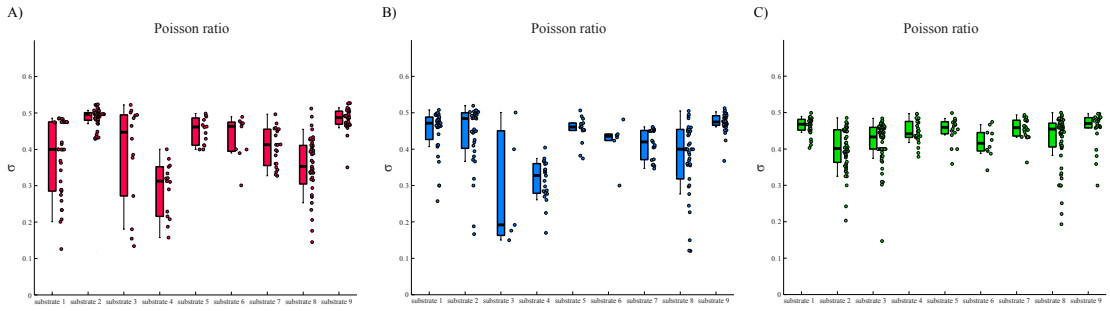


**Figure 5.11**: Poisson ratio determined for nine different experiments using polyacrylamide substrates. A) Poisson ratio determined for nine different polyacrylamide substrates, obtained by using function 1 (eq. 5.10) in the optimization algorithm. B) Poisson ratio determined for nine different polyacrylamide substrates, obtained by using function 2 (eq. 5.11) in the optimization algorithm. C) Poisson ratio determined for nine different polyacrylamide substrates, obtained by using function 3 (eq. 5.12) in the optimization algorithm.

the displacement fields shown in Figure 5.10G-H are more similar to the ones in Figure 5.10E-F than the displacement fields shown in Figure 5.10I-J, which are the displacement fields calculated from the propagation of the ones exerted in the surface for a Poisson ratio equal to 0.2.

The Poisson ratio of the substrate is calculated through an iterative process of optimization, consisting on minimizing the difference between the displacement fields calculated using eq. 5.6 and the measured ones in a plane at the same distance below the surface. Since the only unknown parameter in the function used for the optimization is the Poisson ratio, $\sigma$ (from eq. 5.6), this is the the parameter that varies in the iteration process. The value of the Poisson ratio that minimizes the optimization function is the value of the Poisson ratio of the substratum that we are using in the experiment.

Since we are doing time-lapse recordings, we calculate the displacement fields and perform the optimization process for each instant of time. Therefore, our method computes the Poisson ratio of the substrate at each location in which we acquire the z-stack of images. Figure 5.11 shows boxplots of the Poisson ratio calculated for nine different substrates using our new elastometry method, when using the three optimization functions in eqs. 5.10- 5.12. The variation between the values calculated for these substrates is small. Figure 5.12 shows a boxplot including all the time points in the nine substrates used for the calculation of the Poisson ratio

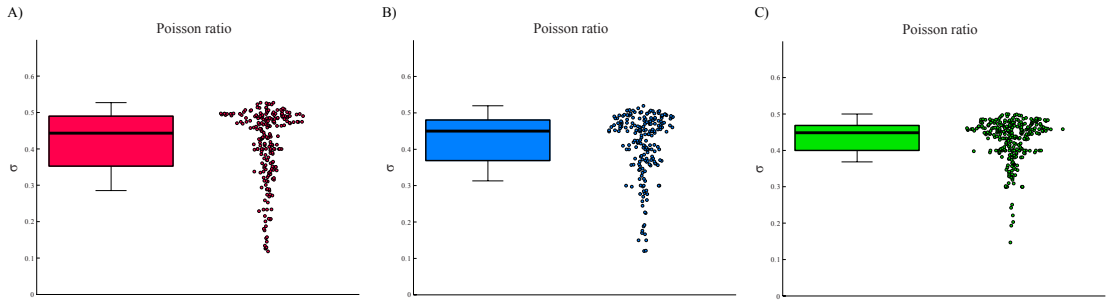


**Figure 5.12**: Boxplots showing the Poisson ratio of polyacrylamide substrates using three different optimization functions. A) Poisson ratio of polyacrylamide substrates using the measurements calculated for nine substrates, obtained through function 1 (eq. 5.10) in the optimization algorithm. B) Poisson ratio of polyacrylamide substrates using the measurements calculated for nine substrates, obtained through function 2 (eq. 5.11) in the optimization algorithm. C) Poisson ratio of polyacrylamide substrates using the measurements calculated for nine substrates, obtained through function 3 (eq. 5.12) in the optimization algorithm.

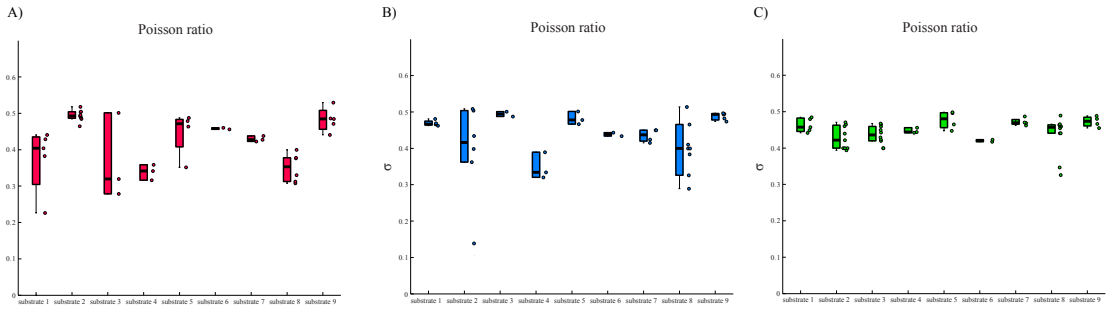


**Figure 5.13**: Poisson ratio determined for nine different experiments using polyacrylamide substrates through the combination of the displacement fields of six consecutive instants of time in the optimization problem. A) Poisson ratio determined for nine different substrates, obtained by using function 1 (eq. 5.10) in the optimization algorithm and through the combination of the displacement fields of six consecutive instants of time in the optimization problem. B) Poisson ratio determined for nine different substrates, obtained by the using function 2 (eq. 5.11) in the optimization algorithm and through the combination of the displacement fields of six consecutive instants of time in the optimization problem. C) Poisson ratio determined for nine different substrates, obtained by the using function 3 (eq. 5.12) in the optimization algorithm and through the combination of the displacement fields of six consecutive instants of time in the optimization problem.

when using the three optimization functions in eqs. 5.10- 5.12. The optimization function used doesn't influence the result obtained for the Poisson ratio. The mean value that we obtain for the Poisson ratio is 0.45, regardless of the optimization function used in our algorithm. This result

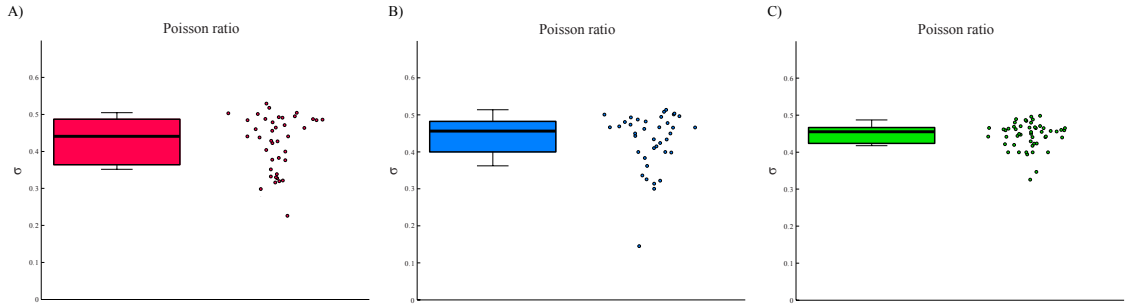


**Figure 5.14**: Boxplots showing the Poisson ratio of polyacrylamide substrates through the combination of the displacement fields of six consecutive instants of time in the optimization problem for three optimization functions. A) Poisson ratio of polyacrylamide substrates using the measurements obtained for nine substrates, using function 1 (eq. 5.10) for the optimization algorithm and through the combination of the displacement fields of six consecutive instants of time in the optimization problem. B) Poisson ratio of polyacrylamide substrates using the measurements obtained for nine substrates, using function 2 (eq. 5.11) for the optimization algorithm and through the combination of the displacement fields of six consecutive instants of time in the optimization problem. C) Poisson ratio of polyacrylamide substrates using the measurements obtained for nine substrates, using function 3 (eq. 5.12) for the optimization algorithm and through the combination of the displacement fields of six consecutive instants of time in the optimization problem.

is in good agreement with previous studies that used different methods for its characterization [94][169][178].

We have also performed the optimization method by taking the displacement fields obtained for six consecutive instants of time for each experiment and applying our algorithm in the same manner. Figure 5.13 shows the results for the Poisson ratio obtained for each of the same nine experiments when we perform the optimization using the displacement fields of six consecutive instants of time combined and Figure 5.14 shows the mean Poisson obtained for all the experiments. The optimization through the combination of the displacement fields measured for six consecutive instants of time in each experiment gives results that are less disperse, specially when using the optimization function 3, eq. 5.12 (Figure 5.14C). The mean value that we obtain for the Poisson ratio when the optimization is applied to six instants of time at the same step is 0.45 as well, regardless the optimization function used.

## 5.4 Discussion

This study presents a new elastometry method, which poses a novel procedure to characterize the Poisson ratio of flexible polymer-based elastic hydrogels commonly used as extracellular matrix in cell culture. There are few studies that characterize the value of the Poisson ratio in elastic hydrogels due to a general assumption that this parameter barely influences the traction stresses, but on the contrary this has been shown not to be the case [43]. This new method offers the possibility of calculating the Poisson ratio of elastic hydrogels in real time and the simultaneous measurement of the traction forces exerted by moving cells.

Elastic polymer-based hydrogels are broadly used for the calculation of the traction forces that cells apply when moving. The accurate characterization of their elastic properties is crucial for a precise calculation of these traction forces. When using TFM, the stresses are proportional to the Young's modulus of the substratum, and therefore significant efforts are generally devoted to characterize this parameter. Well established methods have been developed to accurately measure the Young's modulus such as indentation, atomic force microscopy and manipulation of spherical beads [179][180]. On the other hand, many studies assumed that the value of the forces exerted by the cells didn't depend much on the value of the Poisson ratio of the substratum over which they move, but it has been shown that they are highly dependent on this value [43]. The stresses exerted by cells in both the normal and tangential directions to the substratum are highly affected by the Poison ratio's value, specially for the nearly incompressible gels, with Poisson ratio's values close to 0.5, that are typically used in TFM measurements. The inaccuracy in the calculation of the traction stresses due to an error in the value of the Poisson ratio may be much higher than the inaccuracy due to the same percentage of error in the value of the Young's modulus [43].

We calculated the accuracy of our elastometry method by using simulated synthetic displacement fields in the three directions with noise levels of a determined standard deviation. We showed that the result of the Poisson ratio does not depend on the function used for the optimization in the algorithm by trying three different functions. Although the mean error in the calculation of the Poisson ratio increases with the level of noise of the displacements fields used

in the optimization, we showed that our method is very robust, and the noise in the displacement fields doesn't affect the results, specially if the function that is used for the optimization is based on the correlation coefficient of the two displacement fields. We showed through the simulated displacement fields that our method provides accurate results for the calculation of the Poisson ratio of elastic gels.

The experimental procedure shown here for the calculation of the Poisson ratio of polyacrylamide gels, based on the measurement of the deformation exerted by *Physarum* cells and the solution of the elasticity equation of equilibrium, results in an average value of 0.45. Chippada et al. using the measurement of the displacements of non-spherical magnetic inclusions moved by a magnetic manipulator obtained a value close to 0.5 for polyacrylamide gels of the same percentage of monomer [94]. Takigawa et al. measured a value of 0.46, by measuring the stretch ratio between the elongation of the gel in the directions perpendicular and parallel to the mechanically stretched one [169]. Bodou et al. measured a value of 0.49 by measuring the deformation exerted through micropipette aspiration experiments [178]. The average Poisson ratio that we calculated is the same regardless of the optimization function that we used in the algorithm.

When using previous methods, the same substratum that is used for the measurement of the Poisson ratio can not be used for the measurement of the traction forces. With other techniques, the substrates used for the measurement of the Poisson ratio had to be much thicker than the ones that can be used in TFM. The internal microstructure of the polyacrylamide gels is not perfectly uniform [170] [171]. The difference in the internal composition increases with the ratio of cross-linking to monomer [170] and this inhomogeneous gel microstructure has an effect on its mechanical properties. Our method allows us to do both measurements, the value of the Poisson ratio and the traction forces exerted by a cell, simultaneously. Additionally, it has been suggested that the percentage of acrylamide and bisacrylamide and the amount of ammonium per sulfate influence the value of the Poisson ratio [95] [94]. Our new method provides a tool for accurately compute this value for each substrate in real time, which poses an advantage with respect to other existent methods. We have shown that this optimization method is very accurate

and robust, when using the optimization function based on the correlation of the displacement field and for the value of the Poisson ratio of these substrates.

Constitutive equations are necessary for calculating the forces exerted by cells when moving. Our new method can be extended to calculate the constitutive equations for other materials that are not purely elastic and have more complex behaviors, but are very relevant as ECM for cell culture. More physiological environments than polymer hydrogels are fibre-reinforced materials such as collagen or fibrin [181]. The elastic properties of tissue are associated with the directions of the collagen fibers and their dispersion [182] [183]. In this case the elastic materials properties can be formulated in terms of five invariants related to the deformation gradient tensor [184] [185]. With a similar approach to the exposed here, the deformation gradient tensor that is produced when a cell is moving inside a collagen matrix can be calculated. Applying an optimization algorithm that uses these five invariants as the parameters of the optimization, the specific constitutive equations for the matrix in which the cell is moving could be calculated and therefore the forces that the cell exerts while moving in the specific substratum.

Another application of our new method could be the study of the interaction between tumorgenic cells and the ECM. Oncogenic processes commonly trigger the deregularization and disorganization of the ECM [186] [187]. Our method could be applied for the study of the changes in the ECM when cancer cells migrate within it. This new understanding could help to unravel the involvement of the ECM in tumor development [188] [189]. This approach may allow, as well, the comparison of the mechanical properties of the ECM when non-tumorgenic cells, such as neutrophils, not secreting metalloproteases move within it and, on the other hand, when tumorgenic cells are present. The characterization of the behavior of the ECM in real time and the computation of the changes occurring when metalloproteases are secreted by cells will clarify the relationship between these processes.

This new elastometry method opens a wide range of possibilities for the characterization of the mechanical properties and constitutive equations of the substrates at the same time that TFM methods can be applied for measuring the traction forces simultaneously. The measurement of the mechanical properties of the substratum in real time offers the advantage of connecting the

influence of these mechanical properties to the mechanistic behavior and dynamics of the cells moving in the specific substratum.

Chapter 5 is currently being prepared for publication, “Novel Elastometric Microscopy to Characterize the Extracellular Matrix Properties” by B. Álvarez-González, R. A. Firtel, J. C. Lasheras and J. C. del Álamo. The thesis author is the primary investigator in this publication.

# Chapter 6

# Concluding remarks

A brief summary of the main conclusions achieved in this dissertation is presented in this chapter, although a more detail discussion can be found at the end of each chapter.

The amoeboid type of cell migration requires that cells generate mechanical forces on their surrounding environment through adhesions that are remodeled in a fast manner [104][139]. The spatiotemporal coordination of the force-generation mechanisms allows cells to protrude the leading edge and retract the trailing edge with a well-defined frequency, and the speed of migration is proportional to this frequency [24].

However, the mechanics of amoeboid cell migration and particularly the role that the cell-generated forces play in this process are far from understood in contrast to the much better understood mechanism of the mesenchymal type of cell migration, in which the dependence between migration speed and the strength of cell-substrate forces has been characterized experimentally and explained by mathematical models [140][141]. Nevertheless, in the case of the amoeboid type of cell migration, previous studies reveal no correlation between the magnitude of the traction forces and the migration speed [40][90].

To investigate the role of cellular forces in establishing the speed of amoeboid cell migration, we measured the three-dimensional forces exerted by wild-type *Dictyostelium* cells,

as well as eight mutant strains with leading edge and posterior cross-linking defects, deficient cortical integrity and impaired linking between the membrane and the cortical and intracellular F-actin, chemotaxing on flat elastic substrates. We calculated these three-dimensional forces using the 3D Fourier Force Microscopy technique developed by del Álamo et al. [43]. Additionally, we analyzed the accuracy in the calculation of the deformation field exerted, which is essential to ensure that we used the optimal configuration for the acquisition of the images, that led to accurate measurements of the cell-substrate forces. We found that the tangential and normal components of these forces are comparable in magnitude [105][72],

Previous studies based on two-dimensional Traction Force Microscopy indicated that the forces generated by *Dictyostelium* wild-type cells on the substrate are typically concentrated in two or three well-defined areas at the front and the back of the cell [106], leading to a pattern of axial contraction directed toward the cell center. Existing measurements of the tangential forces in mutant strains lacking the proteins myosin II and filamin indicated that these mutant strains use lateral squeezing to propel the cytoplasmic material, and that the role of the F-actin polymerization at the front is reduced [30].

Interestingly, the physics of a system as simple as a sessile liquid drop may offer hints about how a crawling cell may exert normal forces. Liquid drops have been shown to exert normal forces when placed onto soft substrates, causing the substrate to deform in a similar manner than the observed for cells: upwards around the droplet edge and downwards under its center [114][190]. In the case of the drop, the physical reason for this force pattern is well understood, the surface tension at the interface between the substrate and the droplet is balanced by a pressure rise inside the drop. In a similar manner, the mechanical tension in the cell membrane and cortex, and the associated cytosolic pressure can generate both, the pulling and compressive normal forces exerted by migrating cells in the normal direction to the substrate's surface.

We corroborated that cortical tension is generating the perpendicular forces to the substrate by estimating the cortical tension of all the cell lines that we have examined. To do that, we used our measurements of the normal cell-substrate forces and a simple model assuming that the cortical tension is balanced by an increase in cytoplasmic pressure with respect to the extracellular

medium, based on the Young-Laplace's law. The cortical tensions estimated in this manner were found to be in good agreement with previously reported data measured by micropipette aspiration or cell poking for the cell lines considered in this study [126][124].

We showed that cells pull on their substrate adhesions using two distinct, yet interconnected mechanisms: axial acto-myosin contractility and cortical tension. The existence of these two mechanisms and the previously unreported transmission of cortical tension to the substrate explains the three-dimensional cell-substrate force patterns generated by cells lacking the leading edge and posterior cross-linking (*mhcA*$^-$ and *abp120*$^-$), cells with cross-linking defects in the cortical region (*ctxA*$^-$*/B*$^-$, *ctxA*$^-$, *ctxB*$^-$) and strains that are defective in linking the membrane and the cortical and intracellular F-actin (*myoA*$^-$*/B*$^-$ , *myoA*$^-$ , *myoB*$^-$).

The tension of the plasma membrane in *Dictyostelium* has been measured to be 1000 times smaller than the cortical tension [147], therefore it should make a minute contribution to the generation of three-dimensional cell-substrate forces.

Furthermore, the lack of correlation between cortical tension and axial contractility that we observed in the cell lines lacking myosin I in contrast to the high correlation shown in the rest of the cell lines, suggests that myosin I may be necessary for the proper communication of forces generated by the cortical and intracellular cytoskeletal networks. Our data is consistent with a model in which the two force-generating cellular domains are mechanically connected by myosin I cross-linking that enables the communication of forces between the domains.

The nature and molecular receptors controlling cell-substrate adhesion in *Dictyostelium* are not fully identified [31][113]. However, actin-rich structures often referred to as actin foci are localized in the adhesion regions of migrating *Dictyostelium* cells [46][100]. Our study revealed that the locations of the actin foci coincide with the locations where the cell is applying pulling forces on the substrate, both in the tangential and normal directions. This observation implies that pulling forces require firm adhesion to the substrate and are directly transmitted by the actin cytoskeleton. In contrast, we did not observe localization of actin foci in the regions where cells were generating compressive, normal forces on the substrate, which suggests that adhesions are not required by the cell to push down on the substrate, and that these compressive forces may be

transmitted directly by cytosolic pressure rather than by the cytoskeleton.

It was previously speculated that the cell's nucleus caused the generation of compressive forces [41][42][105], but we discarded this possibility for *Dictyostelium* cells due to the lack of co-localization between the position of the nucleus and the regions where the compressive forces in the direction perpendicular to the substrate were applied.

In addition, we found that cell migration speed depends on the relative magnitude of the tangential and normal forces, which reveals a novel role for three-dimensional cellular forces in establishing the efficiency of amoeboid cell movement. Our measurements uncovered a clear relationship between the cell speed and the ratio of the tangential to normal forces, suggesting that cells can modulate their shape and move faster if they are able to generate periodic axial contractions that balance the tension of their cortex. Thus, from a mechanical point of view, the normal cell-substrate forces that result from cortical tension could be viewed as an immobilization mechanism rather than a locomotion facilitator.

For a long time, it has been known that the tangential traction forces exerted by crawling cells are much larger than those needed to overcome the external resistance of the environment, but the reason why the cells exert these large forces was unknown. The migration speed increases when axial contractility overcomes cortical tension to produce the cell shape changes needed for locomotion, and therefore the cell needs to counterbalance the tension of its cortex through axial contractions. Consequently, the magnitude of the forces is established so as the cells are able to move and depends on the cells' cortical tension. Our findings suggest the first mechanistic explanation for the existence of such large traction forces.

We have also developed a method to calculate the three dimensional forces exerted by cells improved by Lagrange multipliers optimization. The results from this method are subject to two constraints: the forces must be in equilibrium and applied only in the region where the cell is located. The results obtained with this method are based on the optimization of the measurements of the correlation functions used for the calculation of the displacement filed. Besides taking into account the experimental measurements, this method provides results that are more consistent with the physics behind the problem.

Furthermore, we have designed a technique for the characterization of the properties of the extracellular matrix in real time, which allows for the simultaneous measurement of the forces exerted by cells, as well. This novel elastometry method is based on the exact solution of the elastic equation of equilibrium, the measurement of the deformation exerted by cells when moving over an elastic substrate and the application of an optimization algorithm for solving a non-linear least-squares problem. This method is an extension from Fourier Traction Force Microscopy, with a novel application as Elastometric Microscopy. Elastic polymer-based hydrogels are broadly used for the calculation of the traction forces that cells apply when moving. The value of the forces is very sensitive to the value of their Poisson ratio, especially for values close to 0.5, which is the case of polyacrylamide gels extensively used in Traction Force Microscopy. We present a novel method for characterizing the Poisson ratio of polymer-based substrates on real time. The value of the Poisson ratio that we obtained for the polyacrylamide gels used in our experiments is approximately 0.45.

We have previously shown that the distribution and dynamics of the tangential traction forces exerted by mammalian cells moving in a neutrophil-like manner are similar to the ones in *Dityostelium* [30]. A natural way to continue the work done in this dissertation would be to quantify the three dimensional forces generated by amoeboid migrating mammalian cells, such as neutrophils or some cancer cells, and their relationship with the efficiency of migration. Furthermore, other extension of this work should be to study the migration in the process of invasion across three-dimensional matrices and when cells are confined within three-dimensional environments.

The calculation of the forces applied by cells migrating across or inside three-dimensional matrices, poses the need of a mechanical characterization of the surrounding matrix that may not be linearly elastic and could be remodeled by the activity of metalloproteases segregated by some cells. Our Elastometric Microscopy method could be used to calculate the mechanical properties and constitutive equations for this type of extracellular environments, which are not perfectly elastic, since in the case of fibre-reinforced materials such as collagen or fibrin, the material properties can be formulated in terms of five invariants related to the deformation gradient tensor

[184][185]. With a similar approach to the exposed in this dissertation, the deformation gradient tensor that is produced when a cell is moving inside a fiber-reinforced surrounding matrix can be computed. The specific constitutive equations for the matrix in which the cell is moving could be determined, as well, applying an optimization algorithm that uses these five invariants as the parameters of the optimization, in a similar way to the explained in chapter 5.

In addition, we have shown that in the case of *Dictyostelium* cells, wild-type cells move slower than mutant strains with deficient cortical integrity or with impaired connection between the plasma membrane and the cortical and intracellular F-actin, due to the lower axial-contractility to cortical tension relative values. The relevance of the higher cortical tension values may reside in the movement of cells inside confined environments. When cells move inside a three-dimensional matrix, they could need the force generated through the cortical tension to squeeze inside it. A hypothesis may be that cells with cortical cross-linking defects are unable to move in confined environments. A fundamental continuation of this study would be to examine the importance of the cellular cortical tension in the movement inside the matrix. Amoeboid migrating cells, such as leukocytes squeeze through small gaps in the extracellular matrix and may use similar mechanisms to push off the surrounding obstacles [153]. Therefore, it is crucial to understand the mechanisms underlying amoeboid migration within fully confined matrices.

Our novel methodology for the characterization of the properties of the surrounding matrix has the potential to be used for the quantification of the interactions between different cells and the environment in which they move in real time. Our new elastometry method allows a wide range of possibilities for the characterization of the mechanical properties and constitutive equations of the substrates at the same time that Traction Force Microscopy methods can be applied for measuring the traction forces simultaneously in real time. The characterization of the behavior and change of the matrix when moving cells secret metalloproteases, would clarify the interaction between these cells and the surrounding matrix. This could be applied to understand the interplay between tumorgenic cells and their surrounding and how the characteristics of the environment influence the tumor development [189]. This approach may allow, as well, the comparison of the mechanical properties of the extracellular matrix when non-tumorgenic cells,

such as neutrophils, not secreting metalloproteases move within a matrix and, on the other hand, when tumorgenic cells are present.

Quantifying the interaction between the biochemistry and the mechanics underlying cell migration and its function in setting the speed and efficiency of the motion is fundamental to better control and predict cell migration. The new findings in this direction could guide the development of novel therapeutic approaches for efficient treatments of pathological diseases, such as cancer.

# Bibliography


[1] Lauffenburger, D. A., and A. F. Horwitz, 1996. Cell Migration: A Physically Integrated Molecular Process. *cell* 84:359–369.

[2] Wallingford, J. B., S. E. Fraser, and R. M. Harland, 2002. Convergent extension: the molecular control of polarized cell movement during embryonic development. *Dev. Cell* 2:695–706.

[3] Kumar, S., and V. M. Weaver, 2009. Mechanics, malignancy, and metastasis: the force journey of a tumor cell. *Cancer Metastasis Rev.* 28:113–127.

[4] Ross, R., 1995. Cell biology of atherosclerosis. *Annu. Rev. Physiol.* 57:791–804.

[5] Louis, S. F., and P. Zahradka, 2010. Vascular smooth muscle cell motility: From migration to invasion. *Exp Clin Cardiol* 15:75–85.

[6] Ingegnoli, F., M. Blades, A. Manzo, S. Wahid, M. Perretti, G. Panayi, and C. Pitzalis, 2002. [Role of cell migration in the pathogenesis of rheumatoid arthritis: in vivo studies in SCID mice transplanted with human synovial membrane]. *Reumatismo* 54:128–132.

[7] Zozulya, A. L., and H. Wiendl, 2008. The role of regulatory T cells in multiple sclerosis. *Nat Clin Pract Neurol* 4:384–398.

[8] Ananthakrishnan, R., and A. Ehrlicher, 2007. The Forces Behind Cell Movement. *International Journal of Biological Sciences* 3:303–317.

[9] Ciobanasu, C., B. Faivre, and C. Le Clainche, 2012. Actin dynamics associated with focal adhesions. *Int J Cell Biol* 2012:941292.

[10] Li, S., J. L. Guan, and S. Chien, 2005. Biochemistry and biomechanics of cell motility. *Annu Rev Biomed Eng* 7:105–150.

[11] Janmey, P. A., 1998. The cytoskeleton and cell signaling: component localization and mechanical coupling. *Physiol. Rev.* 78:763–781.

[12] Mitchison, T. J., and L. P. Cramer, 1996. Actin-based cell motility and cell locomotion. *Cell* 84:371–379.

[13] Ingber, D. E., 2002. Mechanical signaling and the cellular response to extracellular matrix in angiogenesis and cardiovascular physiology. *Circ. Res.* 91:877–887.

[14] Ingber, D. E., 2003. Tensegrity II. How structural networks influence cellular information processing networks. *J. Cell. Sci.* 116:1397–1408.

[15] Asthagiri, A. R., and D. A. Lauffenburger, 2000. Bioengineering models of cell signaling. *Annu Rev Biomed Eng* 2:31–53.

[16] Lammermann, T., and M. Six, 2009. Mechanical modes of 'amoeboid' cell migration. *Current opinion in Cell Biology* 21:636–644.

[17] Friedl, P., and K. Wolf, 2009. plasticity of cell migration: a multiscale tunning model. *Journal of Cell Biology* 188:11–19.

[18] Beningo, K. A., M. Dembo, I. Kaverina, J. V. Small, and Y.-L. Wang, 2001. Nascent focal adhesions are responsible for the generation of strong propulsive forces in migrating fibroblasts. *Journal of Cell Biology* 153:881–888.

[19] Huttenlocher, A., and A. R. Horwitz, 2011. Integrins in Cell Migration. *Cold Spring Harbor Perspectives in Biology* 3.

[20] Jannat, R. A., M. Dembo, and D. A. Hammer, 2011. Traction forces of neutrophils migrating on compliant substrates. *Biophys. J.* 101:575–584.

[21] Mannherz, H. G., M. Mach, D. Nowak, M. Malicka-Blaszkiewicz, and A. Mazur, 2007. Lamellipodial and amoeboid cell locomotion: The role of actin-cycling and bleb formation. *Biophysical Reviews and Letters* 2:5–22.

[22] Smith, L. A., H. Aranda-Espinoza, J. B. Haun, M. Dembo, and D. A. Hammer, 2007. Neutrophil Traction Stresses are Concentrated in the Uropod during Migration. *Biophysical Journal* 92:58–60.

[23] Shin, M. E., Y. He, D. Li, S. Na, F. Chowdhury, Y.-C. Poh, O. Collin, P. Su, P. de Lanerolle, M. A. Schwartz, N. Wang, and F. Wang, 2010. Spatiotemporal organization, regulSpatiotemporal organization, regulation, and functions of tractions during neutrophil chemotaxis. *Blood* 116:3297–3310.

[24] Meili, R., B. Alonso-Latorre, J. C. del Álamo, R. A. Firtel, and J. C. Lasheras, 2010. Myosin II is essential for the spatiotemporal organization of traction forces during cell motility. *Molecular Biology of the Cell* 21:405–417.

[25] Affolter, M., and C. J. Weijer, 2005. Signaling to cytoskeletal dynamics during chemotaxis. *Dev. Cell* 9:19–34.

[26] Wessels, D., H. Vawter-Hugart, J. Murray, and D. R. Soll, 1994. Three-Dimensional Dynamics of Pseudopod Formation and the Regulation of Turning During the Motility Cycle of Dictyostelium. *Cell Motility and the Cytoskeleton* 27:1–12.

[27] Ehrengruber, M. U., D. A. Deranleau, and T. D. Coates, 1996. Shape oscillations of human neutrophil leukocytes: characterization and relationship to cell motility. *The Journal of Experimental Biology* 199:741–747.

[28] Murray, J., H. Vawter-Hugart, E. Voss, and D. R. Soll, 1992. Three-Dimensional Motility Cycle in Leukocytes. *Cell Motility and the Cytoskeleton* 22:211–223.

[29] Charest, P. G., and R. A. Firtel, 2007. Big roles for small GTPases in the control of directed cell movement. *Biochemical Journal* 401:377–390.

[30] Bastounis, E., R. Meili, B. Alvarez-Gonzalez, J. Francois, J. C. del Alamo, R. A. Firtel, and J. C. Lasheras, 2014. Both contractile axial and lateral traction force dynamics drive amoeboid cell motility. *J. Cell Biol.* 204:1045–1061.

[31] Uchida, K., and S. Yumura, 2004. Dynamics of novel feet of Dictyostelium cells during migration. *Journal of Cell Science* 117:1443–1455.

[32] Cornillon, S., L. Gebbie, M. Benghezal, P. Nair, S. Keller, B. Wehrle-Haller, S. J. Charette, F. Bruckert, F. Letourneur, and P. Cosson, 2006. An adhesion molecule in free-living Dictyostelium amoebae with integrin beta features. *EMBO Rep.* 7:617–621.

[33] Butler, J. P., I. M. Tolić-Nørrelykke, B. Fabry, and J. J. Fredberg, 2002. Traction fields, moments, and strain energy that cells exert on their surroundings. *American Journal of Cell Physiology* 282:595–605.

[34] Dembo, M., T. Oliver, A. Ishihara, and K. Jacobson, 1996. Imaging the Traction Stresses Exerted by Locomoting Cells with theElastic Substratum Method. *Biophysical Journal* 70:2008–2022.

[35] Li, B., and J. H.-C. Wang, 2010. Application of Sensing Techniques to Cellular Force Measurement. *Sensors* 10:9948–9962.

[36] Sabass, B., M. L. Gardel, C. M. Waterman, and U. S. Schwarz, 2008. High resolution traction force microscopy based on experimental and computational advances. *Biophys. J.* 94:207–220.

[37] Maruthamuthu, V., B. Sabass, U. S. Schwarz, and M. L. Gardel, 2011. Cell-ECM traction force modulates endogenous tension at cell-cell contacts. *Proc. Natl. Acad. Sci. U.S.A.* 108:4708–4713.

[38] Peschetola, V., V. M. Laurent, A. Duperray, R. Michel, D. Ambrosi, L. Preziosi, and C. Verdier, 2013. Time-dependent traction force microscopy for cancer cells as a measure of invasiveness. *Cytoskeleton (Hoboken)* 70:201–214.

[39] Munevar, S., Y. Wang, and M. Dembo, 2001. Traction force microscopy of migrating normal and H-ras transformed 3T3 fibroblasts. *Biophys. J.* 80:1744–1757.

[40] Lombardi, M. L., D. A. Knecht, M. Dembo, and J. Lee, 2007. Traction force microscopy in Dictyostelium reveals distinct roles for myosin II motor and actin crosslinking activity in polarized cell movement. *Journal of Cell Science* 120:1624–1634.

[41] Hur, S. S., Y. Zhao, Y.-S. Li, E. Botvinick, and S. Chien, 2009. Live Cells Exert 3-Dimensional Traction Forces on Their Substrata. *Cellular and Molecular Bioengineering* 2:425–436.

[42] Maskarinec, S. A., C. Franck, D. A. Tirrell, and G. Ravichandran, 2009. Quantifying cellular traction forces in three dimensions. *Proc. Natl. Acad. Sci. U.S.A.* 106:22108–22113.

[43] del Álamo, J. C., R. Meili, B. Álvarez-González, B. Alonso-Latorre, E. Bastounis, R. Firtel, and J. C. Lasheras, 2013. Three-Dimensional Quantification of Cellular Traction Forces and Mechanosensing of Thin Substrata by Fourier Traction Force Microscopy. *PLOS ONE* 8:e69850.

[44] Chisholm, R. L., A. M. Rushforth, R. S. Pollenz, E. R. Kuczmarski, and S. R. Tafuri, 1988. Dictyostelium discoideum myosin: isolation and characterization of cDNAs encoding the essential light chain. *Mol. Cell. Biol.* 8:794–801.

[45] Bosgraaf, L., and P. J. van Haastert, 2006. The regulation of myosin II in Dictyostelium. *Eur. J. Cell Biol.* 85:969–979.

[46] Uchida, K. S., T. Kitanishi-Yumura, and S. Yumura, 2003. Myosin II contributes to the posterior contraction and the anterior extension during the retraction phase in migrating Dictyostelium cells. *J. Cell. Sci.* 116:51–60.

[47] Conrad, P. A., K. A. Giuliano, G. Fisher, K. Collins, P. T. Matsudaira, and D. L. Taylor, 1993. Relative distribution of actin, myosin I, and myosin II during the wound healing response of fibroblasts. *J. Cell Biol.* 120:1381–1391.

[48] Cox, D., J. A. Ridsdale, J. Condeelis, and J. Hartwig, 1995. Genetic deletion of ABP-120 alters the three-dimensional organization of actin filaments in Dictyostelium pseudopods. *J. Cell Biol.* 128:819–835.

[49] Kicka, S., Z. Shen, S. J. Annesley, P. R. Fisher, S. Lee, S. Briggs, and R. A. Firtel, 2011. The LRRK2-related Roco kinase Roco2 is regulated by Rab1A and controls the actin cytoskeleton. *Mol. Biol. Cell* 22:2198–2211.

[50] Gilden, J., and M. F. Krummel, 2010. Control of cortical rigidity by the cytoskeleton: emerging roles for septins. *Cytoskeleton (Hoboken)* 67:477–486.

[51] Robinson, D. N., S. S. Ocon, R. S. Rock, and J. A. Spudich, 2002. Dynacortin is a novel actin bundling protein that localizes to dynamic actin structures. *J. Biol. Chem.* 277:9088–9095.

[52] Surcel, A., Y. S. Kee, T. Luo, and D. N. Robinson, 2010. Cytokinesis through biochemical-mechanical feedback loops. *Semin. Cell Dev. Biol.* 21:866–873.

[53] Green, R. A., E. Paluch, and K. Oegema, 2012. Cytokinesis in animal cells. *Annu. Rev. Cell Dev. Biol.* 28:29–58.

[54] Keren, K., Z. Pincus, G. M. Allen, E. L. Barnhart, G. Marriott, A. Mogilner, and J. A. Theriot, 2008. Mechanism of shape determination in motile cells. *Nature* 453:475–480.

[55] Tinevez, J. Y., U. Schulze, G. Salbreux, J. Roensch, J. F. Joanny, and E. Paluch, 2009. Role of cortical tension in bleb growth. *Proc. Natl. Acad. Sci. U.S.A.* 106:18581–18586.

[56] Strychalski, W., and R. D. Guy, 2013. A computational model of bleb formation. *Math Med Biol* 30:115–130.

[57] Dai, J., and M. P. Sheetz, 1999. Membrane tether formation from blebbing cells. *Biophys. J.* 77:3363–3370.

[58] Paluch, E., J. van der Gucht, and C. Sykes, 2006. Cracking up: symmetry breaking in cellular systems. *J. Cell Biol.* 175:687–692.

[59] Carvalho, K., F. C. Tsai, F. C. Tsai, E. Lees, R. Voituriez, G. H. Koenderink, and C. Sykes, 2013. Cell-sized liposomes reveal how actomyosin cortical tension drives shape change. *Proc. Natl. Acad. Sci. U.S.A.* 110:16456–16461.

[60] Stamenovic, D., and D. E. Ingber, 2002. Models of cytoskeletal mechanics of adherent cells. *Biomech Model Mechanobiol* 1:95–108.

[61] Jean, R. P., C. S. Chen, and A. A. Spector, 2005. Finite-element analysis of the adhesion-cytoskeleton-nucleus mechanotransduction pathway during endothelial cell rounding: axisymmetric model. *J Biomech Eng* 127:594–600.

[62] Ingber, D. E., 2006. Cellular mechanotransduction: putting all the pieces together again. *FASEB J.* 20:811–827.

[63] Rape, A., W. H. Guo, and Y. L. Wang, 2011. Microtubule depolymerization induces traction force increase through two distinct pathways. *J. Cell. Sci.* 124:4233–4240.

[64] Dumbauld, D. W., T. T. Lee, A. Singh, J. Scrimgeour, C. A. Gersbach, E. A. Zamir, J. Fu, C. S. Chen, J. E. Curtis, S. W. Craig, and A. J. Garcia, 2013. How vinculin regulates force transmission. *Proc. Natl. Acad. Sci. U.S.A.* 110:9788–9793.

[65] Cha, I., and T. J. Jeon, 2011. Dynamic localization of the actin-bundling protein cortexillin I during cell migration. *Mol. Cells* 32:281–287.

[66] Ren, Y., J. C. Effler, M. Norstrom, T. Luo, R. A. Firtel, P. A. Iglesias, R. S. Rock, and D. N. Robinson, 2009. Mechanosensing through cooperative interactions between myosin II and the actin crosslinker cortexillin I. *Curr. Biol.* 19:1421–1428.

[67] Novak, K. D., M. D. Peterson, M. C. Reedy, and M. A. Titus, 1995. Dictyostelium myosin I double mutants exhibit conditional defects in pinocytosis. *J. Cell Biol.* 131:1205–1221.

[68] Mermall, V., P. L. Post, and M. S. Mooseker, 1998. Unconventional myosins in cell movement, membrane traffic, and signal transduction. *Science* 279:527–533.

[69] Khatau, S. B., R. J. Bloom, S. Bajpai, D. Razafsky, S. Zang, A. Giri, P. H. Wu, J. Marchand, A. Celedon, C. M. Hale, S. X. Sun, D. Hodzic, and D. Wirtz, 2012. The distinct roles of the nucleus and nucleus-cytoskeleton connections in three-dimensional cell migration. *Sci Rep* 2:488.

[70] Alam, S., D. B. Lovett, R. B. Dickinson, K. J. Roux, and T. P. Lele, 2014. Nuclear forces and cell mechanosensing. *Prog Mol Biol Transl Sci* 126:205–215.

[71] Hersen, P., and B. Ladoux, 2011. Biophysics: Push it, pull it. *Nature* 470:340–341.

[72] Franck, C., S. A. Maskarinec, D. A. Tirrell, and G. Ravichandran, 2011. Three-Dimensional Traction Force Microscopy: A New Tool for Quantifying Cell-Matrix Interactions. *PLOS ONE* 6:317833.

[73] Fu, J., Y. K. Wang, M. T. Yang, R. A. Desai, X. Yu, Z. Liu, and C. S. Chen, 2010. Mechanical regulation of cell function with geometrically modulated elastomeric substrates. *Nat. Methods* 7:733–736.

[74] Ye, G. J., Y. Aratyn-Schaus, A. P. Nesmith, F. S. Pasqualini, P. W. Alford, and K. K. Parker, 2014. The contractile strength of vascular smooth muscle myocytes is shape dependent. *Integr Biol (Camb)* 6:152–163.

[75] Lee, J., M. Leonard, T. Oliver, A. Ishihara, and K. Jacobson, 1994. Traction forces generated by locomoting keratocytes. *J. Cell Biol.* 127:1957–1964.

[76] Gallagher, R., S. Collins, J. Trujillo, K. McCredie, M. Ahearn, S. Tsai, R. Metzgar, G. Aulakh, R. Ting, F. Ruscetti, and R. Gallo, 1979. Characterization of the continuous, differentiating myeloid cell line (HL-60) from a patient with acute promyelocytic leukemia. *Blood* 54:713–733.

[77] Hauert, A. B., S. Martinelli, C. Marone, and V. Niggli, 2002. Differentiated HL-60 cells are a valid model system for the analysis of human neutrophil migration and chemotaxis. *Int. J. Biochem. Cell Biol.* 34:838–854.

[78] du Roure, O., A. Saez, A. Buguin, R. H. Austin, P. Chavrier, P. Silberzan, P. Siberzan, and B. Ladoux, 2005. Force mapping in epithelial cell migration. *Proc. Natl. Acad. Sci. U.S.A.* 102:2390–2395.

[79] Wang, J. H.-C., and J.-S. Lin, 2007. Cell traction force and measurement methods. *Biomechanics and Modeling in MechanoBiology* 6:361–371.

[80] Dembo, M., and Y.-L. Wang, 1999. Stresses at the Cell-to-Substrate Interface during Locomotion of Fibroblasts. *Biophysical Journal* 76:2307–2316.

[81] Yang, Z., J.-S. Lin, J. Chen, and J. H.-C. Wang, 2006. Determining substrate displacement and cell traction fields-a new approach. *Journal of Theoretical Biology* 242:607–616.

[82] Peterson, M. D., K. D. Novak, M. C. Reedy, J. I. Ruman, and M. A. Titus, 1995. Molecular genetic analysis of myoC, a Dictyostelium myosin I. *J. Cell. Sci.* 108 ( Pt 3):1093–1103.

[83] Fukui, Y., and S. Yumura, 1986. Actomyosin Dynamics in Chemotactic Amoeboid Movement of Dictyostelium. *Cell Motility and the Cytoskeleton* 6:662–673.

[84] Weber, I., G. Gerisch, C. Heizer, J. Murphy, K. Badelt, A. Stock, J. M. Schwartz, and J. Faix, 1999. Cytokinesis mediated through the recruitment of cortexillins into the cleavage furrow. *EMBO J.* 18:586–594.

[85] Sakamoto, T., J. Limouze, C. A. Combs, A. F. Straight, and J. R. Sellers, 2005. Blebbistatin, a myosin II inhibitor, is photoinactivated by blue light. *Biochemistry* 44:584–588.

[86] Kolega, J., 2004. Phototoxicity and photoinactivation of blebbistatin in UV and visible light. *Biochem. Biophys. Res. Commun.* 320:1020–1025.

[87] Wang, Y. L., and R. J. Jr.Pelham, 1998. Preparation of a Flexible, Porous Polyacrylamide Substrate for Mechanical Studies of Cultured Cells. *Methods in Enzymology* 298:489–496.

[88] Engler, A., L. Bacakova, C. Newman, A. Hategan, M. Griffin, and D. Discher, 2004. Substrate Compliance versus Ligand Density in Cell on Gel Responses. *Biophysical Journal* 86:617–628.

[89] Tse, J. R., and A. J. Engler, 2010. Preparation of hydrogel substrates with tunable mechanical properties. *Curr Protoc Cell Biol* Chapter 10:Unit 10.16.

[90] del Álamo, J. C., R. Meili, B. Alonso-Latorre, J. Rodriguez-Rodriguez, A. Aliseda, R. A. Firtel, and J. C. Lasheras, 2007. Spatiotemporal analysis of eukaryotic cell motility by improved force cytometry. *Proceedings of the National Academy of Sciences* 104:13343–13348.

[91] Keer, L. M., 1964. Stress distribution at the edge of an equilibrium crack. *Journal of the Mechanics and Physics of Solids* 12:149–163.

[92] Champagnat, F., A. Plyer, G. Le Besnerais, B. Leclaire, S. Davoust, and Y. Le Sant, 2011. Fast and accurate PIV computation using highly parallel iterative correlation maximization. *Experiments in Fluids* 50:1169–1182. http://dx.doi.org/10.1007/s00348-011-1054-x.

[93] Fore, L. B., 2010. Reduction of peak-locking errors produced by Gaussian sub-pixel interpolation in cross-correlation digital particle image velocimetry. *Measurement Science and Technology* 21:035402. http://stacks.iop.org/0957-0233/21/i=3/a=035402.

[94] Chippada, U., B. Yurke, and N. A. Langrana, 2011. Simultaneous determination of Young's modulus, shear modulus, and Poisson's ratio of soft hydrogels. *Journal of Materials Research* 25:545–555.

[95] Li, Y., Z. Hu, and C. Li, 1993. New Method for Measuring Poisson's Ratio in Polymer Gels. *Applied Polymer Science* 50:1107–1111.

[96] Erik Geissler, F. H., Anne-Marie Hecht, and M. Zrinyi, 1988. Compressional Modulus of Swollen Polyacrylamide Networks. *Macromolecules* 21:2594–2599.

[97] Toyjanova, J., E. Bar-Kochba, C. Lopez-Fagundo, J. Reichner, D. Hoffman-Kim, and C. Franck, 2014. High resolution, large deformation 3D traction force microscopy. *PLoS ONE* 9:e90976.

[98] Sen, S., A. J. Engler, and D. E. Discher, 2009. Matrix strains induced by cells: Computing how far cells can feel. *Cell Mol Bioeng* 2:39–48.

[99] Riedl, J., A. H. Crevenna, K. Kessenbrock, J. H. Yu, D. Neukirchen, M. Bista, F. Bradke, D. Jenne, T. A. Holak, Z. Werb, M. Sixt, and R. Wedlich-Soldner, 2008. Lifeact: a versatile marker to visualize F-actin. *Nat. Methods* 5:605–607.

[100] Yumura, S., and T. Kitanishi-Yumura, 1990. Fluorescence-mediated visualization of actin and myosin filaments in the contractile membrane-cytoskeleton complex of Dictyostelium discoideum. *Cell Struct. Funct.* 15:355–364.

[101] Stevense, M., J. R. Chubb, and T. Muramoto, 2011. Nuclear organization and transcriptional dynamics in Dictyostelium. *Dev. Growth Differ.* 53:576–586.

[102] Friedl, P., S. Borgmann, and E.-B. Brocker, 2001. Amoeboid leukocyte crawling through extracellular matrix: lessons from the Dictyostelium paradigm of cell movement. *Journal of Leukocyte Biology* 70:491–509.

[103] Bastounis, E., R. Meili, B. Alonso-Latorre, J. C. del Álamo, J. C. Lasheras, and R. A. Firtel, 2011. The SCAR/WAVE complex is necessary for proper regulation of traction stresses during amoeboid motility. *Molecular Biology of the Cell* 22:3995–4003.

[104] Jay, P. Y., P. A. Pham, S. A. Wong, and E. L. Elson, 1995. A mechanical function of myosin II in cell motility. *J. Cell. Sci.* 108 ( Pt 1):387–393.

[105] Delanoë-Ayari, H., and J. P. Rieu, 2010. 4D Traction Force Microscopy Reveals Asymmetric Cortical Forces in Migrating Dictyostelium Cells. *Physical Review Letters* 105:248103.

[106] Alvarez-Gonzalez, B., R. Meili, R. Firtel, E. Bastounis, J. C. Del Alamo, and J. C. Lasheras, 2014. Cytoskeletal Mechanics Regulating Amoeboid Cell Locomotion. *Appl Mech Rev* 66.

[107] Fukui, Y., and S. Inoue, 1997. Amoeboid movement anchored by eupodia, new actin-rich knobby feet in Dictyostelium. *Cell Motil. Cytoskeleton* 36:339–354.

[108] Burnette, D. T., L. Shao, C. Ott, A. M. Pasapera, R. S. Fischer, M. A. Baird, C. Der Loughian, H. Delanoe-Ayari, M. J. Paszek, M. W. Davidson, E. Betzig, and J. Lippincott-Schwartz, 2014. A contractile and counterbalancing adhesion system controls the 3D shape of crawling cells. *J. Cell Biol.* 205:83–96.

[109] Salbreux, G., G. Charras, and E. Paluch, 2012. Actin cortex mechanics and cellular morphogenesis. *Trends Cell Biol.* 22:536–545.

[110] Diz-Munoz, A., D. A. Fletcher, and O. D. Weiner, 2013. Use the force: membrane tension as an organizer of cell shape and motility. *Trends Cell Biol.* 23:47–53.

[111] Samstag, Y., S. M. Eibert, M. Klemke, and G. H. Wabnitz, 2003. Actin cytoskeletal dynamics in T lymphocyte activation and migration. *Journal of Leukocyte Biology* 30–48.

[112] Zimmermann, J., C. Brunner, M. Enculescu, M. Goegler, A. Ehrlicher, J. Kas, and M. Falcke, 2012. Actin filament elasticity and retrograde flow shape the force-velocity relation of motile cells. *Biophys. J.* 102:287–295.

[113] Fey, P., S. Stephens, M. A. Titus, and R. L. Chisholm, 2002. SadA, a novel adhesion receptor in Dictyostelium. *J. Cell Biol.* 159:1109–1119.

[114] Style, R. W., and E. R. Dufresne, 2012. Static wetting on deformable substrates, from liquids to soft solids. *Soft Matter* 8:7177–7184. http://dx.doi.org/10.1039/C2SM25540E.

[115] Weber, I., R. Neujahr, A. Du, J. Kohler, J. Faix, and G. Gerisch, 2000. Two-step positioning of a cleavage furrow by cortexillin and myosin II. *Curr. Biol.* 10:501–506.

[116] Faix, J., 2002. The actin-bundling protein cortexillin is the downstream target of a Rac1-signaling pathway required for cytokinesis. *J. Muscle Res. Cell. Motil.* 23:765–772.

[117] Faix, J., I. Weber, U. Mintert, J. Kohler, F. Lottspeich, and G. Marriott, 2001. Recruitment of cortexillin into the cleavage furrow is controlled by Rac1 and IQGAP-related proteins. *EMBO J.* 20:3705–3715.

[118] Faix, J., M. Steinmetz, H. Boves, R. A. Kammerer, F. Lottspeich, U. Mintert, J. Murphy, A. Stock, U. Aebi, and G. Gerisch, 1996. Cortexillins, major determinants of cell shape and size, are actin-bundling proteins with a parallel coiled-coil tail. *Cell* 86:631–642.

[119] Lee, S., Z. Shen, D. N. Robinson, S. Briggs, and R. A. Firtel, 2010. Involvement of the cytoskeleton in controlling leading-edge function during chemotaxis. *Mol. Biol. Cell* 21:1810–1824.

[120] Senda, S., S. F. Lee, G. P. Cote, and M. A. Titus, 2001. Recruitment of a specific amoeboid myosin I isoform to the plasma membrane in chemotactic Dictyostelium cells. *J. Biol. Chem.* 276:2898–2904.

[121] Legant, W. R., C. K. Choi, J. S. Miller, L. Shao, L. Gao, E. Betzig, and C. S. Chen, 2013. Multidimensional traction force microscopy reveals out-of-plane rotational moments about focal adhesions. *Proc. Natl. Acad. Sci. U.S.A.* 110:881–886.

[122] Khatau, S. B., C. M. Hale, P. J. Stewart-Hutchinson, M. S. Patel, C. L. Stewart, P. C. Searson, D. Hodzic, and D. Wirtz, 2009. A perinuclear actin cap regulates nuclear shape. *Proc. Natl. Acad. Sci. U.S.A.* 106:19017–19022.

[123] Chambliss, A. B., S. B. Khatau, N. Erdenberger, D. K. Robinson, D. Hodzic, G. D. Longmore, and D. Wirtz, 2013. The LINC-anchored actin cap connects the extracellular milieu to the nucleus for ultrafast mechanotransduction. *Sci Rep* 3:1087.

[124] Dai, J., H. P. Ting-Beall, R. M. Hochmuth, M. P. Sheetz, and M. A. Titus, 1999. Myosin I contributes to the generation of resting cortical tension. *Biophys. J.* 77:1168–1176.

[125] Gerald, N., J. Dai, H. P. Ting-Beall, and A. De Lozanne, 1998. A role for Dictyostelium racE in cortical tension and cleavage furrow progression. *J. Cell Biol.* 141:483–492.

[126] Reichl, E. M., Y. Ren, M. K. Morphew, M. Delannoy, J. C. Effler, K. D. Girard, S. Divi, P. A. Iglesias, S. C. Kuo, and D. N. Robinson, 2008. Interactions between myosin and actin crosslinkers control cytokinesis contractility dynamics and mechanics. *Curr. Biol.* 18:471–480.

[127] Luo, T., K. Mohan, P. A. Iglesias, and D. N. Robinson, 2013. Molecular mechanisms of cellular mechanosensing. *Nat Mater* 12:1064–1071.

[128] Pasternak, C., J. A. Spudich, and E. L. Elson, 1989. Capping of surface receptors and concomitant cortical tension are generated by conventional myosin. *Nature* 341:549–551.

[129] Titus, M. A., 2000. The role of unconventional myosins in Dictyostelium endocytosis. *J. Eukaryot. Microbiol.* 47:191–196.

[130] Kee, Y. S., Y. Ren, D. Dorfman, M. Iijima, R. Firtel, P. A. Iglesias, and D. N. Robinson, 2012. A mechanosensory system governs myosin II accumulation in dividing cells. *Mol. Biol. Cell* 23:1510–1523.

[131] Zischka, H., F. Oehme, T. Pintsch, A. Ott, H. Keller, J. Kellermann, and S. C. Schuster, 1999. Rearrangement of cortex proteins constitutes an osmoprotective mechanism in Dictyostelium. *EMBO J.* 18:4241–4249.

[132] Pintsch, T., M. Satre, G. Klein, J. B. Martin, and S. C. Schuster, 2001. Cytosolic acidification as a signal mediating hyperosmotic stress responses in Dictyostelium discoideum. *BMC Cell Biol.* 2:9.

[133] Gamper, M., E. Kim, P. K. Howard, H. Ma, T. Hunter, and R. A. Firtel, 1999. Regulation of Dictyostelium protein-tyrosine phosphatase-3 (PTP3) through osmotic shock and stress stimulation and identification of pp130 as a PTP3 substrate. *J. Biol. Chem.* 274:12129–12138.

[134] Pintsch, T., H. Zischka, and S. C. Schuster, 2002. Hisactophilin is involved in osmoprotection in Dictyostelium. *BMC Biochem.* 3:10.

[135] Na, J., B. Tunggal, and L. Eichinger, 2007. STATc is a key regulator of the transcriptional response to hyperosmotic shock. *BMC Genomics* 8:123.

[136] Kovacs, M., J. Toth, C. Hetenyi, A. Malnasi-Csizmadia, and J. R. Sellers, 2004. Mechanism of blebbistatin inhibition of myosin II. *J. Biol. Chem.* 279:35557–35563.

[137] Shu, S., X. Liu, and E. D. Korn, 2005. Blebbistatin and blebbistatin-inactivated myosin II inhibit myosin II-independent processes in Dictyostelium. *Proc. Natl. Acad. Sci. U.S.A.* 102:1472–1477.

[138] Limouze, J., A. F. Straight, T. Mitchison, and J. R. Sellers, 2004. Specificity of blebbistatin, an inhibitor of myosin II. *J. Muscle Res. Cell. Motil.* 25:337–341.

[139] Iwadate, Y., and S. Yumura, 2008. Actin-based propulsive forces and myosin-II-based contractile forces in migrating Dictyostelium cells. *J. Cell. Sci.* 121:1314–1324.

[140] Palecek, S. P., J. C. Loftus, M. H. Ginsberg, D. A. Lauffenburger, and A. F. Horwitz, 1997. Integrin-ligand binding properties govern cell migration speed through cell-substratum adhesiveness. *Nature* 385:537–540.

[141] Chan, C. E., and D. J. Odde, 2008. Traction dynamics of filopodia on compliant substrates. *Science* 322:1687–1691.

[142] Soll, D. R., D. Wessels, S. Kuhl, and D. F. Lusche, 2009. How a cell crawls and the role of cortical myosin II. *Eukaryotic Cell* 8:1381–1396.

[143] Murrell, M. P., R. Voituriez, J. Joanny, P. Nassoy, C. Sykes, and M. L. Gardel, 2014. Liposome adhesion generates traction stress. *Nature Physics* 10:163–169.

[144] Bischofs, I. B., S. S. Schmidt, and U. S. Schwarz, 2009. Effect of adhesion geometry and rigidity on cellular force distributions. *Phys. Rev. Lett.* 103:048101.

[145] Deshpande, V. S., R. M. McMeeking, and A. G. Evans, 2006. A bio-chemo-mechanical model for cell contractility. *Proc. Natl. Acad. Sci. U.S.A.* 103:14015–14020.

[146] Oakes, P. W., S. Banerjee, M. C. Marchetti, and M. L. Gardel, 2014. Geometry regulates traction stresses in adherent cells. *Biophys. J.* 107:825–833.

[147] Simson, R., E. Wallraff, J. Faix, J. Niewohner, G. Gerisch, and E. Sackmann, 1998. Membrane bending modulus and adhesion energy of wild-type and mutant cells of Dictyostelium lacking talin or cortexillins. *Biophys. J.* 74:514–522.

[148] Wessels, D., D. R. Soll, D. Knecht, W. F. Loomis, A. De Lozanne, and J. Spudich, 1988. Cell motility and chemotaxis in Dictyostelium amebae lacking myosin heavy chain. *Dev. Biol.* 128:164–177.

[149] Houk, A. R., A. Jilkine, C. O. Mejean, R. Boltyanskiy, E. R. Dufresne, S. B. Angenent, S. J. Altschuler, L. F. Wu, and O. D. Weiner, 2012. Membrane tension maintains cell polarity by confining signals to the leading edge during neutrophil migration. *Cell* 148:175–188.

[150] Raucher, D., and M. P. Sheetz, 2000. Cell spreading and lamellipodial extension rate is regulated by membrane tension. *J. Cell Biol.* 148:127–136.

[151] Yanai, M., C. M. Kenyon, J. P. Butler, P. T. Macklem, and S. M. Kelly, 1996. Intracellular pressure is a motive force for cell motion in Amoeba proteus. *Cell Motil. Cytoskeleton* 33:22–29.

[152] Langridge, P. D., and R. R. Kay, 2006. Blebbing of Dictyostelium cells in response to chemoattractant. *Exp. Cell Res.* 312:2009–2017.

[153] Lammermann, T., B. L. Bader, S. J. Monkley, T. Worbs, R. Wedlich-Soldner, K. Hirsch, M. Keller, R. Forster, D. R. Critchley, R. Fassler, and M. Six, 2008. Rapid leukocyte migration by integrin-independent flowing and squeezing. *Nature* 453:51–55.

[154] Aung, A., Y. N. Seo, S. Lu, Y. Wang, C. Jamora, J. C. del Alamo, and S. Varghese, 2014. 3D traction stresses activate protease-dependent invasion of cancer cells. *Biophys. J.* 107:2528–2537.

[155] Renkawitz, J., and M. Sixt, 2010. Mechanisms of force generation and force transmission during interstitial leukocyte migration. *EMBO Rep.* 11:744–750.

[156] Beningo, K. A., Y. L. Wang, and Y. L. Wang, 2002. Flexible substrata for the detection of cellular traction forces. *Trends Cell Biol.* 12:79–84.

[157] Gui, L., and S. T. Wereley, 2002. A correlation-based continuous window-shift technique to reduce the peak-locking effect in digital PIV image evaluation. *Experiments in Fluids* 32:506–517.

[158] Willert, C. E., and M. Gharib, 1991. Digital particle image velocimetry. *Experiments in Fluids* 10:181–193.

[159] Ng, S. S., C. Li, and V. Chan, 2011. Experimental and numerical determination of cellular traction force on polymeric hydrogels. *Interface Focus* 1:777–791.

[160] Pelham, R. J., and Y. l. Wang, 1997. Cell locomotion and focal adhesions are regulated by substrate flexibility. *Proc. Natl. Acad. Sci. U.S.A.* 94:13661–13665.

[161] Chowdhury, F., S. Na, D. Li, Y. C. Poh, T. S. Tanaka, F. Wang, and N. Wang, 2010. Material properties of the cell dictate stress-induced spreading and differentiation in embryonic stem cells. *Nat Mater* 9:82–88.

[162] Ulrich, T. A., E. M. de Juan Pardo, and S. Kumar, 2009. The mechanical rigidity of the extracellular matrix regulates the structure, motility, and proliferation of glioma cells. *Cancer Res.* 69:4167–4174.

[163] Vogel, V., and M. Sheetz, 2006. Local force and geometry sensing regulate cell functions. *Nat. Rev. Mol. Cell Biol.* 7:265–275.

[164] Li, B., C. Moshfegh, Z. Lin, J. Albuschies, and V. Vogel, 2013. Mesenchymal stem cells exploit extracellular matrix as mechanotransducer. *Sci Rep* 3:2425.

[165] Holle, A. W., and A. J. Engler, 2011. More than a feeling: discovering, understanding, and influencing mechanosensing pathways. *Curr. Opin. Biotechnol.* 22:648–654.

[166] Levental, I., K. R. Levental, E. A. Klein, R. Assoian, R. T. Miller, R. G. Wells, and P. A. Janmey, 2010. A simple indentation device for measuring micrometer-scale tissue stiffness. *J Phys Condens Matter* 22:194120.

[167] Frey, M. T., A. Engler, D. E. Discher, J. Lee, and Y. L. Wang, 2007. Microscopic methods for measuring the elasticity of gel substrates for cell culture: microspheres, microindenters, and atomic force microscopy. *Methods Cell Biol.* 83:47–65.

[168] D., L. L., and L. E. M., 1986. Theory of Elasticity, volume 7. Elsevier Ltd.

[169] Takigawa, T., Y. Morino, K. Urayama, and T. Masudab, 1996. Poisson's Ratio of Polyacrylamide (PAAm) Gels. *Polymer Gels and Networks* 4:1–5.

[170] Y. Cohen, I. J. K., O. Ramon, and S. Mizrahi, 1992. Characterization of inhomogeneous polyacrylamide hydrogels. *Journal of Polymer Science Part B: Polymer Physics* 30:1055–1067.

[171] J. Baselga, I. F. P. M. A. L., I. Hernandez-Fuentes, 1987. Elastic properties of highly crosslinked polyacrylamide gels. *Macromolecules* 20:3060–3065.

[172] Daniel, J. W., and H. P. Rusch, 1961. The pure culture of Physarum polycephalum on a partially defined soluble medium. *J. Gen. Microbiol.* 25:47–59.

[173] Wohlfarth-Bottermann, K. E., 1974. Plasmalemma Invaginations as Characteristic Constituents of Plasmodia of Physarum Polycephalum. *Journal of Cell Science* 16:23–37.

[174] Ueda, M., and S. Ogihara, 1994. Microtubules are required in amoeba chemotaxis for preferential stabilization of appropriate pseudopods. *J. Cell. Sci.* 107 ( Pt 8):2071–2079.

[175] http://www.micro-manager.org/, http://www.micro-manager.org/.

[176] Stuurman, N., N. Amdodaj, and R. Vale, 2007. Manager: Open Source Software for Light Microscope Imaging. *Microscopy Today* 15:42–43.

[177] Edelstein, A., N. Amodaj, K. Hoover, R. Vale, and N. Stuurman, 2010. Computer Control of Microscopes Using Manager. *Current Protocols in Molecular Biology* 14.20.1–14.20.17.

[178] Boudou, T., J. Ohayon, Y. Arntz, G. Finet, C. Picart, and P. Tracqui, 2006. An extended modeling of the micropipette aspiration experiment for the characterization of the Young's modulus and Poisson's ratio of adherent thin biological samples: numerical and experimental studies. *J Biomech* 39:1677–1685.

[179] Dimitriadis, E. K., F. Horkay, J. Maresca, B. Kachar, and R. S. Chadwick, 2002. Determination of elastic moduli of thin layers of soft material using the atomic force microscope. *Biophys. J.* 82:2798–2810.

[180] Long, R., M. S. Hall, M. Wu, and C. Y. Hui, 2011. Effects of gel thickness on microscopic indentation measurements of gel modulus. *Biophys. J.* 101:643–650.

[181] Lai, V. K., C. R. Frey, A. M. Kerandi, S. P. Lake, R. T. Tranquillo, and V. H. Barocas, 2012. Microstructural and mechanical differences between digested collagen-fibrin co-gels and pure collagen and fibrin gels. *Acta Biomater* 8:4031–4042.

[182] Holzapfel, G. A., and R. W. Ogden, 2010. Constitutive modelling of arteries. *Proceedings of the Royal Society A* 466:1551–1597.

[183] Xu, B., M. J. Chow, and Y. Zhang, 2011. Experimental and modeling study of collagen scaffolds with the effects of crosslinking and fiber alignment. *Int J Biomater* 2011:172389.

[184] Limbert, G., 2011. A mesostructurally-based anisotropic continuum model for biological soft tissues–decoupled invariant formulation. *J Mech Behav Biomed Mater* 4:1637–1657.

[185] Lu, J., and L. Zhang, 2005. Physically motivated invariant formulation for transversely isotropic hyperelasticity. *International Journal of Solids and Structures* 42:6015 – 6031. http://www.sciencedirect.com/science/article/pii/S0020768305002295.

[186] Jinka, R., R. Kapoor, P. G. Sistla, T. A. Raj, and G. Pande, 2012. Alterations in Cell-Extracellular Matrix Interactions during Progression of Cancers. *Int J Cell Biol* 2012:219196.

[187] Lu, P., V. M. Weaver, and Z. Werb, 2012. The extracellular matrix: a dynamic niche in cancer progression. *J. Cell Biol.* 196:395–406.

[188] Lochter, A., and M. J. Bissell, 1995. Involvement of extracellular matrix constituents in breast cancer. *Semin. Cancer Biol.* 6:165–173.

[189] Gilkes, D. M., G. L. Semenza, and D. Wirtz, 2014. Hypoxia and the extracellular matrix: drivers of tumour metastasis. *Nat. Rev. Cancer* 14:430–439.

[190] Style, R. W., Y. Che, S. J. Park, B. M. Weon, J. H. Je, C. Hyland, G. K. German, M. P. Power, L. A. Wilen, J. S. Wettlaufer, and E. R. Dufresne, 2013. Patterning droplets with durotaxis. *Proc. Natl. Acad. Sci. U.S.A.* 110:12541–12544.